Fall 1-31-2014

Nanocarbons as charge carriers in organic solar cells

Xinbo C. Lau
New Jersey Institute of Technology

ABSTRACT

NANOCARBONS AS CHARGE CARRIERS IN ORGANIC SOLAR CELLS

by
Xinbo C Lau

Organic photovoltaics (OPV) are an alternate to conventional silicon and thin film solar cells. They have several advantages such as simple fabrication, low material cost, light weight, and the ability to cover large areas. Typical OPV are based on bulk heterojunction structure consisting of a blend of an electron-donating semiconductor polymer and an electron-accepting molecule. Various approaches have been pursued to improve the performance of OPV: low bandgap polymers, new electron acceptors, processing additives, and tandem cell architecture.

Nanocarbons possess unique physical and chemical properties that can contribute to the enhancement of OPV performance, such as charge carrier mobility, thermal conductivity, mechanical strength, increased optical absorption and solubility in organic solvents. Nanocarbons also can improve the morphology of the active layer, which is critical to the optimization of OPV performance. The objective of this study is to utilize nanocarbons namely carbon nanotubes, nanodiamond and carbon black as additives and to synthesize composites with fullerenes (C60, C70) as charge carriers in OPV to improve power conversion efficiency (PCE).

Functionalized multi-walled carbon nanotubes (MWNTs) are used as additives to C70 to form a weak bonded composite, which result in better absorption and better phase separation. Consequently, PCE increases 70%. In another set of experiments, MWNTs are size sorted and MWNTs of different sizes are tested as an additive to the OPVs to

improve PCE. It has been found that the shorted MWNTs provide larger surface area for exciton dissociation and better phase separation and probably lead to less charge recombination. Therefore, they show higher PCE. Functionalized nanodiamonds (ND) are also introduced to C60 to synthesize C60-ND-COOH composite by taking the advantage of their small size distribution (4-5 nm) and modest charge mobility. The NDs have shown the ability to enhance short circuit current density and PCE. Finally carbon black (CB) is implemented into the P3HT/C60 OPV system and the effect of concentration is investigated. The addition of low concentration (12.5 ppm) of CB results in 35% improvement in short circuit current density, and 79% improvement in PCE.

In conclusion, the nanocarbons (MWNT, ND, CB) are promising additives for the performance enhancement of polymer photovoltaic cells and may work with diverse donor-acceptor systems.

NANOCARBONS AS CHARGE CARRIERS IN ORGANIC SOLAR CELLS

by
Xinbo C Lau

A Dissertation
Submitted to the Faculty of
New Jersey Institute of Technology
in Partial Fulfillment of the Requirements for the Degree of
Doctor of Philosophy in Chemistry

Department of Chemistry and Environmental Science

January 2014

.

APPROVAL PAGE

NANOCARBONS AS CHARGE CARRIERS IN ORGANIC SOLAR CELLS

Xinbo C Lau

Dr. Somenath Mitra, Dissertation Advisor — Date
Distinguished Professor of Chemistry and Environmental Science, NJIT

Dr. Carol A. Venanzi, Committee Member — Date
Distinguished Professor of Chemistry and Environmental Science, NJIT

Dr. Edgardo T. Farinas, Committee Member — Date
Associate Professor of Chemistry and Environmental Science, NJIT

Dr. Haidong Huang, Committee Member — Date
Assistant Professor of Chemistry and Environmental Science, NJIT

Dr. Pradyot Patnaik, Committee Member — Date
Consultant, Radiance

BIOGRAPHICAL SKETCH

Author: Xinbo C Lau

Degree: Doctor of Philosophy

Date: January 2014

Undergraduate and Graduate Education:

- Doctor of Philosophy in Chemistry,
  New Jersey Institute of Technology, Newark, NJ, 2014

- Bachelor of Science in Chemical Engineering,
  Yanbian University of Science and Technology, Yanji, P. R. China, 2007

Major: Chemistry

Publications and Presentations:

Lau XC, Desai C, Mitra S. Functionalized Nanodiamond as a Charge Transporter in Organic Solar Cells. Solar Energy. 2013;91(0):204-11.

Lau XC, Wang Z, Mitra, S. A C70-Carbon Nanotube Complex for Bulk Heterojunction Photovoltaic Cells. Applied Physics Letters. 2013;103(25).

Lau XC, Wu Z, Mitra, S. Enhanced Charge Carrier Transport through Shorter Carbon Nanotubes in Organic Photovoltaics Solar energy. Applied Materials & Interfaces. 2013 (under revision).

Lau XC, Mitra, S. Effect of Low Concentrations of Carbon Black in Organic Solar Cells. Nanoscale. 2013 (under review).

Lau XC, Mitra, S. Effect of Metal Decorated Graphene Oxide on the Performance of P3HT-C60 Photovoltaic Cells. 2013 (under preparation).

Lau XC, Li C, Mitra, S. Effect of Dye Doping on the Performance of P3HT-C60 and P3HT-C70 Photovoltaic Cells. 2013 (under preparation).

Lau XC, Wang Z, Mitra, S. Co-solvent treated Poly-3-hexylthiophene with C70 for Organic Solar Cells. 2013 (under preparation).

Wang Z, Chen K, Yan C, Wu Z, Lau XC, Somenath Mitra, Flexible secondary alkaline battery with carbon nanotube enhanced electrodes and polymer separator. 2013 (under preparation).

Lau XC, Desai C, Mitra S. Functionalized Nanodiamond as a Charge Transporter in Organic Solar Cells. Sustainable Nanotechnology Organization Conference, Nov. 4-6, 2012, Arlington, VA.

Lau XC, Desai C, Mitra S. Functionalized Nanodiamond as a Charge Transporter in Organic Solar Cells. NERM 2012 American Chemical Society 38th Northeast Regional Meeting, Sep. 30-Oct. 3 2012, Rochester, NY.

Lau, XC, Mitra, S. Nanocarbons as Charge Transporters in Organic Solar Cells. Dana Knox Student Research Showcase, Apr. 17, 2013, NJIT.

Lau, XC, Mitra, S. Nanocarbons as Charge Transporters in Organic Solar Cells. Graduate Student Research Day, Nov. 12, 2012, NJIT.

This dissertation is dedicated to my parents, my husband and my daughter, for their triumphant love and deep-seated support

ACKNOWLEDGMENT

I would like to extend my heart-felt appreciation and respect to my doctoral dissertation advisor, Dr. Somenath Mitra, who has generously shared his profound wisdom and who has been an exemplary role model during the time of my doctoral studies. I would also like to show my gratitude for his astounding cutting-edge pathways for my experimentations, which have always enthralled me and kept me inspired. I am also very indebted to Dr. Carol Venanzi, Dr. Edgardo Farinas, Dr. Haidong Huang and Dr. Pradyot Patnaik for serving on my committee and contributing beneficial comments.

I gratefully acknowledge the generous funding support financial support from National Institute of Health, and U.S. Army.

Special thanks go to the Department of Chemistry and Environmental Science for providing teaching assistant position, and to the assistant of the chair, Ms. Gayle Katz, for her support and understanding. I greatly appreciate the help that Ms. Clarisa González-Lenahan, as well as the staff of the Graduate Studies Office and the Office of the International Students and Faculty have offered to me during my studies. I would also like to give my thanks to Dr. Xueyan Zhang, who has guided and trained me to properly utilize instrumentations from York Center. I would also like to thank my colleagues for their friendship, assistance, and suggestions.

I am appreciative for the uplifting character building from my family members. They have been an important part of making me who I am. I would not have come this far without them.

TABLE OF CONTENTS

TABLE OF CONTENTS
(Continued)

TABLE OF CONTENTS
(Continued)

Chapter **Page**

LIST OF TABLES

LIST OF FIGURES

LIST OF FIGURES
(Continued)

LIST OF FIGURES
(Continued)

CHAPTER 1

INTRODUCTION

1.1 Objective

The rapid development of science, technology, standard of living and Gross Domestic Product have improved enormously; meanwhile, daily life has become more reliant on these advanced technologies which causes an increase in demand of energy. However, a price needs to be paid; the combustion of fossil fuels has polluted the air and in the future will be depleted. Therefore, a greater demand of renewable energy has been placed. In 2012, about 9 quadrillion Btu of renewable energy was consumed in the United States, which was about 9% of all energy used nationwide. Renewable sources provided about 12% of U.S. electricity generation in 2012. Renewable energy weighs in more and more each year in the supply of energy. When renewable energy becomes a more integrated source, the call for fossil fuels will become extinct. Non-biomass renewable sources of energy, such as hydropower, geothermal, wind and solar, are better energy choices, since they are much cleaner and more environmental friendly.

Since the discovery of photovoltaic effect in 19th century, solar energy, the most abundant and everlasting energy source, was studied and utilized to generate electricity. Photovoltaic (PV) cells have been researched on extensively since then. Till 2013, crystalline silicon solar cell holds the world record of power conversion efficiency (PCE) at 27.4%, which is still dominating the solar cell market. Thin film solar cell (CdTe) has the impressive efficiency of 18.3%. The third generation solar cell, organic solar cell, is emerging pretty quickly to 12% [1]. Organic photovoltaics (OPV) as a new, clean and sustainable energy resource candidate are excellent alternatives to conventional silicon

solar cells and thin film solar cells. However, commercializing OPVs and making OPV competitive to first generation and second generation solar cells could be very challenging. The objectives of this research are to:

- Synthesize and characterize functionalized nanocarbons with fullerene composites to serve as charge carriers in OPVs.
- Study the role of functionalized nanodiamonds (NDs) in charge transport in OPVs.
- Investigate the effect of functionalized carbon nanotubes (CNTs) in the acceptor phase.
- Study the effect of different lengths of carbon nanotubes in OPVs.
- Explore the effect of low concentration of carbon black (CB) as charge carriers in OPVs.
- Characterization of active layers and fabrication of solar cell devices.

1.2 Organic Solar Cells

In 1954, Bell Laboratories invented the first silicon solar cells with an efficiency of 6%. In the late 1970s, the conductivity of the polymer polyacetylene-by doping with halogens-was discovered by Heeger, Shirakawa, and Macdiarmid, for which they were awarded the Nobel Prize in Chemistry in 2000 [1].The first generation consists of the conventional single or poly-crystalline (mostly Si) solar cell, which is energy intensive and expensive in production. The second generation is said to consist of cheap thin-film technologies employing less crystalline absorbers and providing moderate efficiencies. Another classification describes the third generation of solar cells as cheap and efficient. Organic semiconductors are highly disordered, which allows easier and cheaper processing. They are organic solvent soluble and could be thermally vapored at low temperature; low cost processing techniques are available, ranging from inkjet printing to spin coating and

roller casting. They have several remarkable attributes, such as simple fabrication processes, low material cost, light weight, the ability to cover large areas, and tunable physical properties, making OPV attractive to both academic and industrial fields in the last two decades. In order to commercialize OPVs, the stability of the solar cell output performance against influences such as exposure to air and humidity is very crucial. It was shown by the company Konarka that the lifetime of encapsulated photovoltaic devices with a high performance on a roof-top was almost 2 years. Heliatek, the organic solar cells company, set the world record 12% in 2013. They are projecting that 15% of OPV efficiency could be achieved by 2015. If the efficiency could reach 15% and the lifetime could extend to 15 yrs., the price of OPV cell could be reduced to $0.36, which will make OPV competitive to the first and second generation solar cells.

Table 1.1 Product Attributes

Technology	Material ($/m^2)	Process ($/m^2)	Energy payback time (years)	Record Efficiency (%)	Cost ($/W)
C-Silicon	207	123	1.95	27.4	1.75
CdTe	50-60	86	0.75	18.3	0.94-1.2
OPV	**37**	**23-37**	**0.19**	**12**	**1-1.36**

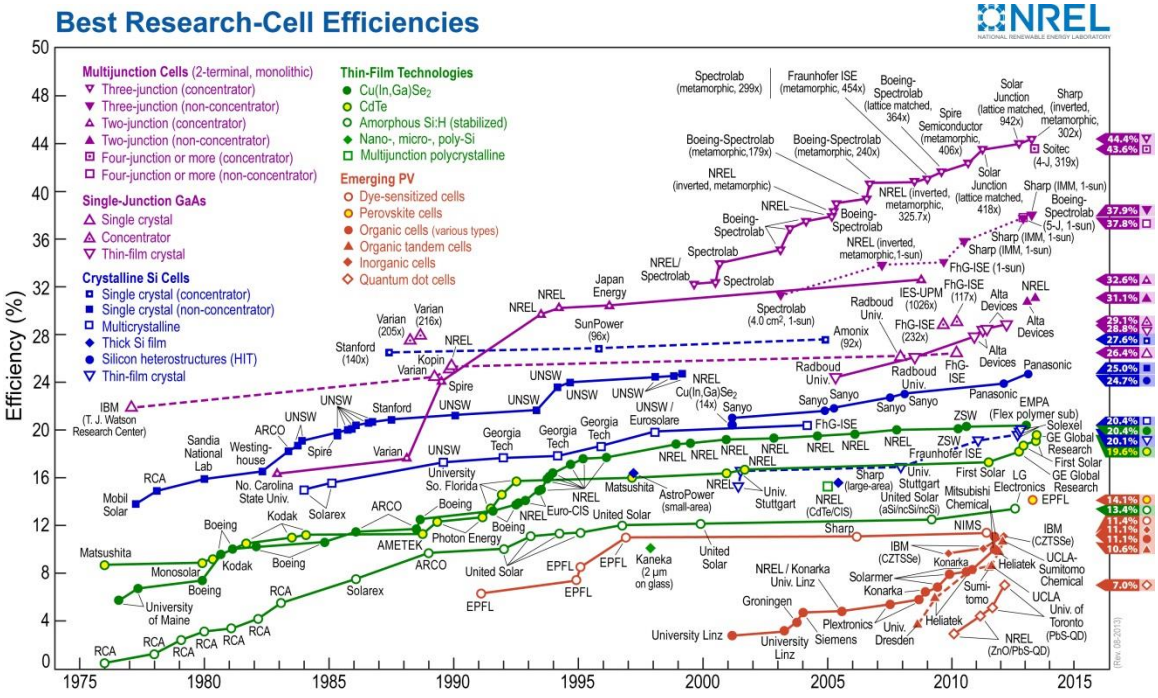

Figure 1.1 Best research-cell efficiencies.

Source: National Renewable Energy Laboratory

OPV consists of three categories, dye sensitized solar cell, polymer solar cell, and small molecule based solar cell. Polymer solar cell is the core of this work; it consists of three combinations: polymer /fullerene, polymer/polymer, polymer/quantum rod. For polymer/fullerene combination, the polymer is the light absorbing material, and fullerene acts as an acceptor. The ultrafast photoinduced charge transfer process between polymer and fullerene enables relatively high efficiency, such as Poly (3-hexylthiophene) (P3HT) / Phenyl-C61-butyric acid methyl ester (PCBM) with an efficiency of 5%. Polymer/polymer combination has the advantage of both components have high absorption coefficients and the ability of covering complementary parts of the solar spectrum. However, polymers have the tendency to have phase separation. The challenge is to find a n-type polymer with acceptor properties and good stability. Polymer/quantum rod combination has the

advantage of tunable bandgap by simply changing the particle size and they have high absorption coefficient as well. However, poor charge transport in quantum dots comprises the device performance.

The essential feature that differentiates OPV from inorganic solar cells is that still coulomb bounded electron-hole pair after illumination. For inorganic semiconductors under illumination, the generated excitons dissociate spontaneously into separated electrons and holes, since the binding energy for excitons in inorganic semiconductors is only around a few meV to hundreds meV. Take silicon as an example, the binding energy is around 0.1 eV, due to its high dielectric constant. However, for most of organic semiconductors, their dielectric constant is around 2 to 4, resulting in high binding energy in the order of 0.4 to 1 eV. The strongly bonded electron-hole pairs are diffusing in the donor phase rather than contributing to charge transport and generating current. Hence, an acceptor material is introduced to provide a driving force to separate the exciton. The offset between LUMO levels of the donor and the acceptor is the energy source, which is around 0.3 to 0.5 eV.

1.3 Bulk Heterojunction Solar Cells

1.3.1 Device Configuration and Basic Measurement

The air mass (AM) is defined as 1/cos(z) with the angle of incidence z measured to the vertical. This means AM describes the ratio of the actual path of a sunray through the atmosphere to the path of perpendicular incidence. The standard test condition for solar-cell characterization is AM 1.5 spectrum, corresponds to a solar zenith angle of z=48.2°. The integral over AM 1.5, the total energy flux, is defined as $1KW/m^2=100mW/cm^2$, the latitude of northern Europe and northern America.

The PCE η, which is the most important merit for characterizing the performance of a photovoltaic cell, is then defined as:

$$\eta = \frac{JmaxVmax}{Pinc} = \frac{FFJscVoc}{Pinc} \tag{1.1}$$

Where Pinc represents the incident power density and FF represents fill factor. Jsc is short circuit current density, Voc is open circuit voltage. These four parameters are the key performance characteristics of a solar cell. Jmax is the current at the maximum power point, and Vmax is the voltage at the maximum power point. The FF is defined as the ratio of the product of Jmax and Vmax and the product of Jsc and Voc, shown below:

$$\mathrm{FF} = \frac{JmaxVmax}{JscVoc} \tag{1.2}$$

It describes the "squareness" of the current-voltage curve.

External quantum efficiency (EQE) is the probability that an incident photon of energy E will deliver one electron to the external circuit.

$$EQE = \eta_{abs}\eta_{diff}\eta_{tc}\eta_{tr}\eta_{cc} \tag{1.3}$$

Where η_{abs} is photon absorption efficiency, η_{diff} is exciton diffusion process efficiency, η_{tc} is hole–electron separation process efficiency, η_{tr} is carrier transport process efficiency, and η_{cc} is charge collection process efficiency. Therefore, valuable information

about the quality of the semiconductor bulk and surfaces can be extracted from spectral measurements of quantum efficiency. Internal quantum efficiency (IQE) is another valuable parameter, EQE = η_{abs} IQE. In spite of the absorption efficiency of the materials, IQE offers a qualitative assessment of its ability to separate excitons into free charges and collect them at respective electrodes[2].

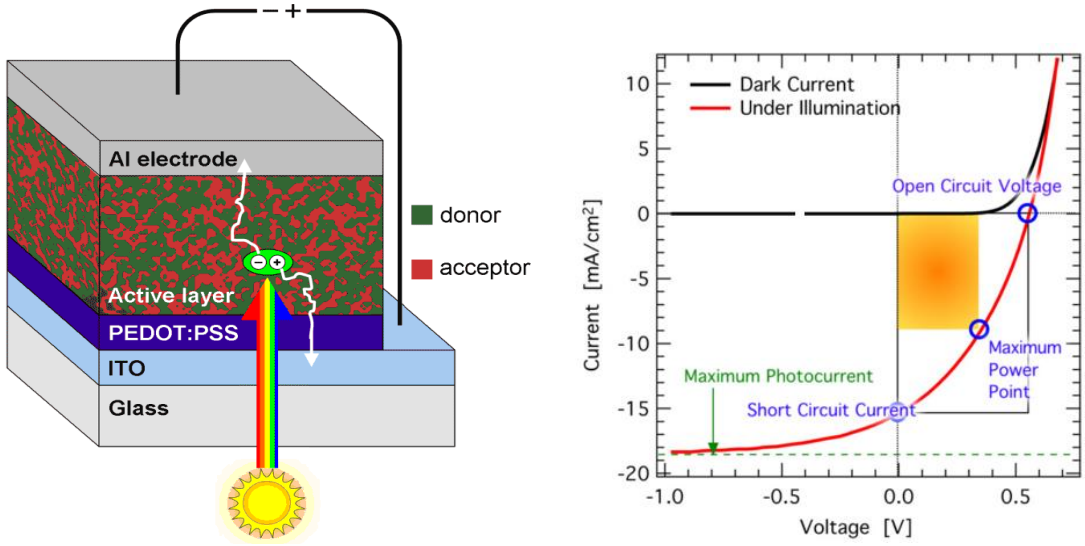

Figure 1.2 Typical bulk heterojunction solar cell configuration and schematic current-voltage characteristics of bulk heterojunction solar cells.

Source:http://www-ssrl.slac.stanford.edu/content/science/highlight/2011-01-31/effects-thermal-annealing-morphology-polymer%E2%80%93fullerene-blends-organic
Deibel C, Dyakonov V. Polymer–fullerene bulk heterojunction solar cells. Reports on Progress in Physics. 2010;73(9):096401.

It is undoubtedly that the key to enhance the performance of solar cells is to maximize Jsc, Voc and FF.

The FF parameter is greatly determined by the active layer morphology and the cell technology. As seen in Figure 1.2, an ideal characteristic of I-V curve under illumination is presented. The series resistance arises from both material resistivity and contact resistance. The shunt resistance arises from the leakage currents which means charge carrier losses

due to short-circuit pathways and carrier recombination [2]. An ideal device performance requires Rs close to 0 and Rsh close an infinite value.

Dark I-V curve measurements provide extra information about the cell. Most solar cells act like a diode in the dark, generating current under forward bias (V>0). Illuminated I-V curve of a solar cell is shown in the fourth quadrant and the current-voltage product is powder which is negative. That means the cell is a power generating device between 0 and Voc. At V<0, the illuminated device acts as a photodetector, dissipating power to generate a photocurrent. At V>Voc, the device dissipates power again and it behaves like a light emitting diode. Power is consumed through the resistance of the contacts and through leakage currents in a real solar cell.

The Voc is greatly dependent on materials properties, in particular the energetic relationship between the donor and the acceptor [3]. The energy difference between the ionization potential of the donor and the electron affinity of the acceptor governs the Voc value [4]. The maximum value of Jsc is largely governed by the optical band gap of the semiconductor. The smaller the optical band gap, the larger yield of maximum Jsc could be obtained [4].

1.3.2 Photoconversiton Mechanism

The physics behind organic solar cells is briefly reviewed in this section, and it is mainly focusing on bulk heterojunction solar cells. Bulk heterojunction is a concept firstly reported in Reference [2],[3] [5]. The basic operation of a bulk heterojuction solar cell is shown as a 5-step process in Figure The 5-step process includes light absorption, exciton diffusion, exciton dissociation, charge transport, and charge extraction.

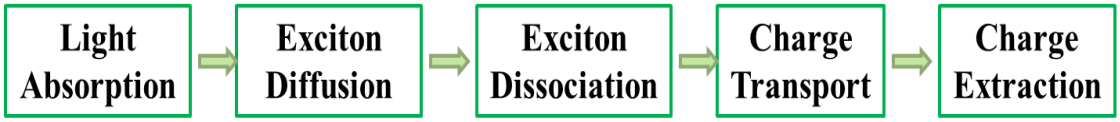

Figure 1.3 5-step process of photo conversion mechanism.

Photo conversion process starts with light absorption. In a bulk heterojunction solar cell, light is mostly absorbed in conjugated polymers, so-called the donor material. Organic semiconductors possess very high absorption coefficients above 10^7 m^{-1}. Therefore, in order to obtain a good absorption yield for most organic photovoltaic devices, the film thickness only need to be designed to be between 100 and 300 nm. When photons are absorbed by an organic semiconducting specimen of the polymer, an electron and hole pair with opposite spin are generated, called exciton which is bound by their Coulomb attraction. The neural excitons are diffusing to the donor and acceptor interfaces, not affected by the applied electric field. The relative dielectric constant of organic semiconductors is as low as 2 to 4, which with a Coulomb binding energy around 1 eV, as compared to inorganic semiconductors as high as 10, which with a Coulomb binding energy around 0.1 eV. That makes excitons generated in organic semiconductors very difficult to dissociate into a separated electron and hole at room temperature, and resulted in strongly bound Frenkel-like localized excitons. In order to enhance the PCE, a better matching absorption spectrum of the polymer to the solar spectra could be employed. This could be achieved by designing low band gap polymers, which generally refers to polymer with band gap lower than 2 eV and absorbs light with wavelength longer than 620nm. The energy band gap of semiconducting polymers could be tuned as low as 0.5 eV, which could increase the light absorption and hence the theoretical current. However, Voc is greatly

dependent on the difference between the highest occupied molecular orbital (HOMO) level of the donor and the lowest unoccupied molecular orbital (LUMO) lever of the acceptor; therefore, decreasing the band gap of the polymer also could result in decreasing Voc and device performance. An optimal band gap is 1.5 eV, based on the alignment of the energy levels to achieve high V_{OC} and an efficient charge transport from the donor polymer to the acceptor fullerene.

After light is absorbed by the donor material, the exciton has to diffuse to the donor and acceptor interface to be dissociated; otherwise, they would recombine and decay by photoluminescence. The diffusion length is expressed as,

$$L_D = \sqrt{D\tau} \tag{1.4}$$

Where D is diffusion coefficient and τ is lifetime of the exciton. The higher the diffusion coefficient, the longer the lifetime, resulted in further distance the exciton can go before it recombines. The diffusion length of the exciton in organic materials is typically in the range of 10 nm or less. The diffusion length for P3HT is 4nm, and for C60 is 40nm [6]. However, an optimum thickness of the donor layer is required around 50-100nm for good yield devices, which means that 10% to 20% excitons might get to the interface to be split and contribute to charge generation. To overcome this dilemma, the concept of bulk heterojunction was utilized and an intimate percolation path is created for more efficient electron and hole transportation.

Once the excitons diffuse to the D/A interface, exciton dissociation should occur at the D/A interface. In most polymer/fullerene organic solar cells, charges are generated by

photoinduced electron transfer. Exciton dissociation only happens when the photoinduced electron transfer process is energetically favorable [6]. The driving force is the energy difference (offset) between LUMOs of the donor and the acceptor, and a minimum energy difference of 0.3 eV is needed in order to make exciton splitting and dissociating happen. Excess energy difference between the LUMOs doesn't appear to favor the exciton dissociation more, rather than become wasted energy that doesn't enhance the device performance [3]. Photoinduced electron transfer occurs extremely fast, with a time constant of~ 45 femtoseconds at the conjugated polymer/fullerene interface at room temperature. If the excitons fail to reach the interface within the diffusion length, they tend to recombine (μs) and decay to the ground state within a few ns. Therefore, exciton dissociation is the essential step of the photo conversion process. In order to yield optimal power, the excitons have to be dissociated efficiently and collected at electrodes before other competitive processes happen [7]. Nanocarbons, such as carbon nanotubes, could provide extensive D/A interface to enhance exciton dissociation efficiency.

After the excitons are separated, charges have to be transported through the organic materials to respective electrodes. The holes will travel through the donor material to the anode which is indium tin oxide (ITO), while the electrons will travel through the acceptor material to the cathode which is Aluminum (Al) in this work. Charge transport mainly takes place by hopping from one molecule to the next, then hops towards the electrodes where they can be extracted to generate a photocurrent [4, 8]. In a bulk heterojunction, the increased D/A interface strategy helps exciton dissociation. On the other hand, the connected percolation pathways of both materials to both electrodes provide more opportunity of separated charges encounter each other at the D/A interface and recombine

non-geminately. Therefore, a cost paid at compromised charge mobility and charge extraction efficiency. In order to higher the charge carrier mobility, optimizing nano structural material phases could be achieved by introduction nanocarbons to the active layer.

Finally, when dissociated charges reach an electrode, they have the potentiality to be extracted; however, a poor electrode interface may prohibit this to happen. Normally, the substrate-supported transparent electrode is ITO with work function of 4.8 eV, serves as anode. The reason for the popularity of ITO is that it possesses both electrical conductivity and optical transparency, in addition that it can be deposited as a thin film. The counter metal electrode is Al with work function of 4.3 eV, serves as cathode. Al cathode is deposited by thermal deposition in vacuum through a shadow mask.

Several detrimental charge collection scenarios include: charges are extracted at the opposite polarity electrode, charges are recombined through defects (e.g., metal penetration into active layer). Buffer layers can be inserted to improve charge selectivity and alleviate this effect. A layer of poly(3,4-ethylene dioxythiophene): poly(styrene sulfonate) (PEDOT:PSS) is a popular option, its work function is 5.0 eV, and conductivity is around 1S/cm [9]. It is used as a hole conducting and transporting layer. In addition, it works as a smoothing layer between ITO and active layer, and increases the work function even further as well [10].

1.3.3 Active Layer

The core conceptual design of the active layer for heterojunction solar cells is the utilization of two materials with different electronic levels. One is so-called donor which is an easily oxidized, p-type, low ionization potential and electron accepting organic material;

the other one is so-called acceptor which is easily reduced, n-type, strongly electronegative, high electron affinity and electron accepting organic material. The donor and acceptor have different electronic levels [5, 11, 12]. The energy offset is necessary to dissociate strongly bounded excitons, which is achieved at the interface of the donor and acceptor.

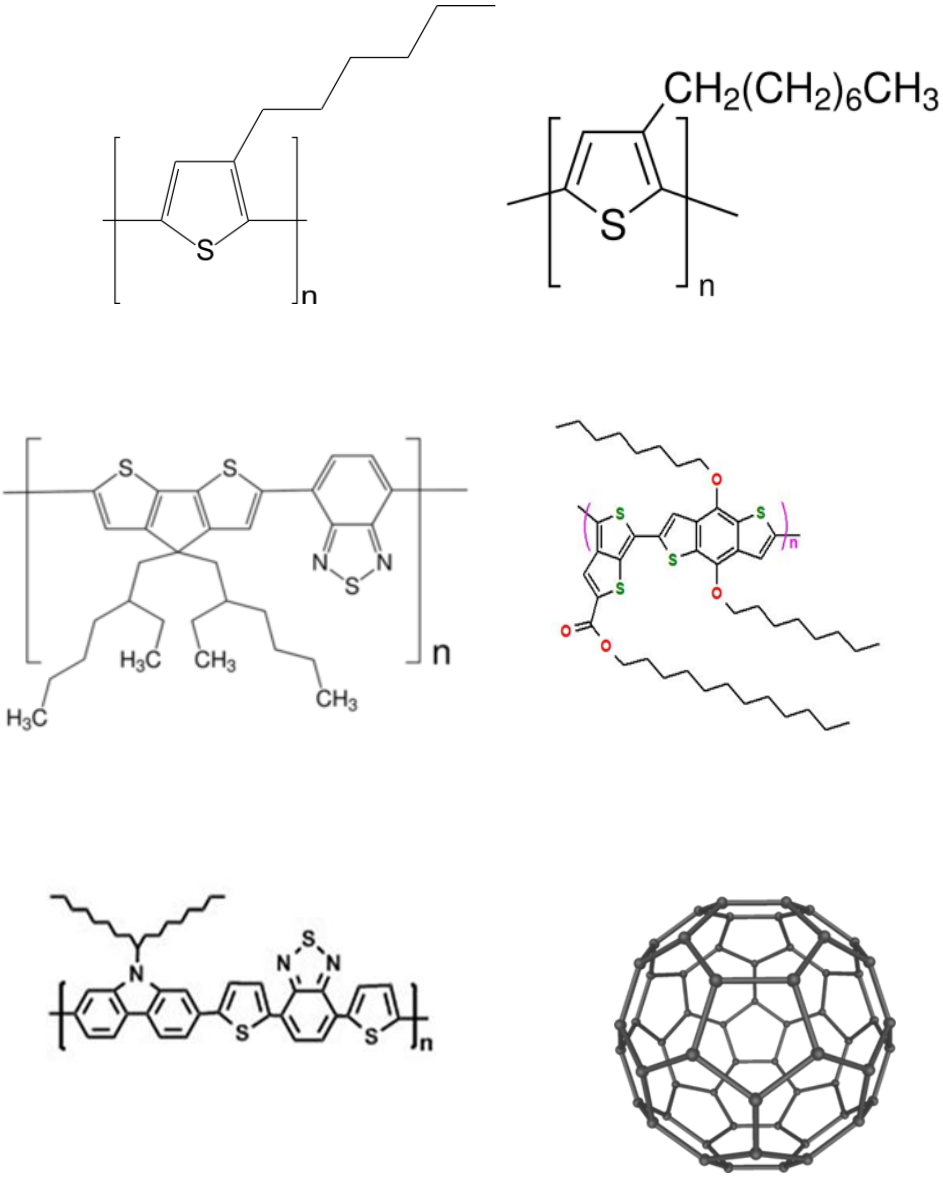

Figure 1.4 Chemical structures of semiconductors in OPV: P3HT, Poly(3- octylthiophene -2,5-diyl) (P3OT), Poly[2,6-(4,4-bis-(2-ethylhexyl) -4*H*-cyclopenta [2,1-*b*;3,4-*b*′] dithiophene)-*alt*-4,7(2,1,3-benzothiadiazole)] **(**PCPDTBT), poly((4,8-bis(octyloxy)benzo (1,2-b:4,5-b')dithiophene-2,6-diyl)(2-((dodecyloxy)carbonyl)thieno(3,4-b)thiophenediyl)) (PTB1), Poly[[9-(1-octylnonyl)-9H-carbazole-2,7-diyl]-2,5-thiophenediyl-2,1,3-benzothi adiazole-4,7-diyl-2,5-thiophenediyl] (PCDTBT), C60, C70, PCBM.

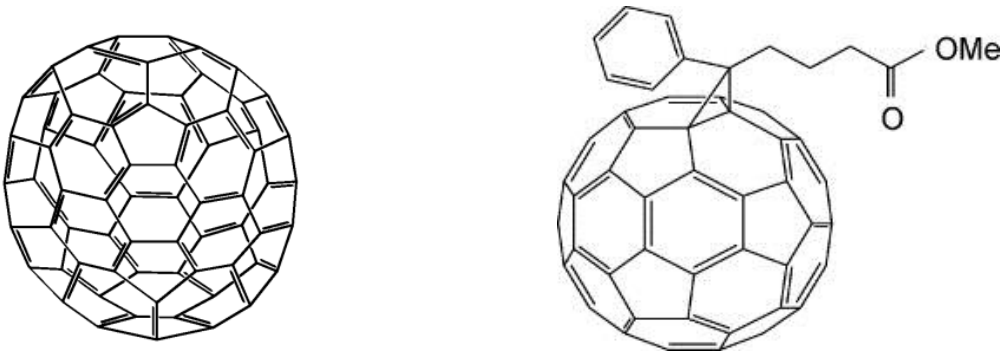

Figure 1.4 Chemical structures of semiconductors in OPV: P3HT, Poly(3- octylthiophene -2,5-diyl) (P3OT), Poly[2,6-(4,4-bis-(2-ethylhexyl) -4*H*-cyclopenta [2,1-*b*;3,4-*b*′] dithiophene)-*alt*-4,7(2,1,3-benzothiadiazole)] **(**PCPDTBT), poly((4,8-bis(octyloxy)benzo (1,2-b:4,5-b')dithiophene-2,6-diyl)(2-((dodecyloxy)carbonyl)thieno(3,4-b)thiophenediyl)) (PTB1), Poly[[9-(1-octylnonyl)-9H-carbazole-2,7-diyl]-2,5-thiophenediyl-2,1,3-benzothi adiazole-4,7-diyl-2,5-thiophenediyl] (PCDTBT), C60, C70, PCBM.

The origin of electrical conductivity in carbon-based semiconductors is conjugation, the alternation of single and double bonds between carbon atoms. The ground state configuration of carbon atom is $1s^2 2s^2 2p^2$. Minimizing the free energy during bonding is desirable, in the case of conjugated polymers; hexagonally directed orbitals which are $sp^2 p_z$ hybridized are formed. The backbone is created by the three in-plane sigma (σ) orbitals of the sp^2 hybridized carbons. The fourth electron locates in the p_z orbital, which is perpendicular to the σ orbitals. The p_z orbital overlaps with the neighboring p_z orbital and form a π bond, which results in delocalized charges. Decoupling the p_z electron from the backbone originates special electrical properties for conjugated polymers. Typically, excitations within the π-band do not cause bond breaking, which account for the valuable photo-conductive properties of π-conjugated polymers. The band gap between the HOMO LUMO is typically in the range of 1-3 eV, making such an organic compound a semiconductor. Moreover, such range of the band gap enables conjugated polymers to access the visible light. The semiconducting and light absorbing properties make

conjugated polymer very attractive for OPVs. In this work, Poly (3-hexylthiophene) P3HT was used as a donor in all the systems. However, different acceptor materials were experimented, such as C60, C70 and PCBM [13].

P3HT has been a most interesting and popular hole accepting semiconductor for OPV [14, 15]. It has a bandgap of 1.9 eV, with the HOMO and LUMO levels at 5.2 and 3.3 eV, which covers only 30% of the AM 1.5 solar photon flux [16]. P3HT like other organic semiconductors has high absorption coefficient in the order of $10^5 cm^{-1}$, which enables conjugated polymers absorb light very efficiently corresponding to the solar spectrum. Consequently, a thickness of a few hundreds of nanometers (100-300 nm) is sufficient to absorb good yield of light for organic semiconductor devices. Additionally, P3HT exhibits fairly high hole mobility ($\sim 10^{-4}$–10^{-3} cm^2/Vs) [17, 18].

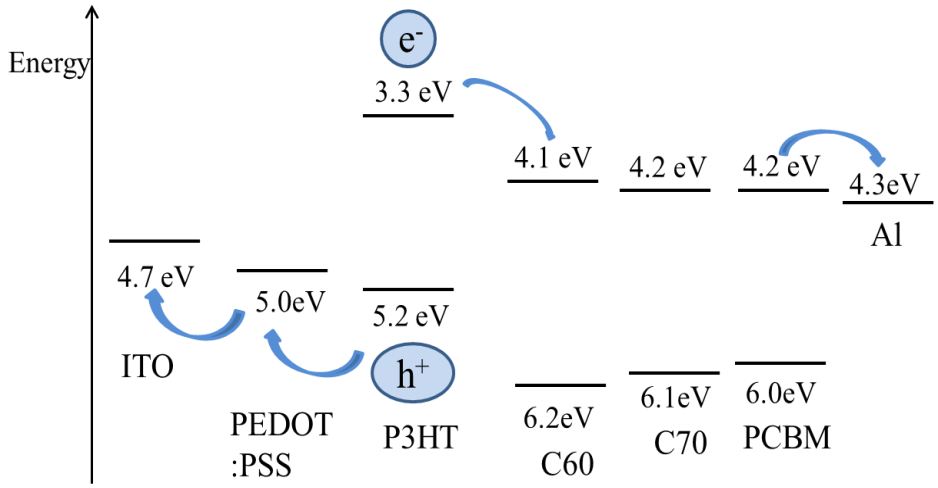

Figure 1.5 An energy diagram of donor and acceptors used in this work.

Fullerenes and their derivatives have several remarkable attributes to serve as electron acceptors in bulk heterojunction solar cells [19, 20]. In the case of C60, these 60 carbon atoms are $\sim sp^2$ hybridized and arranged in 12 pentagons and 20 hexagons to form a

spherical molecule with a nucleus diameter of 0.7 nm. From an energetic standpoint, C60 has a deeper LUMO energy, comparing to other potential electron donor materials, which means high electron affinity. This is energetically favorable for efficient exciton dissociation and charge transfer from the donor to fullerene. Additionally, the triply degenerate LUMO enables C60 to accept up to six electrons in its cage. The HOMO and LUMO levels of C60 are 6.2 and 4.1eV, respectively (Figure 1.5). C60 films can also form crystalline structure with high electron mobility, which favors maximizing photocurrent. The high electron mobility is due to excess electrons can be efficiently stabilized by conjugation in the molecule. From a processing standpoint, C60 has a modest solubility (27mg/ml) in ODCB [21, 22], which allows both donor and acceptor materials well mixed and dissolved in the same solvent and be able to deposited.

Passing to C70 molecule, it can be considered as an addition of a ring of five hexagons along the equatorial plane of C60. For that reason, C70 has relatively less symmetrical structure. C70, a higher molecular weight fullerene in the shape of a rugby ball, has a bandgap around 1.9 eV, and the HOMO and LUMO levels are 6.1 eV and 4.2 eV, respectively. However, it has higher absorption in the visible region than C60, and this could lead to higher efficiency. Moreover, C70 has better solubility (36.2 mg/ml) than C60 in ODCB [23-25]. Hence, C70 was used in this work as an alternative to C60, which is in detailed in Chapter 3.

In order to optimize the acceptor materials furthermore, PCBM was synthesized by Hummelen and Wudl in 1995 [26]. It leads to good solubility in organic solvents such as chloroform, chlorobenzene, dichlorobenzene, etc., by adding side-chains to enhance the solubility above 100 mg/ml [27]. PCBM has a bandgap around 1.8 eV, with the HOMO

and LUMO levels at 6.0 eV and 4.2 eV, respectively. PCBM films exhibit amazingly high electron mobility ($\approx 10^{-3}$ cm^2/Vs), as was determined by the Blom group [28]. These properties of PCBM enhance generation of photocurrent and better performance of OPV devices. However, the complicated synthesize processes hinder the widely utilization of PCBM for large scale commercialization [29]. Control system based on P3HT/PCBM is discussed in Chapter 4.

1.4 Nanocarbons

Carbon, an abundant material and a potential alternative as a replacement of Silicon, holds notable potential as a material for solar cells. It can be found in various forms ranging from insulator, to semiconductor, metallic/semi-metallic graphite (or graphene) [30]. Nanocarbons, such as single–walled carbon nanotubes (SWCNT), Multi-walled carbon nanotubes (MWNT), fullerenes, graphene and their chemical derivatives, have been intensively studied in the past two decades. The unique and interesting optoelectronic, physical and chemical properties of these materials make them very valuable for improving OPV performance, including carrier mobility, thermal conductivity, mechanical strength, optical absorption, and their ability to be dissolved in organic solvents to deposit thin solar cell active layers from solution. Other carbon allotropes, for instance amorphous carbon (such as carbon black (CB)) and nanodiamonds (NDs), can be deposited in thin film form on flexible substrates by means of chemical vapor deposition [31-33]. Nanocarbons are important for many applications due to advantages such as wide electrochemical window, good electrical conductivity, and long-term stability (shown in Table 1.2).

Table 1.2 Properties of Nanocarbons

	CNT	**Nanodiamond (DND)**	**Carbon Black (CB)**
Electron mobility (cm2/Vs, 300K)	10^8	4500	Conductivity $0.1\text{-}10^2$ $(\Omega cm)^{-1}$
Hole mobility (cm2/Vs, 300K)	10^3	3800	----------
Surface area (m^2/g)	50 to 1315	200-450	150-250
Size	MWNTs: Original 500-2000 nm Long 1695 nm Short 123 nm	4-5 nm, Aggregation 150-200 nm	<500 nm
Cost	50 $/g (SWNTs) 5 $/g (MWNTs)	86.5$/g	24.6 $/g

1.4.1 Carbon Nanotube

CNTs possess unique physical and electrical properties, making CNTs with high purity can behave as a transparent electrode to replace ITO glass in solar cell devices, as reported by Wu Z et al. [34]. On the other hand, CNTs was employed as acceptor materials firstly by Kymakis and Amaratunga in 2002. However, the PCE is very low (<0.1%) [35]. The investigation of CNTs as additives to the active layer has been explored intensively. CNTs act as exciton dissociating sites and ballistically conductive agent with high carrier mobility [24, 30].

The structure of CNT consists of cylindrical graphene sheet rolled up into a seamless cylinder whose diameter in the order of a nanometer and length is the order of a

micrometer. Thus, the length to diameter ratio exceeds 10^3 [2]. This allows percolation pathways created at appropriate low doping levels and provides a high surface area, which could be a suitable morphological architecture for exciton dissociation, more efficient charge transfer to the proper electrodes [2]. CNTs in their pristine form are rigid, chemically inert, and difficult to dissolve in water or organic solvents. In order to obtain homogenous mixtures of CNTs with different organic, inorganic, and polymeric materials to act as an additive, some level of functionalization is required to the addition of certain molecules or functional groups onto their sidewalls without significantly changing their physical/electronic properties. Functionalization of CNTs can be done through covalent bonding to the tips, sidewalls and defects of tubes. Carboxyl group (-COOH) and amide are formed at the ends of tubes as well as at the defects on the sidewalls by oxidation.

Both SWNTs and MWNTs have been introduced in photovoltaic devices as additives lately [24, 36-40]. The CNTs not only act as electron acceptors but also provide high field at the polymer/CNT interfaces for exciton dissociation [40]. Application of carbon nanotubes CNTs in organic photovoltaic device is of great interest. It has been demonstrated that CNTs along with conjugated polymers favor charge transportation and exciton dissociation. CNTs can improve exciton dissociation by providing field at the polymer nanotube interface. A blend of CNTs with conducting polymer allows formation of devices with high interfacial area, which can lead to a large pair dissociation region. These properties of CNTs with conjugated polymer have generated a great interest in developing photovoltaic devices [41].

1.4.2 Nanodiamond

Detonation-synthesis NDs were first synthesized in 1963 by detonation of a mixture of carbon-containing material with explosives [14]. NDs have a complex structure usually consisting of three layers: a diamond core (sp^3) 4-6 nm in size, comprised of 70% to 90% of the total number of carbon atoms; a transient carbon shell (sp^{2+X}) encircling the core and containing X-ray amorphous carbonaceous structures 0.4 -1.0 nm thick, comprised of 10% to 30% of the total number of carbon atoms; and a surface layer (sp^2) comprised of various functional groups. The surface groups were including hydroxyl groups (OH), carboxyl group and tertiary alcohol, amide groups, hydrocarbon groups (C-H) in the form of CH, CH_2 and CH_3, carbonyl groups (C=O) in the form of ketone, carboxyl group, acid anhydride, ester and lactone, C-O-C groups in the form of ether, acid anhydride, lactone and epoxy group.

ND particles have a large specific surface area (200-450 m^2/g) and hence their surface groups greatly affect their physical and chemical properties. Specific modification of NDs could be achieved by controlled functionalization, which offers a powerful tool to involve NDs in various chemical reactions and enhance their interaction with solvents, components of composite materials, polymers and catalysts. Therefore, many applications have been found incorporating NDs with other components. NDs possesses high surface area, good mechanical properties, low cost and relatively high conductivity, therefore, they offer attractive properties for energy storage applications, such as electrochemical capacitors, also known as supercapacitors [42].

The relatively inexpensive large scale production of ND by a detonation synthesis process has made them commercially viable for a broad range of applications.

1.4.3 Carbon Black

The structure of commercial CB is known to have both crystalline carbon (graphite) and amorphous carbon, where the aggregates tend to form through Van der Waals forces. Moreover, functional groups including ketone, ether, ester, quinone, carboxyl, phenolic and hydroxylic groups are known to be present in CB [43]. In this work, graphitized mesoporous carbons (GMCs) were used. The structural features of GMCs include structural homogeneity with significant graphite-like domains and stacking heights, in combination with the high surface area, the enhanced conductivities of GMCs have also been harnessed for their use in high performance components in electrochemical applications [17]. Examples include electrodes for double layer capacitors, and binding materials. The nanostructure of the GMC possesses a pentagonal configuration with an approximate diameter of 35 nm. These primary nano-particles form aggregates in the 175 nm size range. Further agglomeration of the material leads to particle agglomerates in the 400 nm range. CB is electrically conductive with conductivities ranging from 0.1 to 10^2 S/cm at ambient temperature [1]. They impart good conductivity to polymers and have been widely used as fillers in polymers for applications such as conductive packaging for electronics [2], and as fuel cell electrodes [3],[44]. CB also shows high absorption of the solar spectra [45].

1.5 Nanocarbons Incorporated Composites in Organic Solar Cells

In order to utilize nanocarbons as additives in the active layer in OPVs (shown in Figure 1.6), several approaches have been explored. CNTs have been extensively studied and have been incorporated in OPVs by several groups. The fundamental understanding of the

electrical role of CNTs is still not quite clear. CNTs have been introduced into fullerene by sonication [46], they also have been incorporated with fullerene by microwave irradiation [36-38, 47]. On the other hand, CNTs have been employed with conjugated polymer by low power sonication as well [39]. With a proper concentration of CNTs, Jsc has been improved and hence the enhanced performance of OPVs has been revealed [24]. Few groups have incorporated NDs into the active layer, enhanced absorption spectra, increased Jsc and improved PCE have been explored [48-50].

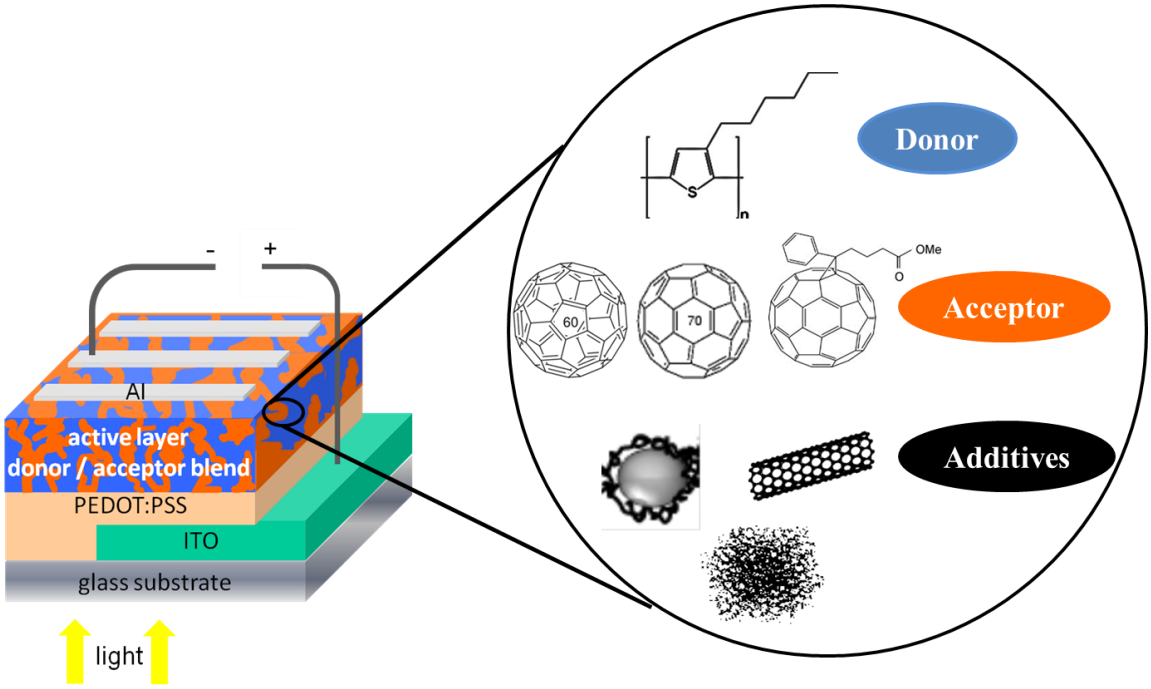

Figure 1.6 Nanocarbons as additives in OPVs.

The microwave irradiation method of synthesizing nanocarbon-composite has been utilized in this work. It is known that fullerene molecules tend to polymerize under high temperature, pressure, and under UV irradiation [47, 51]. Under microwave irradiation, nanocarbons (CNT, CB, ND) serve as heated nuclei. Fullerene molecules could attach to the functional groups on the surface of nanocarbons, or react with the nanocarbons at their

defect sites. The additional C60/C70 molecules tend to aggregate with the already attached C60/C70 molecules due to polymerization of fullerenes under microwave irradiation. The mechanism for C60-ND, C70-CNT and C60-CB is shown in Figure 1.7, respectively.

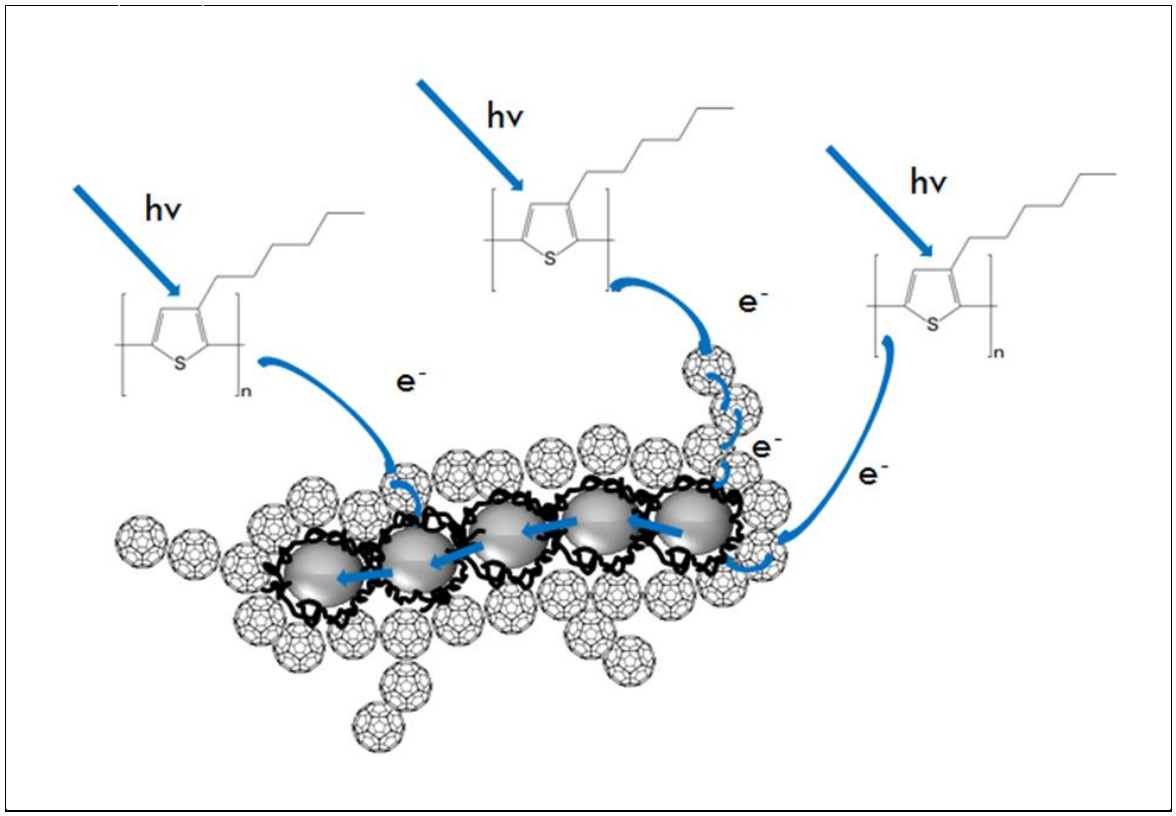

Figure 1.7 Mechanism of charge separation at polymer-fullerene interfaces, and followed by more efficient charge transfer to nanocarbons.

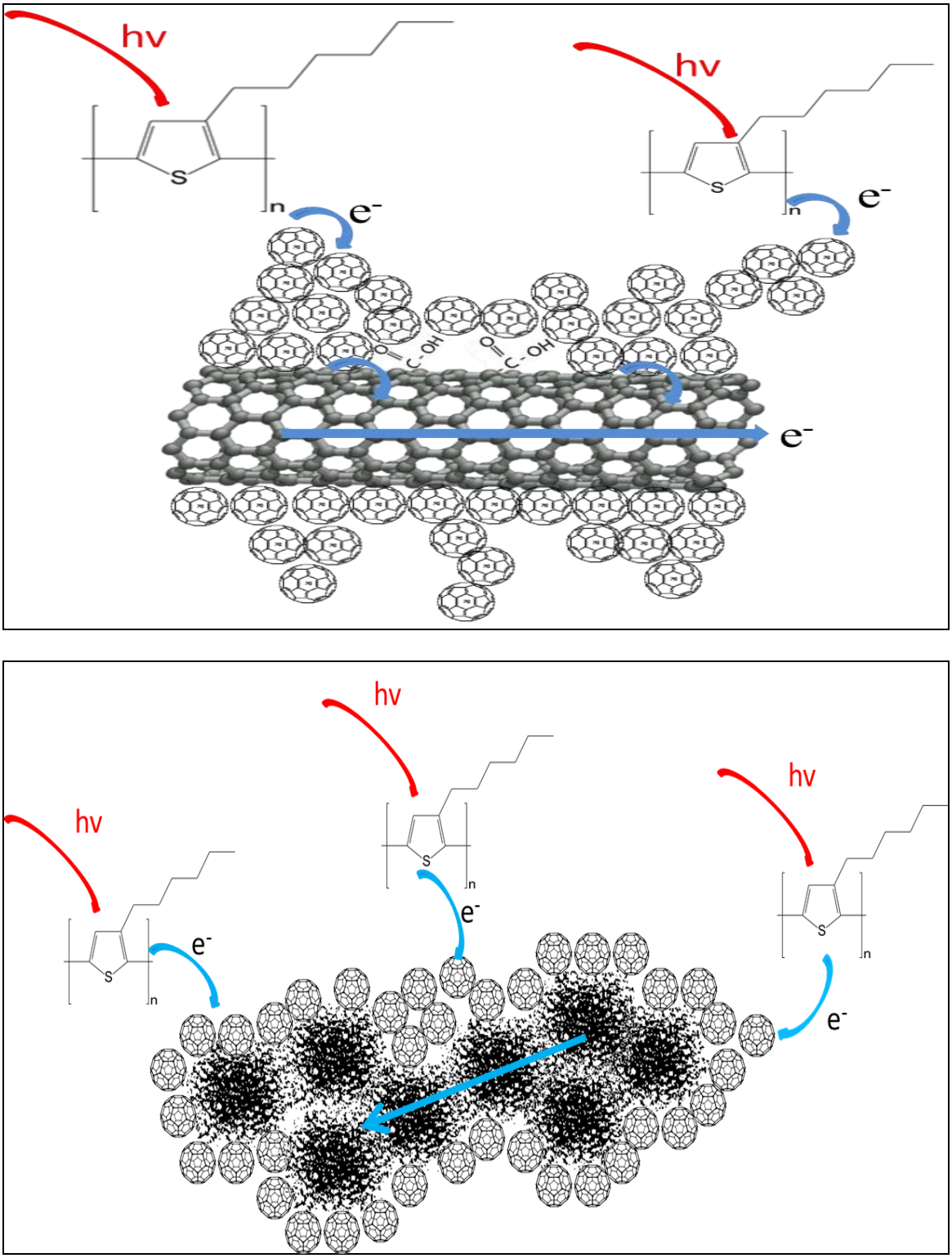

Figure 1.7 Mechanism of charge separation at polymer-fullerene interfaces, and followed by more efficient charge transfer to nanocarbons.

1.6 Fabrication of Solar Cells

Fabrication of organic solar cells is quite a delicate and sophisticated process. ITO coated glass first is cut into 25 mm×25 mm, then they are cleansed by detergent, rinsed with water and sonicated in isopropanol and then acetone, after that they are dried by compressed air. In order to get the effective area, office tape has been used to cover the needed ITO area, 5 mm. Then the sample is etched in a mixture of hydrochloride and nitric acid on a hot plate. 10-15 min is needed to remove the unwanted ITO area and conserve the tape covered ITO area. The cleansing process is repeated to get rid of the acid on the surface of glass and keep the sample clean and dust free. Then PEDOT PSS is filtered and ready to apply onto the sample. Spin coater is used to get a uniform thin film of 30 nm at 2700 rpm for 50 sec, the sample is moved to an oven to be dried for 30 min at 100°C. Then filter the active layer blend and spin-coat the solution at 400 rpm for 15 sec and followed by 780 rpm for 5 sec to get a 100 nm thick film. Then leave the cover on for 5 min to let the film slow dry.

After that, samples are placed on the sample holder and covered by a shadow mask to get an intersection area of 5 mm×5 mm. Then samples are transferred into the thermal evaporator to coat Al electrode. This takes about 2 hr. Finally the samples are fabricated. However, they need to get post production treatment, annealing. Annealing is carried out in a nitrogen filled glovebox on a hotplate at 125°C for 10 min. Then the samples are ready to be tested I-V curve in the dark and under illumination. The solar simulator is calibrated by thermopile detector for every measurement, and the intensity is 95 mw/cm^2.

Since the fabrication process is down to nanometer scale, several important steps need to be noted. The first step is dispersion of nanomaterials. Both donor and acceptor materials are selected to dissolve in the same solvent, and for my work, nanocarbons have

to be manipulated to be introduced into the system as well. Sonication and microwave irradiation are the two main approaches. As shown in Figure 1.8, active layer solutions with nanocarbons are uniform solutions. Second step is optimizing film thickness, has been done by adjusting the spin speed and spin time. Both thickness and diffusion length need to be considered to get enough absorption and efficient exciton dissociation.

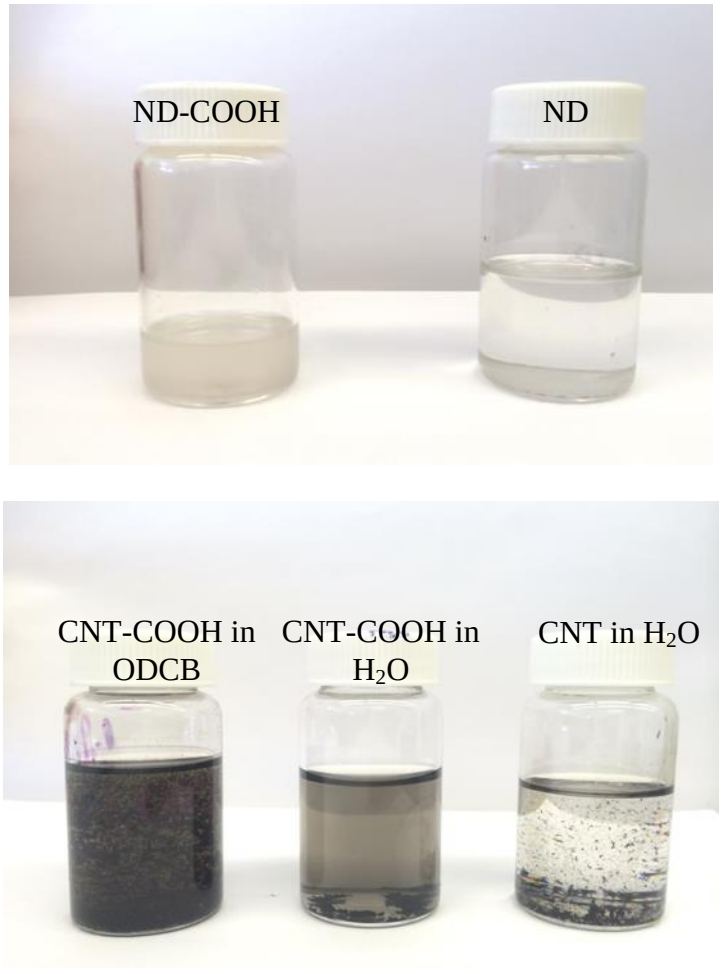

Figure 1.8 Photographs of different nanocarbons in ODCB and H_2O, and active layer solutions.

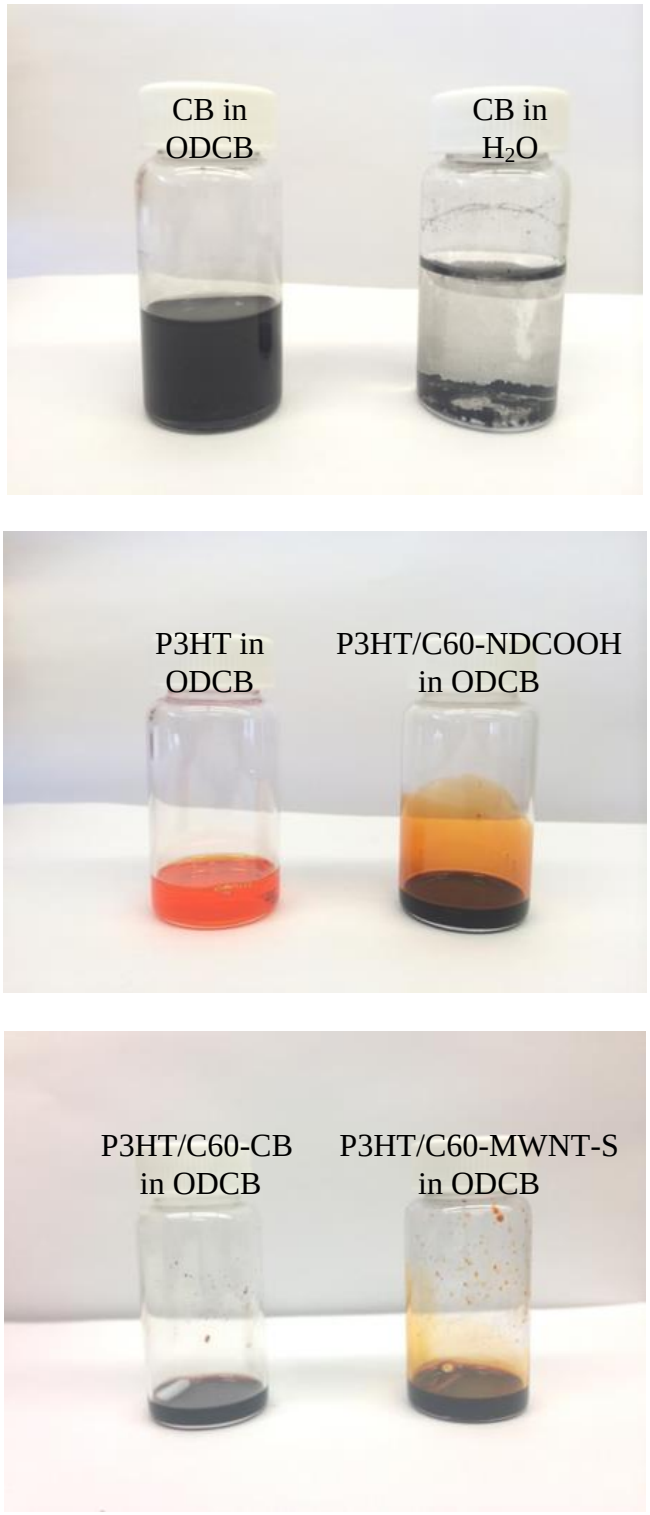

Figure 1.8 Photographs of different nanocarbons in ODCB and H_2O, and active layer solutions.

Electrode deposition is done by thermal evaporator as seen in Figure 1.9. Thermal evaporation is a method to deposit metal thin films. Vacuum chamber pressure, source material purity, and evaporation rate are the variables to control the metal evaporation. The pressure of the vacuum chamber needs to be maintained around 5×10^{-7} torr to ensure good quality deposition. When the deposition is conducted at pressure higher than 1×10^{-6} torr without reaching lower pressure, hot vaporized metal particles will react with remaining oxygen molecules to form metal oxide. Deposited films with this condition lose metallic reflection and electrical properties. In order to get high quality thin films, material purity over 99.99% is essential. High purity source material will lower the chance of side reactions or impurity formation during evaporation. The evaporation rate is in the range of 1Å /sec to 3 Å /sec. Source materials should be evaporated slowly to protect the active layer, which can be damaged by hot vapors.

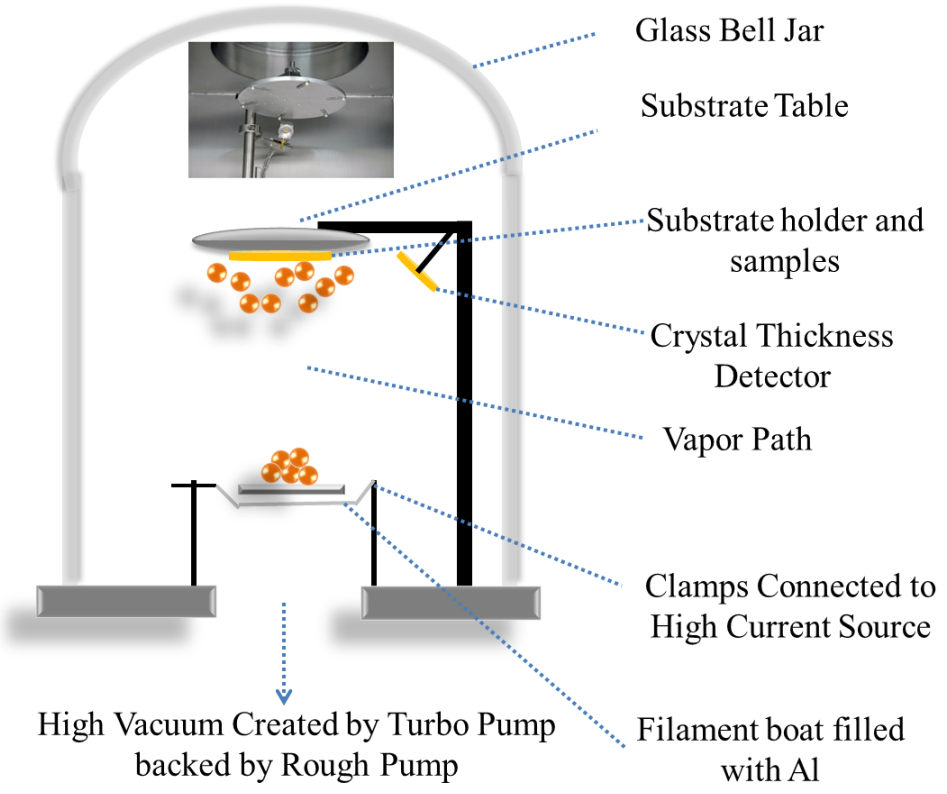

(a)

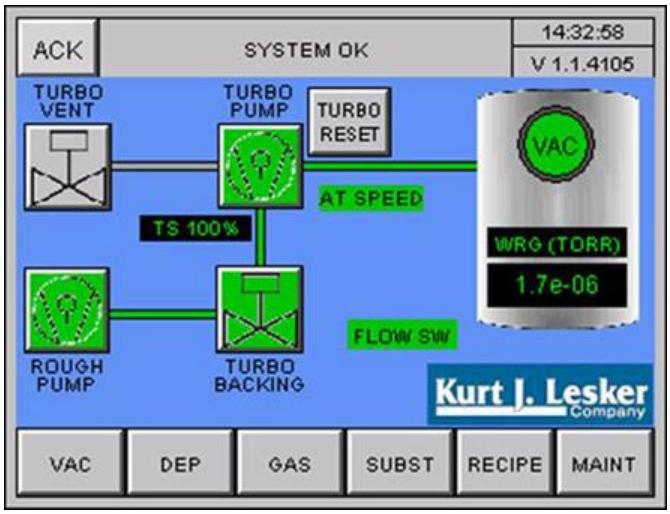

(b)

Figure 1.9 (a) Deposition of thin film of Al, (b) operation screen (c) thermal evaporator.

(c)

Figure 1.9 (a) Deposition of thin film of Al, (b) operation screen (c) thermal evaporator.

A lot of affords have been done to optimize film morphology. First is solvent selection, important parameters are the boiling point which is related to the evaporation rate, the viscosity and the solubility of polymers. High boiling point solvents are better choices, because of the low evaporation rate of these solvents, the drying time is increased and the polymers tend to show higher ordering. The boiling point of ODCB is at 180°C. Thermal annealing involves two main structural evolutions: crystallization and phase separation including coarsening. The structural evolution begins with crystallization of P3HT, followed by diffusion of PCBM and finally, aggregation of PCBM. It also enhances interface properties due to reduced interface defects, such as pores, trapped solvent. Solvent annealing is a method to leave the spin coated sample inside a covered petri dish for a certain time or until the film color has completely changed.

CHAPTER 2

EFFECT OF SHORTER FUNCTIONALIZED MULTIWALL CARBON NANOTUBE AS A CHARGE CARRIER IN ORGANIC SOALR CELLS

2.1 Introduction

The OPVs are excellent alternatives to conventional silicon and thin film solar cells because they attempt to achieve moderate PCE at significantly lower cost. Typical OPVs are based on the creation of bulk heterojunctions consisting of blends of an electron-donating semiconducting polymer and an electron-accepting molecule such as fullerene (C_{60}) or its derivative [3, 16, 33, 47, 52-56]). Improvement in OPVs can be brought about by addressing some of its limitations, namely, improving absorption of a wide range of the solar radiation spectrum [10, 57], and enhancing the electron and hole mobilities. Moreover, components like PCBM that require multistep synthesis are quite expensive, underscoring a key economic advantage of OPVs [36] .

In spite of relatively high V_{OC} and high EQE, bulk heterojunction OPVs suffer from low PCE because they tend to have low J_{SC}. Achievement of a better charge carrier transport without sacrificing EQE and V_{OC} could be the solution for higher PCE. Moreover, in a heterojucntion structure, the free carriers generated from exciton dissociation encounter their opposite carriers during transport, leading to charge recombination [6]. Considering all these, efficient charge carrier transport and optimization of conditions for their facilitation is of great importance for the future development of OPVs.

CNTs have been used to demonstrate that nano materials with a higher conductivity can be added to the OPV composite to act as a charge carrier transporters [36-38]. This has been accomplished by compositing CNTs with fullerenes. While the CNTs are highly

conductive, they themselves are not appropriate for efficient charge separation, and their high charge mobility has been found to enhance PCE. However, the gains in PCE have been modest due to the large size of the CNTs (micron scale length) and the fact that CNTs tend to be heterogeneous and show a wide range of band gap from 0.3 to 2.0 eV, work function between 4.5 to 5.1, but electron and hole mobilities of the order of 10^8 cm^2/Vs and 10^3 cm^2/Vs, respectively [2, 24, 33, 37, 58].

The relatively inexpensive large scale production of ND by a detonation synthesis process has made them commercially viable for a broad range of applications. NDs have tetrahedral network structures, large grain boundary density and low negative electron affinity which makes them attractive for electronic applications such as field emission [59]. The wide band gap (Eg ≈5.4–5.6 eV) makes ND a semiconductor material with a wide range of applications. The combination of high mechanical strength, stiffness, light weight, and low coefficient of friction make ND attractive for the fabrication of structural composites [60, 61] . NDs comprise a diamond core (sp^3), a middle core (sp^{2+x}) and a graphitic outer core (sp^2). The HOMO and LUMO energy of NDs are -5.5 and -3.0eV, respectively, are quite uniform [50] and NDs have modest charge mobility [62]. Based on these considerations, it is conceivable that NDs can serve as charge carriers in OPVs, and with typical size distribution of 2-10 nm, they may be appropriate for OPV fabrication [32]. The objective of this letter is to study the implementation of NDs in OPV structures especially as electron carrier in the acceptor phase. The other objective is to functionalize the NDs to a high degree to synthesize a composite suitable for OPV applications.

2.2 Experimental Section

2.2.1 Preparation and Characterization of Carboxylated NDs

Pristine ND (Purity 95%) and all other chemicals were purchased from Sigma Aldrich Inc. with purity higher than 95%. NDs were functionalized in a Microwave Accelerated Reaction System (Mode: CEM Mars) fitted with internal temperature and pressure controls. The as-received pristine NDs were treated with 1:1 70% nitric acid and 97% sulfuric acid in microwave reaction vessels. The microwave power was set to 95% of a total of 1600 watts and the temperature at 75°C. Reaction was carried out for 1 hr. This oxidizing procedure generated carboxylic group on the pristine NDs referred to as ND-COOH. The resulting solid was filtered through a 10 μm membrane filter, washed with water to a neutral pH and dried under vacuum at 80°C to a constant weight. The carboxylated NDs were characterized by scanning electron microscopy (SEM) and Fourier transformed infrared (FTIR). SEM Data was collected on a LEO 1530 VP Scanning Electron Microscope equipped with an energy-dispersive X-ray (EDX) analyzer. FTIR measurements were carried out in purified KBr pellets using a Perkin-Elmer (Spectrum One) instrument.

2.2.2 Preparation and Characterization of Fullerene-NDs Complexes

Fullerene powder with a purity of 99.98% was obtained from MER Corporation, and orthodichlorobenzene (ODCB) was obtained from Fisher Scientific. The C60-ND and C60-ND-COOH complexes were prepared as follows. First, C60 solution was prepared at a concentration of 10 mg/ml. ND-COOH powder was sonicated in ODCB for 10 min at a concentration of 0.1 mg/ml. Then, 0.05 ml of ND-COOH solution was mixed with 2ml of C60 solution by sonication for 10 min. The mixture was reacted by microwave irradiation

at 300W for 10 min. C60-ND-COOH complex and C60-ND complex were deposited on a cleaned Si wafer to take SEM images. FTIR spectra of C60 and C60-ND-COOH composite were collected in KBr pellets.

2.2.3 Fabrication and Characterization of OPV

The bulk heterojunction OPVs were formed as follows. Regioregular P3HT was obtained from Reike Metals Inc.. P3HT was added to the mixtures of the C60-ND complex and C60-ND-COOH at a 50 weight percent, and the mixtures were stirred overnight at room temperature. A similar solution of P3HT and C60 at 1:1 weight ratio was also prepared by dissolving directly in ODCB and stirring overnight. OPVs were fabricated onto ITO coated glasses. These were patterned prior to being cleaned with detergent, rinsed with de-ionized (DI) water and followed by acetone and isopropanol wash. They were dried with compressed nitrogen and put inside the oven for 5 min at 110°C. PEDOT:PSS aqueous dispersion was filtered and spin coated onto the cleaned glass substrates at 2600 rpm for 50 sec. Then the samples were dried inside the oven under one atmosphere at 110^{o}C for 30 min. The composite solution was spin coated on top of the PEDOT:PSS buffer layer at 400 rpm for 15 sec, and then for 5 sec at 730 rpm. Finally, a 75 nm thickness of Al cathode layer was deposited by thermal evaporation at 7×10^{-7} torr. The fabricated samples were annealed on hot plates at 120^{o}C for 10 min in a glove box filled with nitrogen. The active cell area was around 0.293 cm^2 and was defined by the intersection of Al and ITO layers. Morphology of the active layer was measured with tapping-mode atomic force microscopy (AFM) (Digital Instrument, NanoscopeII). UV-visible absorption spectroscopy of the active layer was measured by an HP 845 UV-visible absorption spectrophotometer.

A Keithley 2400 source-measuring unit was used to measure current-voltage characteristics in the dark and under irradiation. Simulated solar irradiation at 95 mW cm^{-2} was used for light source, which was obtained from a Newport 150W solar simulator with an AM 1.5G filter. A calibrated thermopile detector (Thorlabs Model S210A) was used to check the irradiation intensity before every measurement.

2.3 Results and Discussion

2.3.1 Conformation of Carboxylated Group on NDs

The photographs of pristine ND and carboxylated ND powder are shown in Figure 2.2 (a) and (b). The FTIR spectra and EDX of NDs are shown in Figure 2.1(A) and (B). Based on the EDX, the oxygen content in the oxidized ND increased to 17% compared to 10% in the original ND. The surface chemistries of NDs with and without strong acid treatments were characterized and compared by FTIR. Oxygen-containing surface groups such as hydroxyl, carboxylic, lactones, ketones and ethers are usually present on the ND particles surface and can be observed in Figure 2.1 A (a) and (b) shows the FTIR spectra of the original ND and Carboxylic functionalized NDs (ND-COOH). For the original NDs powder, the main features in the spectrum are related to CH (2924 cm^{-1} stretch and 1387cm^{-1} bend), OH and NH (1629cm^{-1}), COC (1128cm^{-1}) and OH vibrations (3424 cm^{-1} stretch and 1629 cm^{-1} bend), which have been assigned to surface functional groups such as aldehydes, esters, alcohols, acids and amines. For the oxidized NDs powder, it has almost the same IR adsorptions but as those of NDs except CH and COC peak which has shifted from 2924 cm^{-1} to 2909 cm^{-1} and 1128 cm^{-1} to 1120 cm^{-1}, respectively. The significant peak appearance at 1722 cm^{-1} indicates the presence of carboxylic group on the ND surface confirms the conversions of original functional groups like ketones, aldehydes, and

alcohols to carboxylic groups. SEM images in Figure 2.2 (c and d) of as received ND and oxidized NDs showed that there was no apparent change in morphology and shape after the surface functionalization.

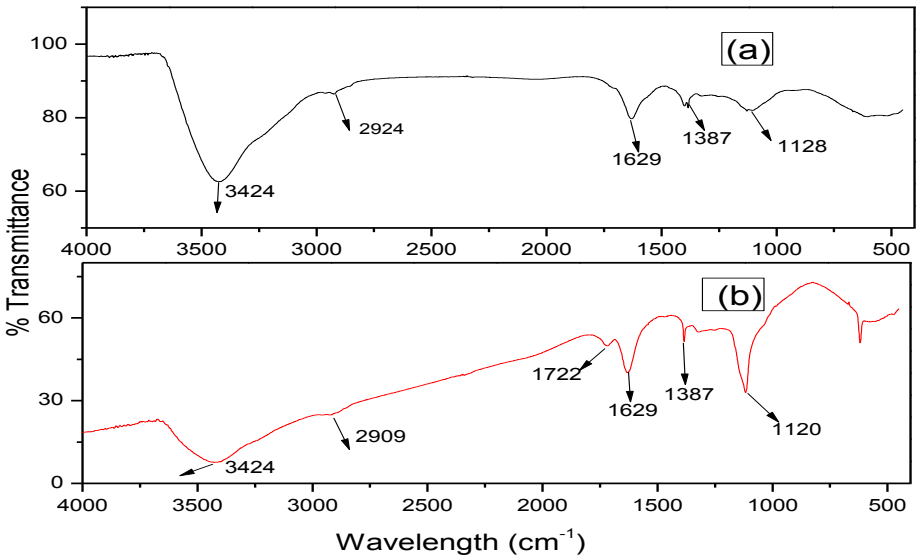

(A)

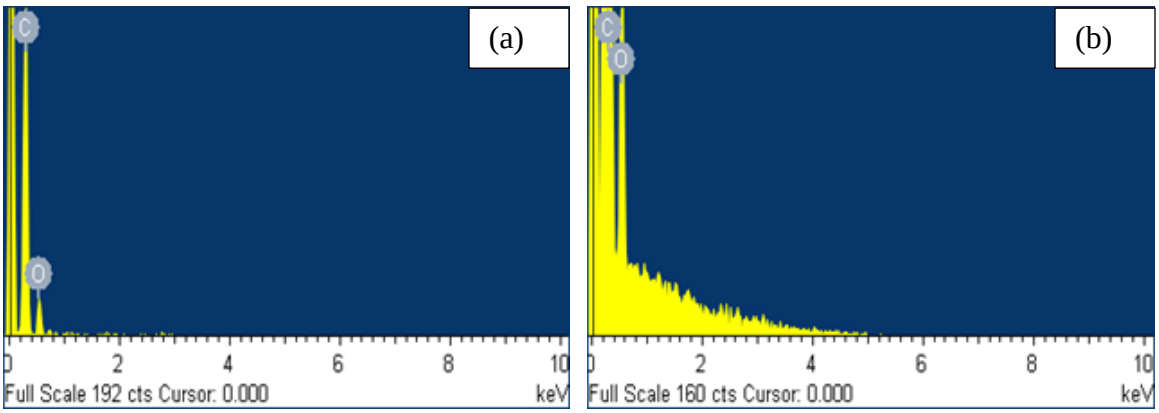

(B)

Figure 2.1 (A) IR-spectra of (a) As received ND and (b) Oxidized ND; (B) EDX of (a) As received ND and (b) Oxidized ND; (C) IR spectra of (a) pristine C60 (b) C60-ND-COOH composite; (D) UV-visible absorption spectra of (a) P3HT:C60 (b) P3HT:C60-ND (c) P3HT:C60-ND-COOH.

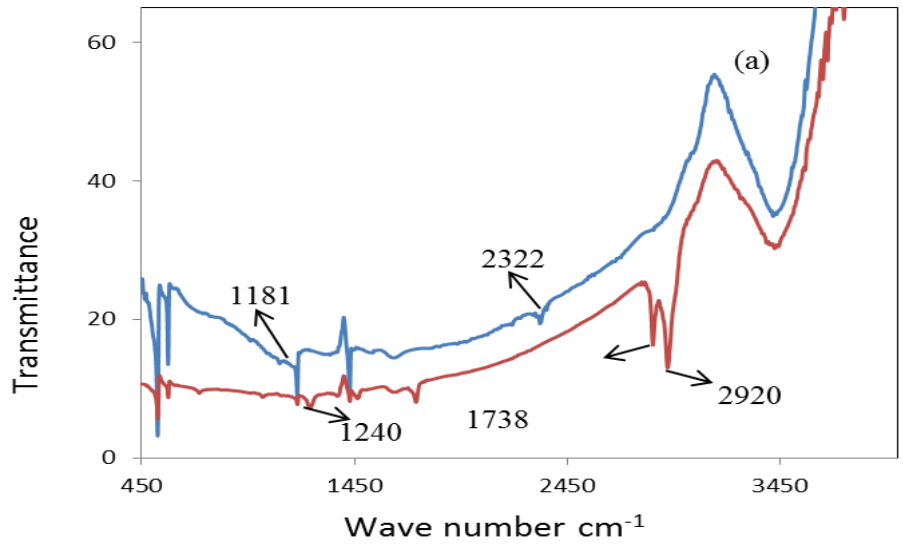

(C)

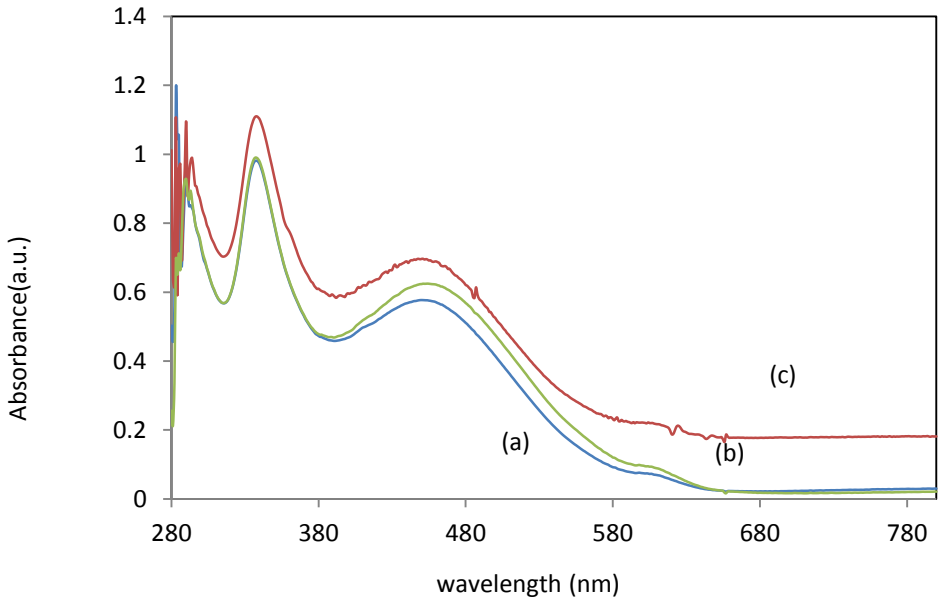

(D)

Figure 2.1 (A) IR-spectra of (a) As received ND and (b) Oxidized ND; (B) EDX of (a) As received ND and (b) Oxidized ND; (C) IR spectra of (a) pristine C60 (b) C60-ND-COOH composite; (D) UV-visible absorption spectra of (a) P3HT:C60 (b) P3HT:C60-ND (c) P3HT:C60-ND-COOH.

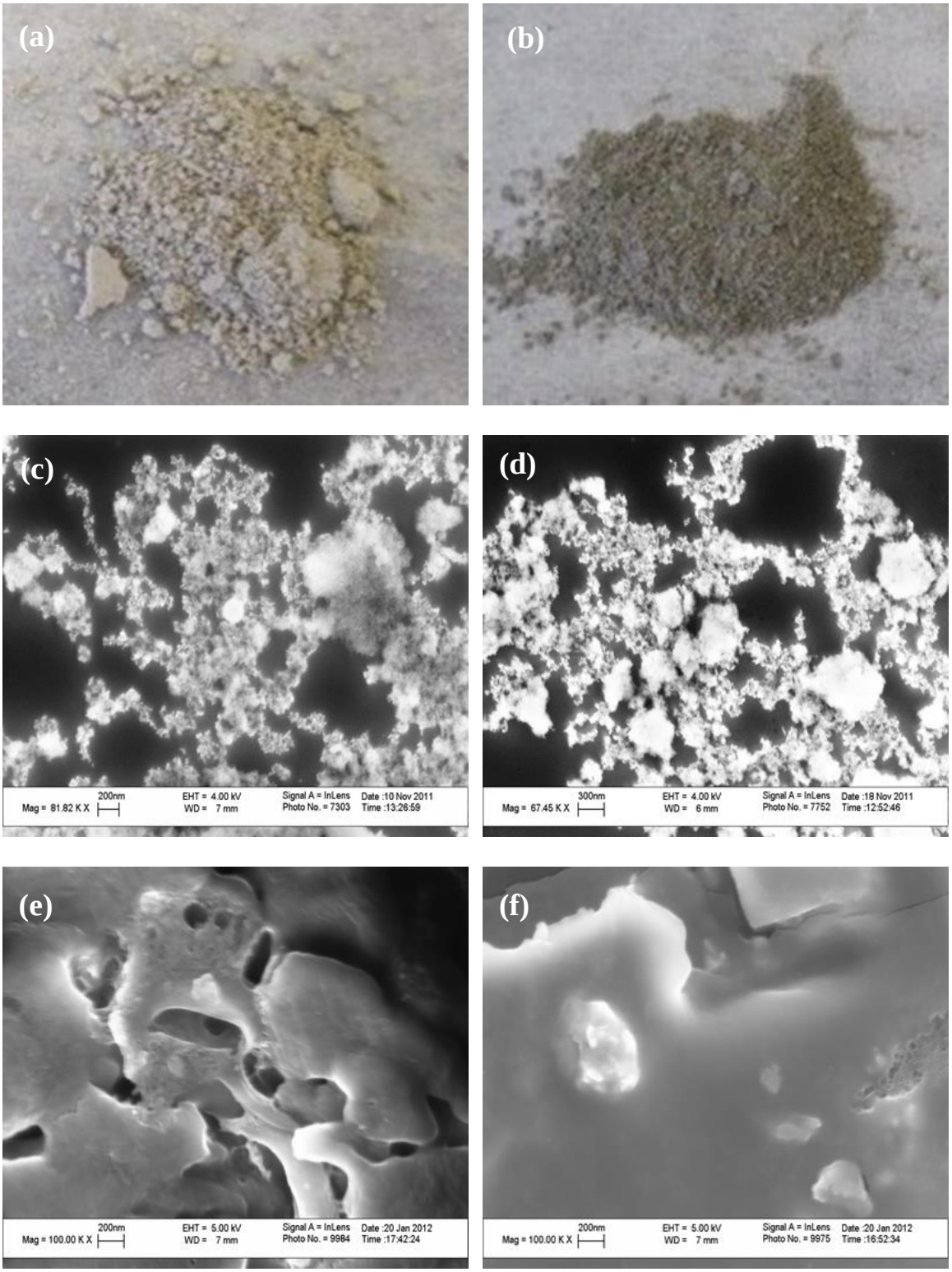

Figure 2.2 Photographs of (a) original ND (b) carboxylated ND; SEM images of (c) as received ND and (d) oxidized ND (e) C60 composite, (f) C60-ND composite and (g) C60-ND-COOH composite.

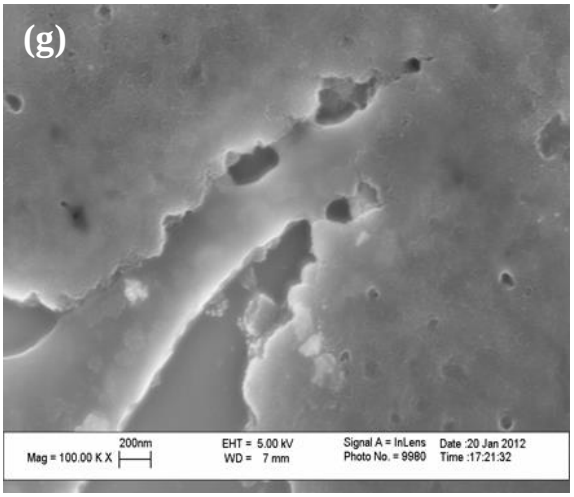

Figure 2.2 Photographs of (a) original ND (b) carboxylated ND; SEM images of (c) as received ND and (d) oxidized ND (e) C60 composite, (f) C60-ND composite and (g) C60-ND-COOH composite.

2.3.2 Conformation and Morphology of Fullerene-NDs Complexes

Carboxylated ND was chosen because it increased the solubility of ND in solvent, and reduced the aggregation which made a more uniform composite and provided an efficient percolation pathway for electron transport. It is anticipated that under microwave conditions, the NDs served as heated nuclei around which the C60 agglomerated. Fullerene molecules are known to polymerize at high temperature, pressure and under UV irradiation [37, 47]. After microwave induced reaction with C60, the surface of NDs was dotted with clusters of C60. It appears that C60 molecules (or clusters) reacted with NDs to form a weakly bonded or self-assembled C60-ND complex. Similar bonding has been reported before [36, 37]，and structures of C60-ND and C60-ND-COOH composites are shown in Figure 2.3 (a) and (b).

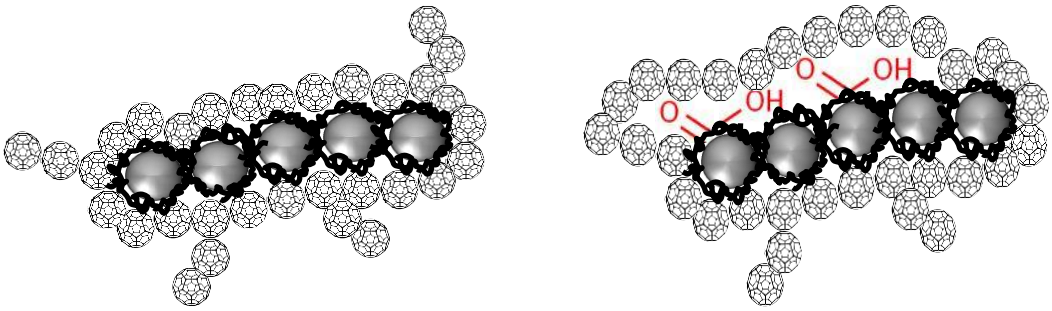

(a) (b)

Figure 2.3 (a) Structure of C60-ND composite (b) structure of C60-ND-COOH composite.

C60-ND-COOH complex was studied by using FTIR, UV absorption, SEM. SEM images of (e) C60, (f) C60-ND and (g) C60-ND-COOH composite prepared by microwave irradiation are shown in Figure 2.2. The films incorporating the NDs did not appear to be significantly different from those without them, which implies that the small size of NDs allowed them to be effectively integrated into the matrix. It is possible that the original 5 nm diameter NDs agglomerated to larger size, but that did not prevent them from being uniformly incorporated into the composite. This was different from previous observations with carbon nanotubes, where significantly different morphology was observed using SEM [36]. FTIR spectra of pristine C60 and C60-ND-COOH composite are shown in Figure 2.1(C). All of the four IR characteristic active modes for pristine C60 (525 cm^{-1}, 575 cm^{-1}, 1181 cm^{-1}, 1428 cm^{-1}) were seen in the C60-ND-COOH composite. In addition, the latter one showed absorption at 1738 cm^{-1}, 2851 cm^{-1} and 2920 cm^{-1}. The peak at 1738 cm^{-1} was attributed to C=O stretch in ND-COOH, and the two peaks of 2851 cm^{-1}, 2920 cm^{-1} were from the alkyl C-H stretch. Moreover, a peak at 1240 cm^{-1} appeared in the spectrum of C60-ND-COOH composite dues to the C-O stretch. These confirm the presence of

ND-COOH in the composite. The change in the relative intensity of the peak at 1181cm^{-1} and the disappearance of the peak at 2322 cm^{-1} showed that there was significant interaction between ND-COOH and C60. In addition, the UV-visible absorption spectra of P3HT:C60, P3HT:C60-ND-COOH and P3HT:C60-ND films are shown in Figure 2.1(D). P3HT:C60-ND-COOH film showed increased absorption in the 580-780 nm range without shifts in absorption peaks.

2.3.3 Morphology and Charge Transfer Mechanism

While, there was no visible alteration in the morphology based on SEM images (Figure 2.2 e,f,g), the AFM measurements of the photoactive composite showed that the presence of ND altered the film morphology, where the surface roughnesses were significantly different. The thickness of the active layer is around 100 nm, and the surface area of P3HT: C60 was 26.731 mm^2, P3HT: C60-ND was 26.075 mm^2, and P3HT:C60-ND-COOH was 26.678 mm^2. Since the difference in surface area was not significant, the difference in surface resistance was attributed to their composition. Figure 2.4 shows that the root mean square (RMS) of height image of P3HT:C60-ND-COOH film was 14.97 nm, P3HT:C60-ND was 2.98 nm, while P3HT:C60 films was 1.71 nm. The higher surface roughness led to large donor/acceptor interface for charge separation.

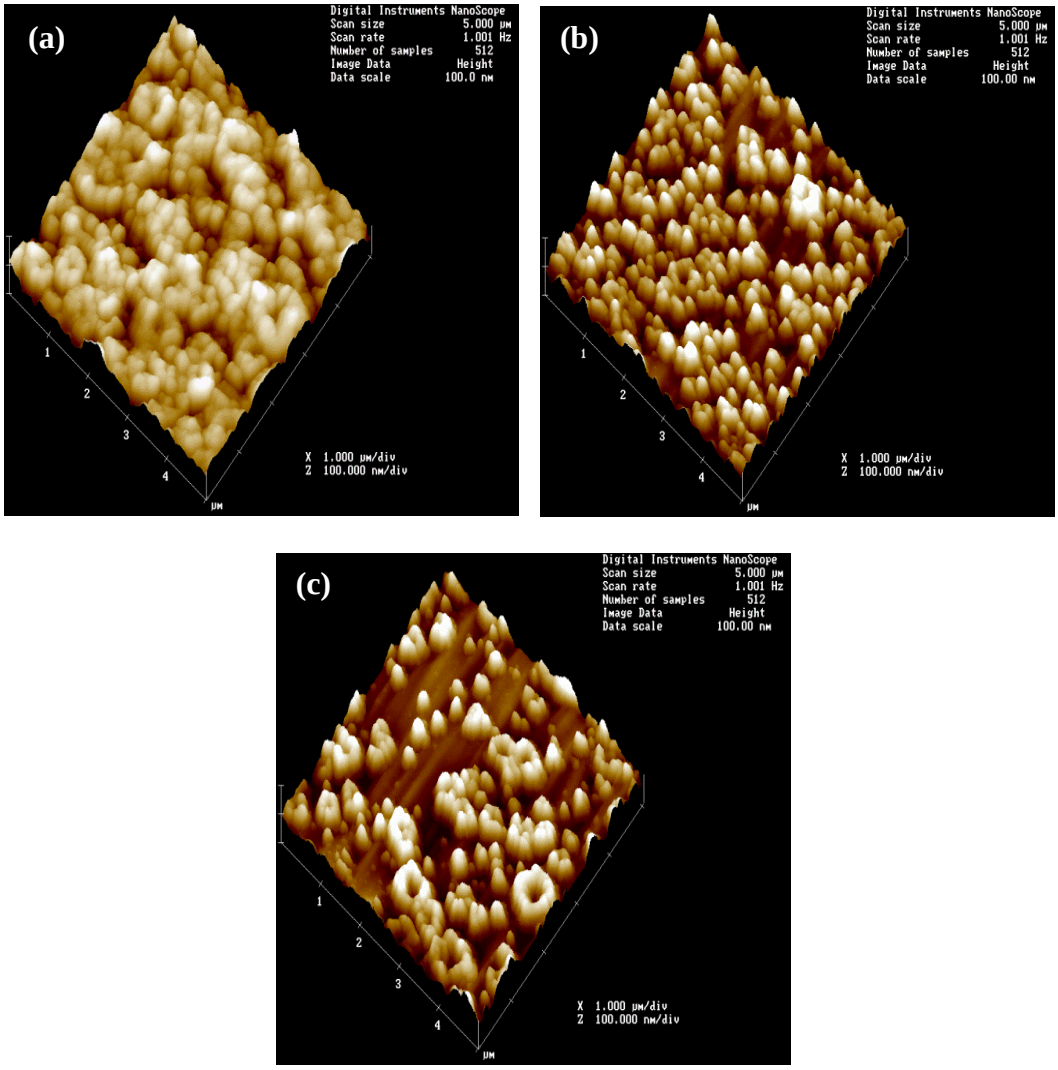

Figure 2.4 Tapping mode AFM of samples after annealing at 120°C for 10 min: (a) P3HT:C60 (b) P3HT:C60-ND (c) P3HT:C60-ND-COOH. Scan size was 5 µm×5 µm, the root mean square (RMS) surface roughness is about 1.71 nm, 3.0 nm, and 15.0 nm.

Since the NDs are expected to enhance charge transport, the resistance of the films was tested using Keithley 6517B electrometer. Surface resistance of P3HT:C60, P3HT:C60-ND and P3HT:C60-ND-COOH films were 35.3, 48.4 and 16.8 GΩ, respectively. This indicated that while the original ND somewhat increased resistance, the carboxylated NDs decreased it. This is attributed to the fact that the NDs did not form a

cohesive composite with the C60, whereas the ND-COOH did, which was expected to help in electron transfer.

Typical series resistance of P3HT PCBM is around the order of 20 Ωcm^{-2} [59], while a typical multi-crystalline silicon solar cell has a series resistances less than 1 Ωcm^{-2}. The series resistances of P3HT:C60, P3HT:C60-ND and P3HT:C60-ND-COOH was calculated as 71 Ωcm^{-2}, 72.9 $\Omega cm^{-2}$and 18.9 Ωcm^{-2}, respectively. At the same time, the shunt resistance of P3HT:C60 cell, P3HT:C60-ND and P3HT:C60-ND-COOH was calculated as 512 Ωcm-2, 884 Ωcm^{-2} and 269 Ωcm^{-2}, respectively. A combination of these may have prevented the increase in FF that would have been expected with the increase in introduction of ND into the photoactive matrix. Therefore, it is noted that the design can be further improved to realize the advantages of using ND and ND-COOH as charge transporters.

2.3.4 Photovoltaic Performance

The J-V curves for the different OPVs are presented in Figure 2.5 A and B, and their performance (mean and standard deviation) is presented in Table 2.1. The data represents an average of eight measurements. Based on Student t-test, the difference in PCE between C60, and C60 with ND-COOH were significant at 95% confidence level. It was observed that ND did not enhance the short circuit current as originally expected. However, when ND-COOH was introduced into the active layer via bonding with C60, Jsc increased from 2.25 to 3.44 $mAcm^{-2}$. The enhancement in Jsc was due to more efficient electron transport in the presence of ND-COOH. The electron mobility of C60 has been reported to be around 1 cm^2/Vs [3], while that for ND films is known to be an order of magnitude higher. Therefore, the introduction of NDs into active layer improved the electron mobility of

acceptor phase, and led to faster electron transport. In general, electrons captured by C60 molecules or clusters were transferred to ND-COOH, which was energetically favored. This was followed by faster electron transport than what could be achieved by hopping among C60 molecules. The lack of Jsc enhancement in the presence of ND was attributed to poor interfacial mixing and phase separation. Carboxylation improved dispersibility of NDs and led to better bonding with C60.

The high roughness factor in AFM measurements of the ND-COOH film implied better phase separation between the donor and the acceptor phases, which led to better charge separation. However, taller domains can lead to higher charge recombination. The ND was a good additive in the OPV, because its size was around 5 nm and even if its agglomerates represented larger size, they were still smaller than nanocarbons such as carbon nanotubes. The smaller size reduces the possibilities of charge recombination at the interfaces of donor and acceptor that is to be expected in larger additives.

From Table 2.1 it is seen that while current density increased significantly, FF decreased only slightly, and the Voc stayed almost the same. The resultant PCE increased from 0.34% to 0.51% for the ND-CCOH system, which was an enhancement of 50%. This indicates that the introduction of ND-COOH into the active layer increased charge transport.

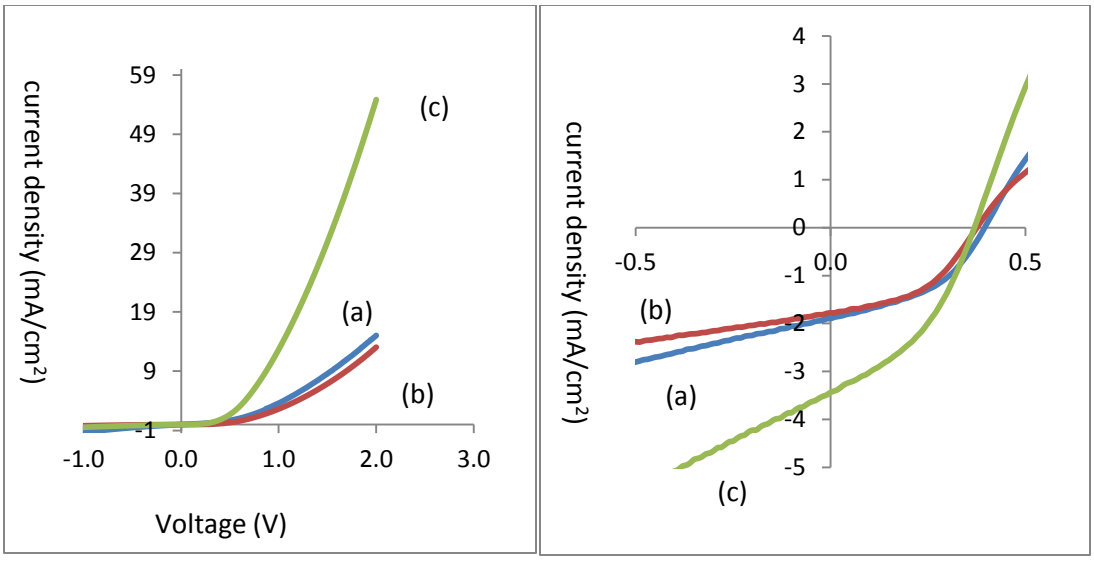

(A) (B)

Figure 2.5 (A) J-V characteristics in the dark of OPVs with (a)P3HT:C60, (b)P3HT:C60-ND, (c)P3HT:C60-ND-COOH, all of the cells were annealed at 120°C for 10min. (B) J-V characteristics under simulated solar irradiation at 95 mW cm-2 for OPVs with (a)P3HT:C60, (b)P3HT:C60-ND, (c)P3HT:C60-ND-COOH, all of the cells were annealed at 120°C for 10 min.

Table 2.1 Photovoltaic Parameters under 95mW/cm^2 Simulated Solar Irradiation Measured after Thermal Annealing at 120^{o}C.

Photoactive layer	**Voc (V)**	**Jsc (mA/cm^2)**	**Fill Factor (FF) (%)**	**PCE (%)**
(A) P3HT: C60	0.36±0.03	2.25±0.54	0.41±0.06	0.34±0.06
(B) P3HT: C60-ND	0.37±0.03	2.04±0.69	0.42±0.03	0.34±0.12
(C) P3HT: C60-ND-COOH	0.37±0.04	3.44±0.44	0.38±0.04	0.51±0.06

2.4 Summary

In conclusion, functionalized NDs are effective charge transporters in OPVs. Composites were made by microwave irradiation of a mixture of ND and carboxylated NDs in a solution with C60. The carboxylated ND was found to form a better composite and led to the increase in PCE by 50%. Introduction of ND-COOH enhanced short circuit current because of faster electron transport via network of NDs. No improvement in either Voc or FF was observed, but we expect further improvement in FF by device optimization. The results indicate that the ND-electron acceptor composite is an excellent candidate for low cost fabrication of polymer photovoltaic cells.

CHAPTER 3

A C70- CARBON NANOTUBE COMPLEX FOR BULK HETEROJUNCTION PHOTOVOLATIC CELLS

3.1 Introduction

OPV based on bulk heterojunction structure have shown improved performance with recent developments such as the use of low bandgap polymers, electron acceptors, processing additives, and tandem cell architecture. Fullerenes are the conventional electron-accepting materials[3, 10, 13, 33, 46, 49, 63]; and currently C60 and its derivatives are extensively used in OPVs. The deep LUMO energy level of C60 provides relatively high electron affinity and PCBM has found widespread applications due to its good dispersibility [64-66].

An alternate electron acceptor is C70 which is a higher molecular weight fullerene in the shape of a rugby ball. Its bandgap is around 1.9 eV, and the HOMO and LUMO are 6.1 eV and 4.2 eV, respectively. C70 has less structural symmetry, but higher absorption in the visible region than C60, which can lead to higher efficiency. Moreover, C70 has better dispersibility than C60 in solvents such as ODCB [23, 25, 64, 67, 68].

The importance of nanoscale morphology in bulk heterojunctions is widely recognized because it affects phase separation and improves percolation pathways. Therefore, optimizing film morphology can improve OPV performance. Nanocarbons including CNT and NDs have been utilized in OPV to improve electron transport. This has been accomplished by synthesizing CNT-C60 and functionalized nanodiamond-C60 complexes [36, 37, 49, 69]. The objective of this study was to see the effect of introducing CNTs into C70 phase as a component of the active layer in OPV.

3.2 Experimental Section

3.2.1 Preparation f-CNT and C70-f-CNT Composite

A C70-f-CNT composite was synthesized in Microwave Accelerated Reaction System (CEM Mars) fitted with internal temperature and pressure controls. Relatively short multi-walled carbon nanotubes (0.5-2 μm) were purchased from Cheap tubes Inc. They were carboxylated as follows using a previously published procedure [70]. In a typical reaction, 1 g of the CNTs were reacted with 40 ml of 1:1 concentrated H_2SO_4 and HNO_3 mixture under microwave radiation at 140°C for 10 min. After the reaction, the reactants were transferred into a beaker with DI water and cooled down to room temperature. The product was filtered under vacuum through a Teflon membrane with pore size of 0.45 μm. The resulting solid was thoroughly washed with DI water until a neutral pH was reached. The solids were stored in a vacuum oven (101kPa) at 70°C for 12 hr to yield carboxylated product (f-CNT).

3.2.2 Fabrication and Characterization of OPV

The photoactive polymer composite containing the C70 and f-CNT was prepared as follows: C70 Fullerene powder (98% purity) was purchased from MER Corporation; Regioregular P3HT was purchased from Reike Metal Inc., and ODCB was purchased from Fisher Scientific. First, 1 mg of f-CNT was added to 10 ml ODCB and sonicated for 10 min. A bulk solution of C70 in ODCB was prepared at a concentration of 10 mg/ml. Then 0.5 ml of the f-CNT solution was added to 5 ml prepared C70 solution and sonicated for 10 min. This was followed by microwave radiation at 300W for 10 min. Finally, P3HT was added to the processed solution to achieve a weight percentage of 50, and the composite was stirred overnight at room temperature. For comparison, a P3HT:C70

composite at a 1:1 weight ratio was also prepared by directly dissolving P3HT and C70 in ODCB. Also, 5 ml of 10 mg/ml C70 in ODCB was sonicated for 10 min and processed by microwave radiation at the same conditions.

SEM images were taken using an LEO 1530 CP field-emission SEM of films deposited on cleaned Si wafers from an ODCB solution of the C70-f-CNT complex. FTIR spectra were measured using a Perkin-Elmer FTIR spectrometer by taking a few drops of ODCB solutions of C70 or the C70-f-CNT complex on KBr powder, which were dried overnight in an oven at 100°C. The C70-f-CNT complex was studied using FTIR, Raman, SEM, UV absorption spectroscopy as well.

Photovoltaic cells were fabricated on 25 mm×25 mm ITO coated glass substrates (Delta-technologies, Rs=8-12). The glass substrates with patterned ITO were cleaned with detergent and rinsed with DI water. They were dried with compressed nitrogen. A 100 nm thick PEDOT:PSS layer was spin coated on the cleaned glass substrate from its aqueous dispersion (Baytron P, H.C. Stark Inc.), and dried at 110°C for 30 min in an oven under atmospheric conditions. Then the composite solution was spin coated on top of the PEDOT:PSS buffer layer at 420 rpm for 15 sec and then at 750 rpm for 5 sec to obtain a film with a thickness of 100 nm. A 100 nm thick Al cathode layer was deposited by thermal evaporation (NANO 36 Thin Film Deposition System) at 7×10^{-7} torr. The active cell area, defined by the intersection of the ITO and Al electrodes, was 0.25 cm^2. Morphology of the active layers was measured with tapping-mode AFM (Digital Instrument, Nanoscope II). The fabricated samples were annealed under a nitrogen atmosphere on a hot plate at 120°C for 10 min.

I-V characteristics in the dark were measured in a glove box under nitrogen atmosphere and I-V characteristics under irradiation were measured in the air. A Keithley 2400 source-measuring unit was used to generate the sweeping voltage and to record the current flowing through the device under test. A Newport 150W solar simulator with an AM 1.5G filter was used to provide simulated solar irradiation at 95 mW cm^{-2}. The irradiation intensity was checked with a calibrated thermopile detector (Thorlabs Model S210A) before each measurement.

3.3 Results and Discussion

3.3.1 Characterization of f-CNT, C70 and C70-f-CNT Composites

Figure 3.1 shows FTIR spectra of f-CNT, C70 and C70-f-CNT composite. The four characteristic peaks of f-CNT spectrum at 1217 cm^{-1}, 1594 cm^{-1}, 1720 cm^{-1}, 3365 cm^{-1} were due to carbonyl C-O stretching, C=C stretching, C=O stretching, and O-H stretching, respectively. This indicates the presence of carboxylic group on the surface of MWNT. The characteristic IR modes of C70 were dominant in both of C70-f-CNT composite, but there were two new absorption bands at 1636 and 3400 cm^{-1} in the spectra of the composite. The IR mode at 1636 cm^{-1} was assigned to the conjugated C=C bonded stretch which originated from the interaction between the carbon atoms on C70 and the carbon atoms on f-CNT. The broad band around 3400 cm^{-1} was assigned to the O-H group on the carboxylated MWNT. Moreover, both C-O bond and C=O bond disappeared, which may be attributed to the interaction between C70 and f-CNT.

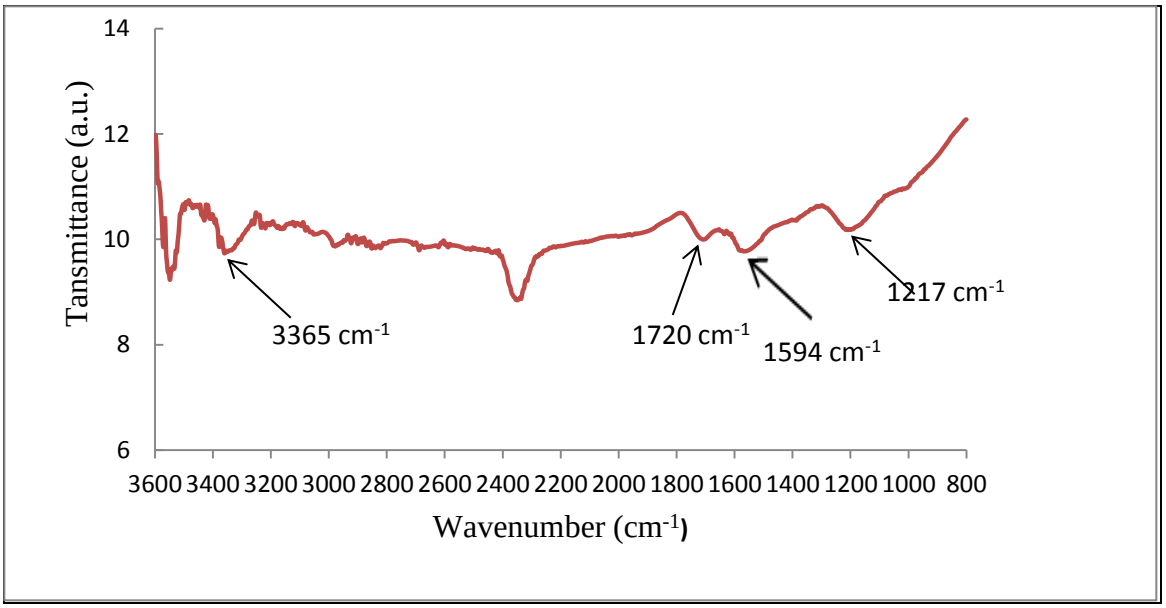

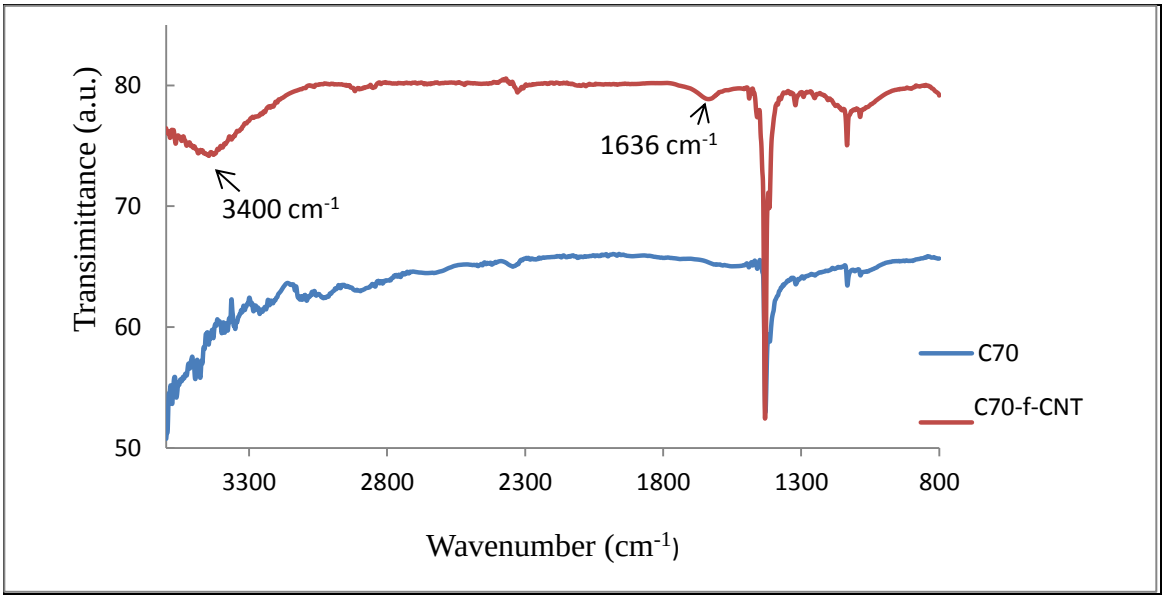

Figure 3.1 Shows the FTIR spectra of (a) f-CNT and (b) pristine C70 and C70-f-CNT composite.

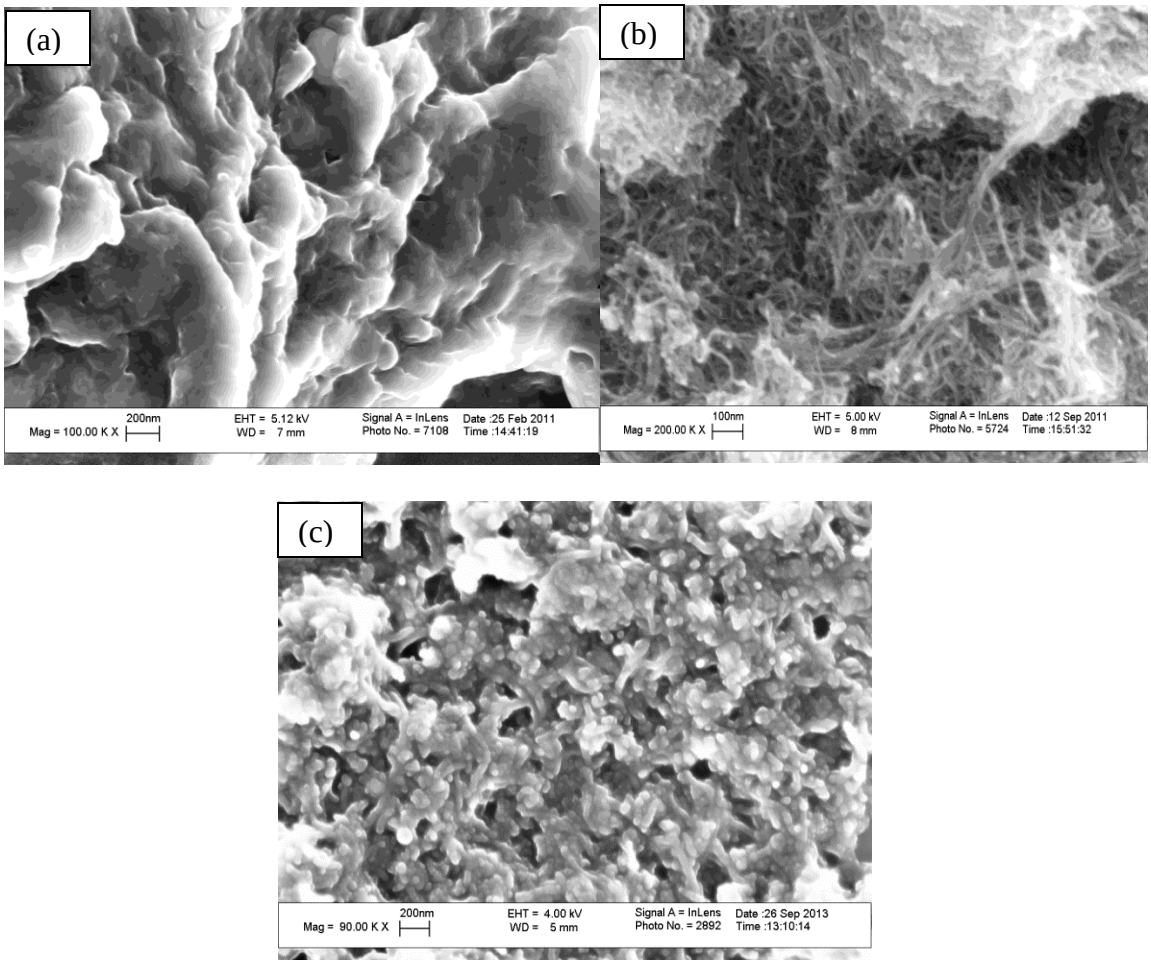

Figure 3.2 SEM images of (a) original C70 (b) f-CNT (c) C70-f-CNT complex prepared by microwave radiation.

SEM images of the original C70, f-CNT and the C70-f-CNT complex after microwave treatment are shown in Figure 3.2 (a), (b), and (c), respectively. After microwave induced reaction with C70, the surface showed a formation of a uniform composite phase similar to that observed previously for C60 [37]. Under microwave radiation, the CNTs served as heated nuclei where the C70 agglomerated. It appears that C70 formed weakly bonded or self-assembled C70-f-CNT complex. Similar bonding has been reported before for C60 [37].

3.3.2 Characterization of P3HT/C70-f-CNT Composite

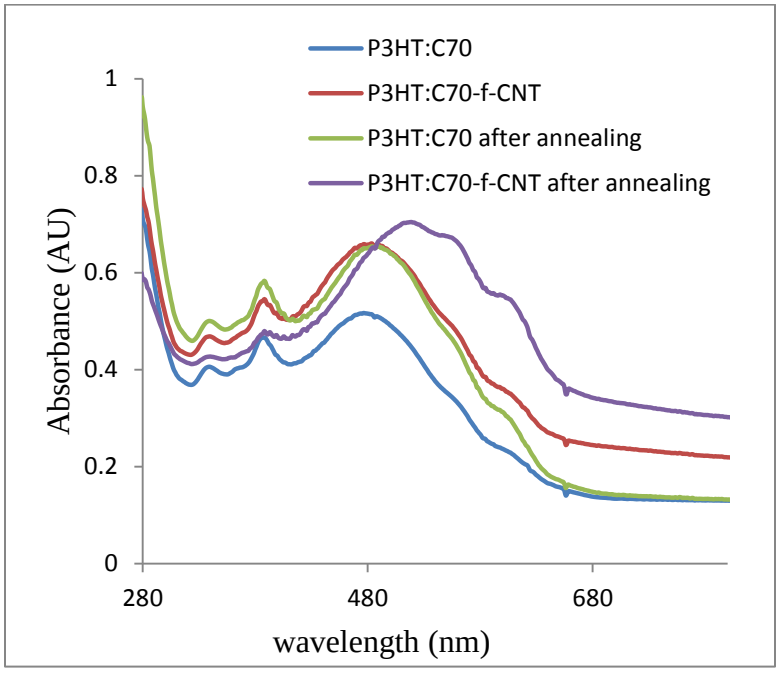

(a)

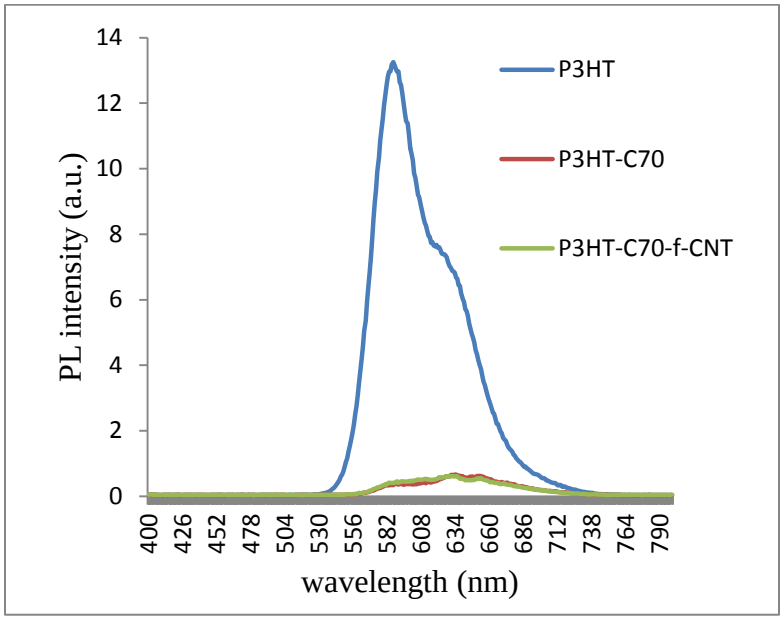

(b)

Figure 3.3 UV absorption spectra of (a) P3HT:C70 and P3HT:C70-f-CNT films before and after annealing at 120°C for 10 min. (b) Photoluminescence spectra of P3HT, P3HT:C70, P3HT: C70- f-CNT after annealing at 120°C for 10 min.

UV absorption spectra of P3HT:C70 and P3HT:C70-f-CNT films before and after annealing are shown in Figure 3.3 (a). It is well known that annealing helps improve the absorption, hence the integrated visible absorption of both cells of P3HT:C70 and P3HT: C70-f-CNT after annealing at 120°C for 10 min was calculated as 189.3 and 236.5. The latter showed a 25% of increased absorption, which helped increase the cell efficiency. Moreover, Photoluminescence (PL) spectra are shown in Figure 3.3(b). P3HT has strong PL in the visible region, which peaked at 587 nm. When C70 and C70-f-CNT were added to P3HT, the PL peak intensity reduced from 13.2 to 0.5. PL quenching provided direct evidence for exciton dissociation and in this case was unaffected by the presence of CNTs implying that the latter did not participate in exciton dissociation [69].

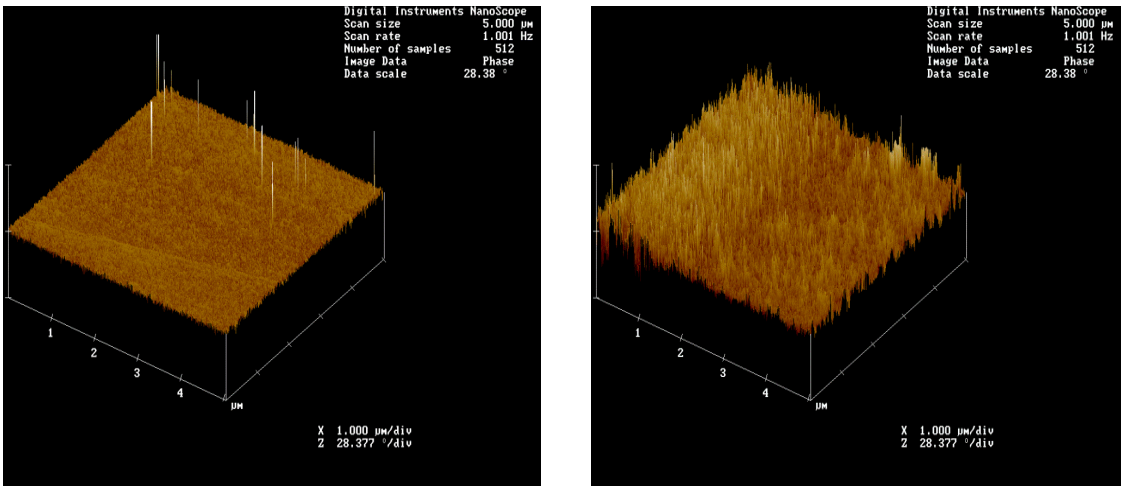

(a) (b)

Figure 3.4 AFM images of (a) original P3HT:C70 from ODCB solution, (b) P3HT:C70-f-CNT complex prepared by microwave irradiation, both of them are spin coated on glass and annealed.

As studied by AFM, the morphology of P3HT:C70-f-CNT film was different from P3HT:C70 film. This is seen from Figure 3.4(a) and (b). The thickness of the active layer was around 100 nm, and the surface areas of P3HT:C70 and P3HT:C70-f-CNT were both 0.25 cm^2. Since the thickness and the surface area of both of the active layers were the

same, the surface resistance was attributed to their compositions. The surface of P3HT:C70-f-CNT film was significantly rougher (Ra=3.243 nm) than P3HT:C70 film (Ra=0.833 nm). It is well known that the diffusion length of charge carriers is of the order of a few nanometers, and only those carriers generated near the electrodes contribute to the photocurrent. The surface roughness leads to an increase in contact area thus affecting the efficiency of charge collection at the electrode-polymer interface, it enhances internal reflection and light collection, and at the same time leads to larger donor and acceptor interfaces for better charge separation. [11].

3.3.3 Photovoltaic Performance

Figure 3.5 shows the I-V characteristics in the dark for cells with the C70-f-CNT complex and pristine C70. These cells were annealed at 120°C for 10 min after Al deposition. Both devices showed typical diode behavior in the dark. Values of shunt resistance R_{sh} of the PV cells were calculated using the slope of the dark J-V curve between -0.1 and + 0.1 V, and values of series resistance R_s were calculated based on the slope between 1.5 to 2.0 V. R_{sh} of P3HT:C70 cell and P3HT:C70-f-CNT were 1.4×10^{1} and 3.3×10^{3} Ωcm^2, respectively, and R_s of P3HT:C70 and P3HT:C70-f-CNT were calculated to be 21.7 and 14.0 Ωcm^2, respectively. Therefore, the introduction of f-CNT into the composite improved the electrical conductivity of the active layer and increased R_{sh}.

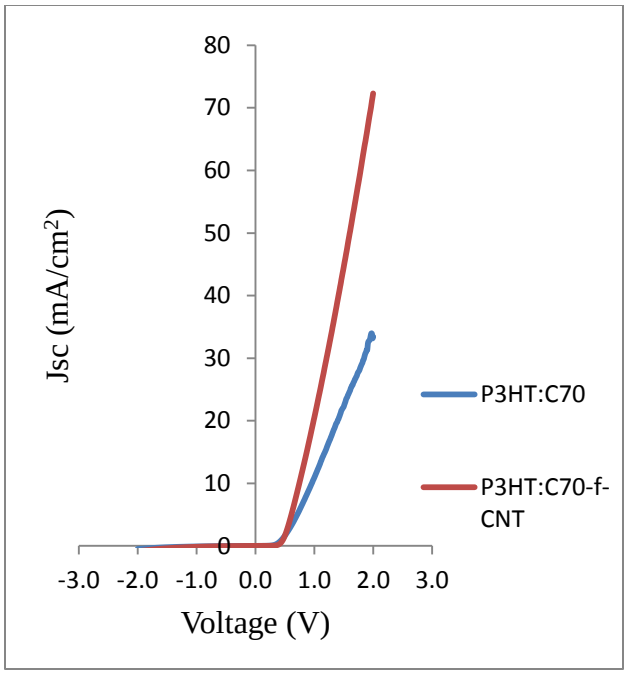

(a)

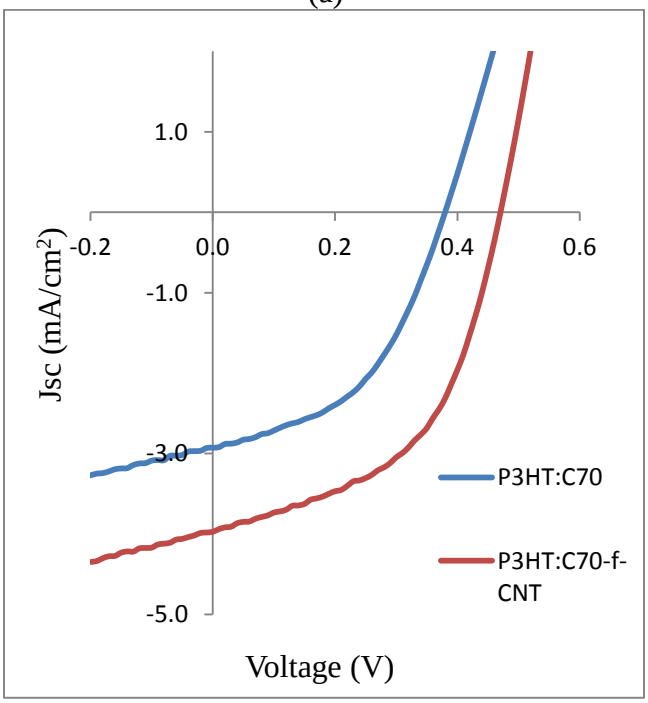

(b)

Figure 3.5 (a) I-V characteristics in the dark of photovoltaic cells with C70-f-CNT composite (red line) or P3HT:C70 composite (blue line) as active layer annealed at 120°C for 10 min. (b) I-V characteristics under simulated solar irradiation at 95 mW cm^{-2} phtovoltaic cells with P3HT:C70 or P3HT: C70-f-CNT as active layer annealed at 120°C for 10 min.

When the f-CNTs were introduced into the control system, the FF stayed almost the same, but the Voc increased 17.5% Jsc increased 31.8%, and PCE increased by 69.5%. This is presented in Table 3.1. The enhancement of Voc is attributed to the alternation of the bandgap of the C70-f-CNT composite because of the implementation of CNT into C70. The enhancement in Jsc was due to the more efficient electron transport because of the presence of CNTs. Electrons captured by C70 molecules or its clusters could be transferred to the CNTs, which is energetically favored. This was followed by faster electron transport than what could be achieved by hopping among C70 molecules. Moreover, the length of functionalized short CNT was only around 0.5 to 2 μm, which may reduce the possibilities of charge recombination at the interfaces of donor and acceptor, as a result, electron transportation becomes more efficient.

Previous data published on equivalent CNT-C60 composites showed the Voc, Jsc, FF, PCE of control cell P3HT:C60 to be 0.37 V, 2.47 mA/cm^2, 0.42%, and 0.41% , respectively, while those with CNT-C60 complex were 0.46 V, 3.74 mA/cm^2, 0.42%, 0.8% [37]. Compared to that the results on C70 from this study where efficiency increased by 43.9% by using lower symmetry acceptor C70 instead of C60 and an equivalent performance enhancement is observed with the introduction of CNTs.

Table 3.1 Photovoltaic Parameters of P3HT:C70-f-CNT and P3HT:C70 Devices under 95 mW cm^{-2} Simulated Solar Irradiation. The polymer: C70 Weight Ratio is the Same for All Devices (P3HT:C70=1:1). Samples were Annealed at 120°C for 10 min After Deposition of Al Cathode

Photovoltaic layer	**Concentration of CNT (mg/ml)**	**Voc (V)**	**Jsc (mA/cm^2)**	**FF (%)**	**PCE (%)**
P3HT: C70	0	0.40±0.02	3.02±0.44	0.47±0.01	0.59±0.12
P3HT: C70-f-CNT	0.01	0.47±0.01	3.98±0.2	0.51±0.02	1.0±0.03

3.4 Summary

In conclusion, polymer photovoltaic devices using a C70-f-CNT composite have been successfully fabricated. The inclusion of CNTs enhanced the performance of the cell and the average PCE of 1.0% under simulated solar irradiation (95 mW cm^{-2}) was achieved. The introduction of carboxylated CNTs into the composite not only enhanced Jsc, but also improved the FF and Voc.

CHAPTER 4

ENHANCED CHARGE CARRIER TRANSPORT THROUGH SHORTER CARBON NANOTUBES IN ORGANIC PHOTOVOLTAICS

4.1 Introduction

OPV are a promising low-cost alternative to silicon solar cells, particularly because they can be made via coating processes to cover large areas, and may be fabricated on flexible plastic substrates [71-74]. Devices incorporating conjugated polymers were enabled by the discovery of photoinduced charge transfer from polymers to Fullerene (C_{60}) and its derivatives such as PCBM. In spite of relatively high V_{OC}, bulk heterojunction OPVs suffer from low PCE because they tend to have low J_{SC}. Achievement of better charge carrier transport could be a path to higher PCE. Moreover, in a heterojunction structure the charge carriers encounter their opposite carriers during transport, leading to charge carrier recombination [6, 48]. Therefore, efficient charge carrier transport and optimization of conditions for their facilitation is of great importance for the future development of OPVs.

It is well known that OPV performance is strongly dependent on the nanoscale morphology of the active layer, the phase separation between donors and acceptors and the formation of interconnected percolation networks. It has been reported that carrier mobility can be improved by ameliorating the nanoscale morphology through introduction of nanomaterials [69, 75]. CNTs have been successfully added to the OPV composite to act as charge carriers/transporters [36, 76-79]. This has been accomplished by blending into OPV matrix [80] or compositing CNTs with fullerenes. While the CNTs have been also used as charge separators, their high electron and hole mobilities of the order of 10^8 $cm^{2/}Vs$ and 10^3 $cm^{2/}Vs$, respectively. It has been found to enhance PCE [36-38, 80]. However, the gains in PCE have been modest due to the relatively long lengths of the CNTs which can

cause a short circuit as well as be sites for charge recombination. The CNTs are expected to act as electron-transporting pathways as well as electron acceptors [77],[66, 81, 82] and the CNTs may also provide a larger surface area at the donor acceptor (D/A) interface for more efficient exciton dissociation [83-85].

Precise control of size and morphology of additives is needed before they can be implemented into an OPV structure. Typical CNTs are a heterogeneous mixture of different lengths. The long CNTs tend to be more tangled and provide a tortuous path for electron transport [86, 87]. Shorter CNTs could improve dispersibility as well as charge transport properties [86]. It's possible that this problem alleviated using shorter CNTs and one with less heterogeneity. The latter could lead to a more defined architecture. The shorter CNTs may also provide a larger surface area at the donor and acceptor interface, which would be favorable for efficient dissociation of excitons. Recent developments in size sorting by high-speed centrifugation, field-flow fractionation, gel electrophoresis, capillary electrophoresis and size-exclusion chromatography and high performance liquid chromatography make it a viable possibility [87]. The objective of this research was to study the implementation of MWNTs of different lengths in conventional P3HT: PCBM solar cell for enhanced charge transport.

4.2 Experimental Section

4.2.1 Preparation and Size Segregation of MWNTs

The synthesis of the carboxylated multi-walled carbon nanotubes were carried out under the Microwave Accelerated Reaction System. Pre-weighted MWNTs (from Cheap tubes Inc. with the length of 500-2000 nm and diameter of 30-50 nm) were added to reaction chamber together with a mixture of concentrated H_2SO_4 and HNO_3. The reaction vessels

were subject to microwave radiation at a preset temperature of 140°C for 20 min. After cooling to room temperature, the product was vacuum filtered using DI water with pore size 10 μm, until the filtration reached a neutral pH. The carboxylated MWNTs were dried in a vacuum oven at 70°C until constant weight.

The long and the short MWNTs were prepared from the same sample, thus eliminating the possibility of batch to batch variation was achieved. The original mixture was size sorted as follows. The highly dispersible original (MWNT-O) was sonicated at low power to disperse in water and centrifuged at 10,000 rpm. The sediment was redispersed in water by sonication and centrifuged once again. The sediment represented the fraction with the longest CNTs and was used for fabricating CNTs. The solution phase from the first sonication at 10,000 rpm was sequentially sonicated at 12,000, 14,000 and 16,000 rpm with the sediment being rejected at each step. The final suspension represented the fraction with the shortest length and was used to fabricate OPVs. The mean length of the long (MWNT-L) and short (MWNT-S) nanotube fractions were 1695±204 nm and 123±12 nm, respectively. Morphology of the MWNTs was studied by SEM.

4.2.2 Solar Cell Fabrication and Characterization

The bulk heterojunction OPVs were fabricated as follows. PCBM powder with a purity of 99.98% was obtained from MER Corporation, and ODCB was obtained from Fisher Scientific. Regioregular P3HT was obtained from Reike Metals Inc. Bulk PCBM solution in ODCB was prepared at a concentration of 10 mg/ml, 0.3 ml of the MWNT-O solution at a concentration of 0.1 mg/ml was added into 3 ml of PCBM solution and sonicated for 10 min. MWNT-L and MWNT-S solutions with PCBM solution were prepared in the same method. The suspension was then mixed with fifty weight percent of P3HT and stirred

overnight at room temperature. A similar 1:1 solution of P3HT and PCBM was also prepared by dissolving directly the two components in ODCB and stirring overnight. OPVs were fabricated onto ITO coated glass. These were patterned prior to being cleaned with detergent, rinsed with DI water and washed with acetone and isopropanol. They were dried with compressed nitrogen and put inside the oven for 5 min at 110°C.

Aqueous dispersion of PEDOT: PSS (conductive grade) was filtered and spin coated onto the cleaned glass substrates at 2800 rpm for 50 sec. Then the samples were dried inside the oven under one atmosphere at 110°C for 30 min. The composite solution was spin coated on top of the PEDOT:PSS buffer layer to produce a film with a thickness of around 100 nm. Then the sample was allowed to dry slowly in the sealed petri dish at room temperature. Finally, a 145 nm thickness of Al cathode layer was deposited by thermal evaporation using a shadow mask at 7×10^{-7} torr. The fabricated samples were annealed on hot plates at 125^{o}C for 10 min in a Nitrogen glove box. The active cell area was around 0.272 cm^2 and was defined by the intersection of Al and ITO layers. Morphology of the active layer was characterized with tapping-mode AFM (Digital Instrument, NanoscopeII) and SEM. UV-visible absorption spectroscopy of the active layer was measured by an HP 845 UV-visible absorption spectrophotometer and photoluminescence spectra was studied by an F-7000 Fluorescence Spectrophotometer.

A Keithley 2400 source-measuring unit was used to measure current-voltage characteristics in the dark and under simulated solar irradiation. Newport 122W solar simulator with an AM 1.5G filter simulated radiation at 95 mW cm^{-2}. A calibrated thermopile detector (Thorlabs Model S210A) was used to check the irradiation intensity before every measurement.

4.3 Results and Discussion

4.3.1 Morphology of Different Sizes of MWNTs and Active Layers

SEM measurements were carried out to analyze size distributions of MWNT-L and MWNT-S, shown in Figure 4.1 (a) and (b), and Table 1 [88]. The mean length of MWNT-L was found to be 1695±204 nm and the mean length of MWNT-S was 123±12 nm. This clearly showed that there was a significant difference between two fractions.

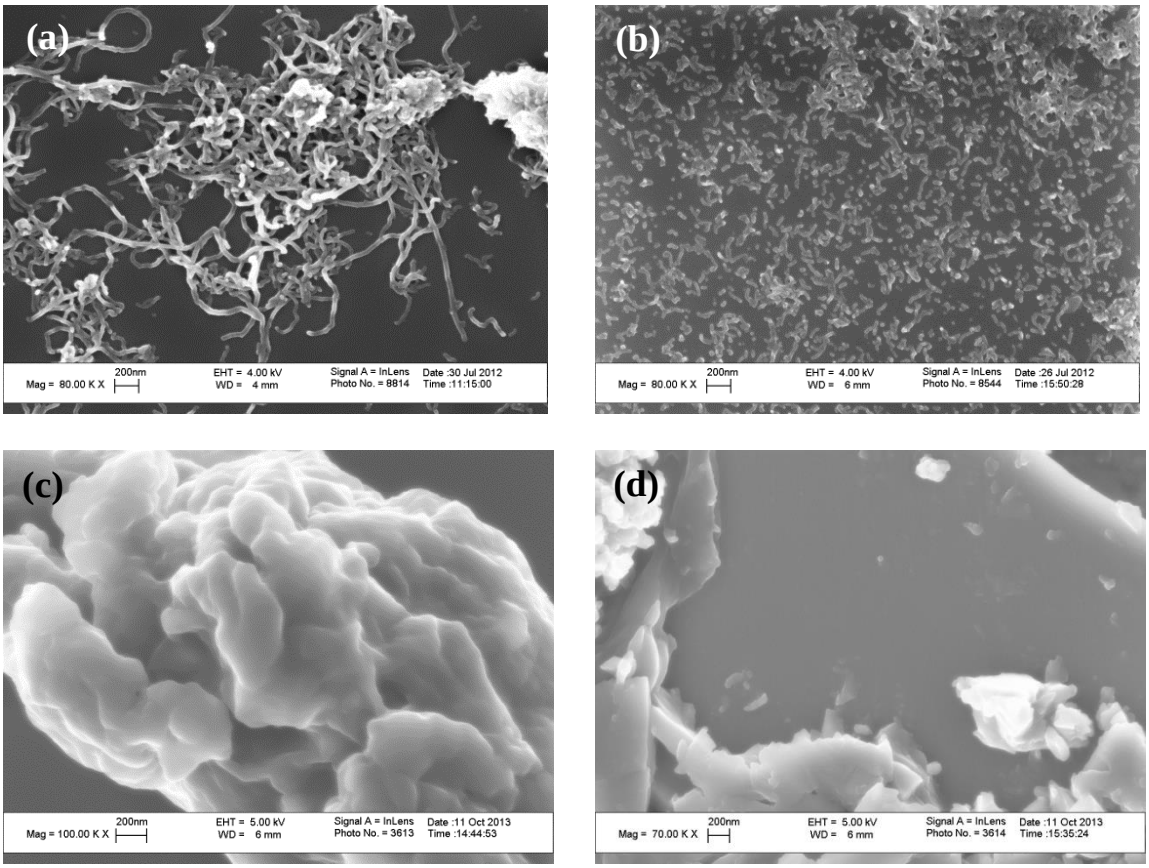

Figure 4.1 SEM images of (a) MWNT-L (b) MWNT-S (c) P3HT: PCBM, (d) P3HT: PCBM –MWNT-O (continued).

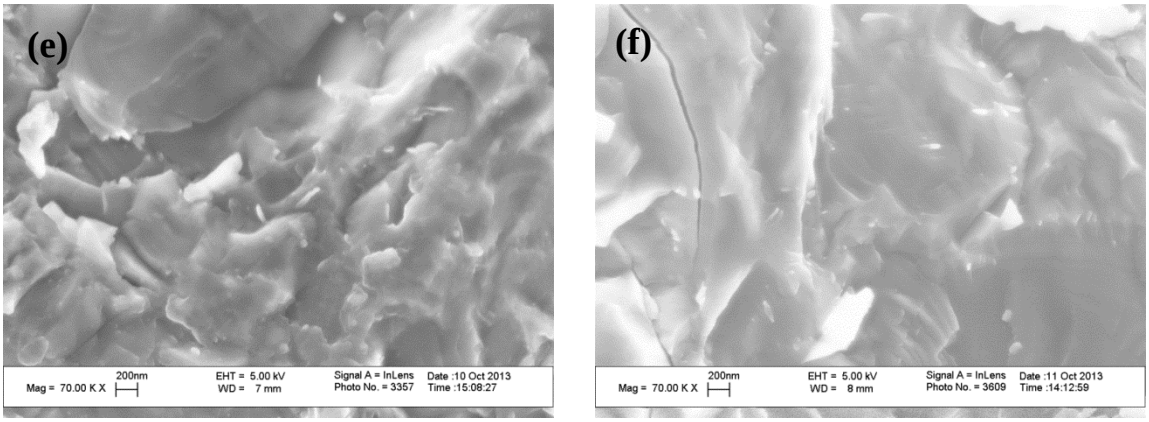

Figure 4.1 SEM images of (e) P3HT: PCBM- MWNT-L, (f) P3HT: PCBM-MWNT-S (continued).

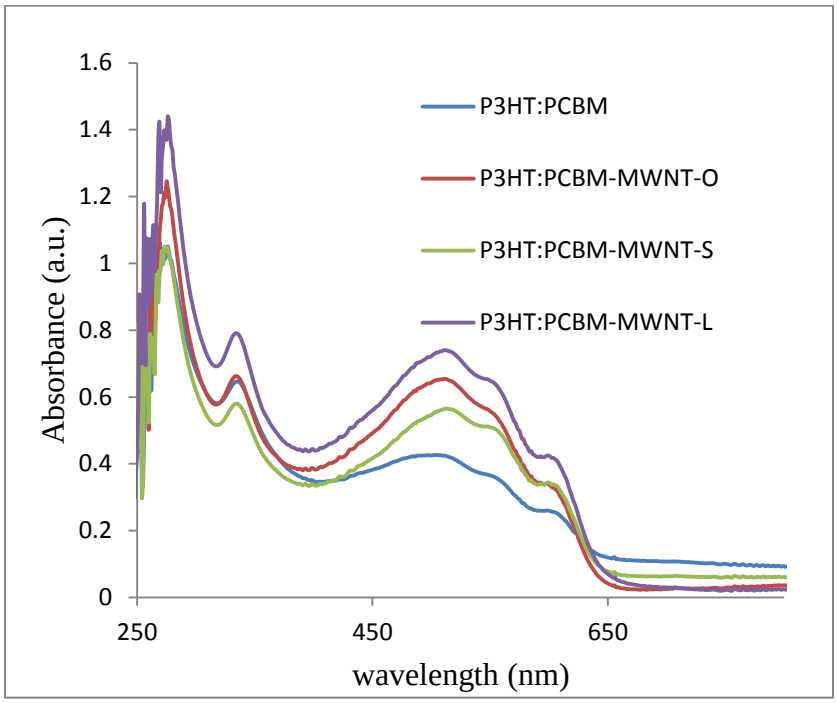

(a)

Figure 4.2 UV absorption spectra (a) and PL spectra (b) of P3HT: PCBM, P3HT: PCBM –MWNT-O, P3HT: PCBM- MWNT-L, and P3HT: PCBM-MWNT-S.

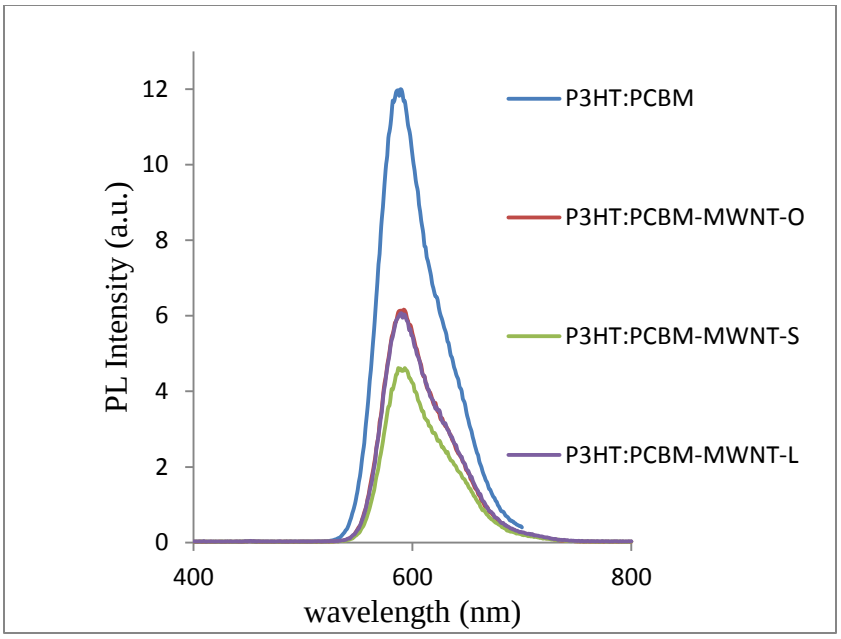

(b)

Figure 4.2 UV absorption spectra (a) and PL spectra (b) of P3HT: PCBM, P3HT: PCBM –MWNT-O, P3HT: PCBM- MWNT-L, and P3HT: PCBM-MWNT-S.

The UV spectra of P3HT: PCBM, P3HT: PCBM –MWNT-O, P3HT: PCBM-MWNT-L, and P3HT: PCBM-MWNT-S coated films are shown in Figure 4.2(a). The introduction of different lengths of MWNT into P3HT:PCBM blend increased the absorption, and MWNT-L enhanced the absorption the most. This is in line with previously published report by Cheng X et. al. [88]. The PL spectra of P3HT: PCBM, P3HT: PCBM –MWNT-O, P3HT: PCBM-MWNT-L, and P3HT: PCBM-MWNT-S in ODCB are shown in Figure 4.2(b). The strong PL peak at 587 nm is the signature for P3HT in ODCB. The observed PL for P3HT:PCBM blends indicates that some of the excitons generated in P3HT recombined. The addition of MWNT-O and MWNT-L to P3HT: PCBM blend reduced the PL intensity almost equally, however, implementation of MWNT-S quenched the intensity the most, from 11.4 to 4.8, which could imply that the implementation of

MWNT-S contributes to the more efficient charge separation and resulted in the enhanced photocurrent density [72].

The morphology of active layers of P3HT:PCBM with MWNT-O, MWNT-L and MWNT-S was studied by SEM. It was seen that the implemetation of MWNTs altered the morphology of the films, and the nanotubes could be seen sticking out of the film surfaces. AFM images of photovoltaic layer of P3HT:PCBM with MWNT-O,MWNT-L and MWNT-S after annealing are shown in Figure 4.3. The morpholgy of the active layers was altered in the presence of different MWNTs. The surface roughness of P3HT:PCBM, P3HT:PCBM with MWNT-O, MWNT-L and MWNT-S was 6.4, 9.2, 8.1, and 11.0 nm resepctively. The introduction of MWNT-S increased the surface roughness of the active layer and also altered the texture into a much coarser film with broad hill-like features compared to the other films. As presented below, the devices with higher surface roughness showed superrior device performance.

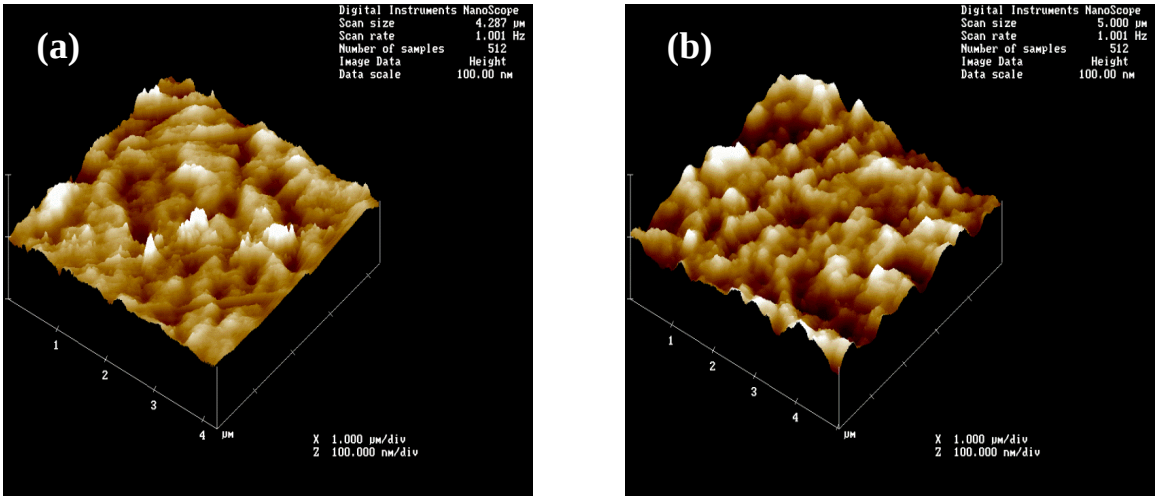

Figure 4.3 AFM images of active layers of (a) P3HT: PCBM, (b) P3HT: PCBM – MWNT-O, (c) P3HT: PCBM- MWNT-L, (d) P3HT: PCBM-MWNT-S.

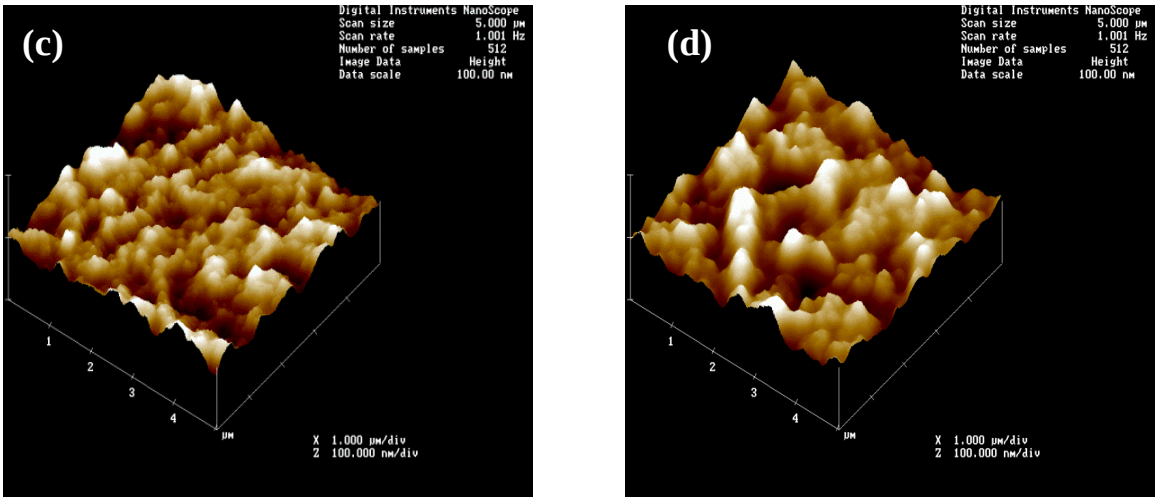

Figure 4.3 AFM images of active layers of (a) P3HT: PCBM, (b) P3HT: PCBM – MWNT-O, (c) P3HT: PCBM- MWNT-L, (d) P3HT: PCBM-MWNT-S.

4.3.2 Performance of Solar Cell Devices

J-V curves of different devices are shown in Figure 4.4 A and B and their performances (mean and standard deviation) are presented in Table 1. The data represents an average of eight measurements. Based on Student t-test, the difference in PCE among the different OPVs was significant at 95% confidence level. It is seen from Table 4.1 that while Voc and FF stayed the almost the same, short circuit current increase from 4.77±0.17 to 5.2±0.11, 5.35±0.36 and 6.39±0.5 $mAcm^{-2}$ for P3HT:PCBM to that with MWNT-O, MWNT-L and MWNT-S, respectively. The integration of MWNTs to P3HT: PCBM led to higher Jsc, which eventually led to more efficient electron transport. Therefore, PCE increased from 1.20±0.06 for P3HT:PCBM to 1.35±0.04, 1.33±0.09 and 1.56±0.12 % for OPVs with MWNT-O, MWNT-L and MWNT-S, respectively. The introduction of all three different lengths of MWNTs increased the efficiency of the devices and MWNT-S was the most effective one.

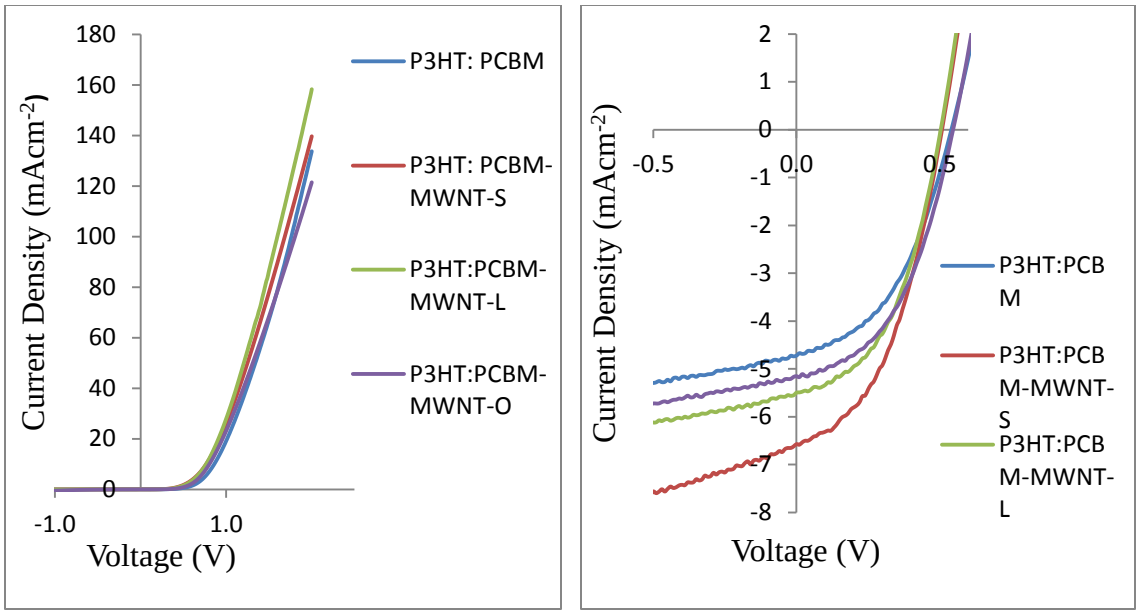

(A) (B)

Figure 4.4 (A) J-V characteristics in the dark of OPVs with (a)P3HT:PCBM, (b)P3HT: PCBM –MWNT-O, (c)P3HT:PCBM-MWNT-L, (d)P3HT: PCBM-MWNT-S. All of the cells were annealed at 125°C for 10 min. (B) J-V characteristics under simulated solar irradiation at 95 mW cm^{-2} for OPVs with (a)P3HT:PCBM, (b) P3HT: PCBM – MWNT-O, (c)P3HT:PCBM- MWNT-L, (d)P3HT: PCBM- MWNT-S. All of the cells were annealed at 125°C for 10 min.

The introduction of MWNTs provided better percolation pathways for faster charge transport. The MWNT-S appeared to serve as better charge transport carriers than MWNT-L. With thickness of the active layer around 100 nm, the MWNT-S with mean length of 123 nm provided better and faster percolation for charge transport. On the other hand, the 1695 nm mean length of MWNT-O could increase the possibilities of short circuit and charge recombinition.

Table 4.1 Photovoltaic Parameters under 95 mW/cm^2 Simulated Solar Irradiation Measured after Yhermal Annealing at 125^{o}C

Photoactive layer	Length (nm)	Voc (V)	Current Density (mAcm^{-2})	Fill Factor (FF) (%)	PCE (%)
P3HT: PCBM		0.54±0.01	4.77±0.17	0.44±0.02	1.20±0.06
P3HT: PCBM with MWNT-O	500-2000	0.54±0.01	5.2±0.11	0.46±0.01	1.35±0.04
P3HT: PCBM with MWNT-L	1695±204	0.51±0.03	5.35±0.36	0.45±0.01	1.33±0.09
P3HT: PCBM with MWNT-S	123±12	0.53±0.03	6.39±0.5	0.44±0.04	1.56±0.12

4.4 Summary

In conclusion, short MWNTs are more effective charge carrier transporters in OPVs, and this led to the enhancement in PCE by 30%. The introduction of MWNT enhanced short circuit current. The enhancement in Jsc for the original, long and short MWNTs were 9%, 12% and 34%, respectively. No improvement in either Voc or FF was observed. It is prudent to expect further improvement in FF by device optimization. These results indicate that the length of the CNT as a charge carrier is an important parameter to be considered in their implementation in OPV and possibly in other photonic devices.

CHAPTER 5

EFFECT OF LOW CONCENTRATIONS OF CARBON BLACK IN ORGANIC SOLAR CELLS

5.1 Introduction

The OPVs are excellent alternatives to conventional silicon and thin film solar cells because they attempt to achieve moderate PCE at significantly lower cost. Typical OPVs are based on the creation of bulk heterojunction solar cells consisting of blends of an electron-donating semiconducting polymer and an electron-accepting molecule such as fullerene (C_{60}) or its derivative [3, 16, 33, 47, 52-56, 89, 90]. While C60 typically has shown low PCE, its derivatives such as PCBM with P3HT bulk heterojunctions have shown PCE that are approaching 5% [48] and the efficiencies of OPVs with low band gap donors are approaching 10% [43].

Improvement in OPVs can be brought about by addressing some of its limitations, namely, improving absorption of a wide range of the solar radiation spectrum [10, 57], and enhancing the electron and hole mobilities [36]. The phase separation in bulk heterojunction solar cells creates percolation pathways for transporting the holes and electrons to their respective electrodes. Therefore, the performance of heterojunction solar cells can also be improved by optimizing phase separation.

Nanocarbons, including CB, graphite, CNTs and NDs are important for many applications for enhancing electrical properties. They have been used in OPVs, where the introduction of CNTs and NDs has been reported to enhance phase separation as well as increase electron mobility [49],[36],[38, 69]. The structure of commercial CB is known to have both crystalline carbon (graphite) and amorphous carbon, where the aggregates tend

to form through Van der Waals forces. CB is electrically conductive with conductivities ranging from 0.1 to 10^2 S/cm at ambient temperature. They impart good conductivity to polymers and have been widely used as fillers in polymers for applications such as conductive packaging for electronics, and as fuel cell electrodes [44]. CB also shows high absorption of the solar spectra [45]. The objective of this research was to study the effect of CB as an additive to enhance charge transport and also to see if film morphology can be improved. The P3HT/C60 system was selected as a model with a particular interest in the effect of concentration of CB.

5.2 Experimental Section

5.2.1 Preparation of Different Concentrations of C60-CB Composites

Regioregular P3HT was obtained from Reike Metals Inc., CB was obtained from Sigma-Aldrich Co., and fullerene powder with a purity of 99.98% was obtained from MER Co. The different concentrations in the parts per million (ppm) of C60-CB composites were prepared according to an experimental procedure previously published by our laboratory [37, 69]. First, C60 solution was prepared at a concentration of 10 mg/ml. CB powder was sonicated in ODCB (shown in Figure 1 a) for 20 min at seven different concentrations. Then 0.3 ml of different concentrations of CB solutions was mixed separately with 3 ml of C60 solution by sonication for 10 min. Mixtures were reacted by microwave irradiation (CEM Discover system) at 300W for 10 min.

5.2.2 Fabrication of OPV Using P3HT/C60-CB Composites

The bulk heterojunction OPV were formed as follows. P3HT was added to the mixtures of the C60-CB composite at different concentrations at a 50 weight percent, and the mixtures

were stirred overnight at room temperature. A similar solution of P3HT and C60 at 1:1 concentration was also prepared by dissolving directly in ODCB and stirring overnight. OPV were fabricated onto ITO coated glasses. These were patterned prior to being cleaned with detergent, rinsed with DI water and followed by acetone and isopropanol wash. They were dried with compressed nitrogen and put inside the oven for 5 min at 110°C. PEDOT:PSS aqueous dispersion was filtered and spin coated onto the cleaned glass substrates at 2600 rpm for 50 sec. Then the samples were dried inside the oven under one atmosphere at 110°C for 30 min. The composite solutions were spin coated on top of the PEDOT:PSS buffer layer at 400 rpm for 15 sec, and then for 5 sec at 730 rpm. Finally, a 100 nm thickness of Al cathode layer was deposited by thermal evaporation at 7×10^{-7} torr. The fabricated samples were annealed on hot plates at 120^{o}C for 10 min in a glove box filled with nitrogen. The active cell area was around 0.272 cm^2 and was defined by the intersection of Al and ITO layers. The concentrations of CB in photoactive films were 5000, 2500, 500, 150, 85, 25, and 12.5 ppm, and they were referred as P3HT-C60-CB-5000, P3HT-C60-CB-2500, P3HT-C60-CB-500, P3HT-C60-CB-150, P3HT-C60-CB-85, P3HT-C60-CB-25, P3HT-C60-CB-12.5, respectively (Table 5.1).

5.2.3 Characterizations of CB, P3HT/C60-CB Composites, and OPV Using P3HT/C60-CB Composites

CB powder was characterized by SEM (LEO 1530 VP), FTIR spectroscopy and Raman. FTIR measurements were carried out in purified KBr pellets using a Perkin-Elmer (Spectrum One) instrument, and Raman spectroscopy was measured by using a DXR Raman microscope (Thermo Fisher Scientific Inc.).

Morphology of the active layer was measured with SEM, tapping-mode AFM (Digital Instrument, Nanoscope II). UV-visible absorption spectroscopy of the active layer was measured by an HP 845 UV-visible absorption spectrophotometer.

A Keithley 2400 source-measuring unit was used to measure current-voltage characteristics in the dark and under irradiation. Simulated solar irradiation at 95 Mw cm^{-2} was used for light source using a Newport 150W solar simulator with an AM 1.5G filter. A calibrated thermopile detector (Thorlabs Model S210A) was used to check the irradiation intensity before every measurement.

5.3 Results and Discussion

5.3.1 Characterization of CB and P3HT/C60-CB Composites

The solutions of C60-CB and CB in ODCB are shown in Figure 5.1 a. The SEM images of the CB and C60-CB are shown in Figures 5.1 b and 5.1 c. Figure 5.1 b shows the nanostructure of CB. The FTIR spectrum of CB powder showed an O-H stretching vibration at 3332 cm^{-1} (Figure 5.1 d). Raman spectrum of CB powder showed the characteristic bands at 1580 cm^{-1} and 1340 cm^{-1}, which are presented in Fig 5.1 e.

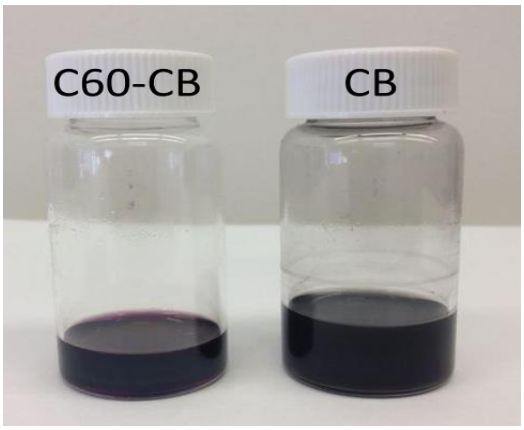

(a)

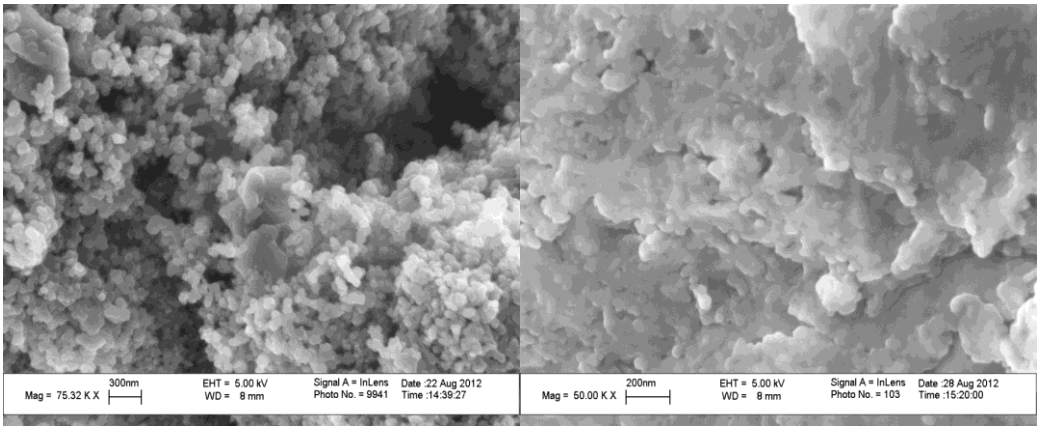

(b) (c)

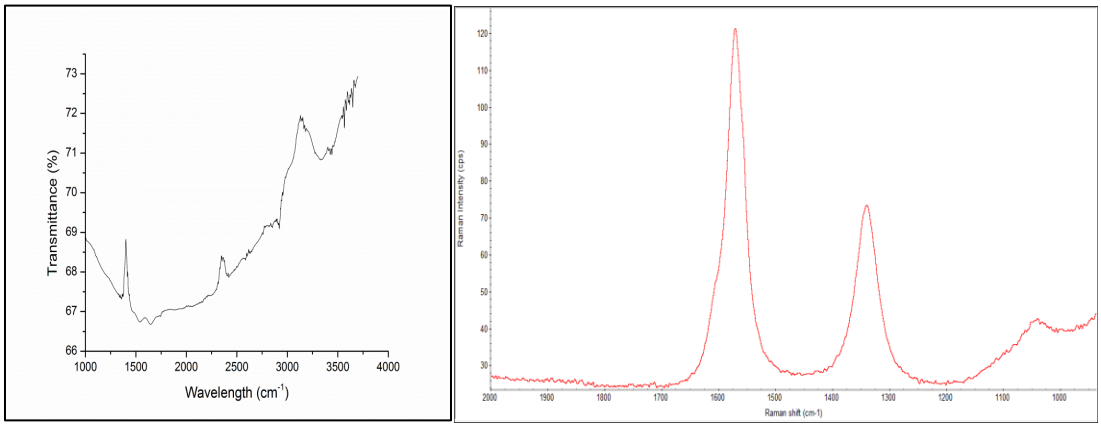

(d) (e)

Figure 5.1 (a) Photograph of C60-CB and CB solutions dissolved in ODCB. (b) SEM image of CB solution and (c) SEM image of C60-CB solution. (d) FTIR spectrum of CB powder, and (e) Raman spectrum of CB powder.

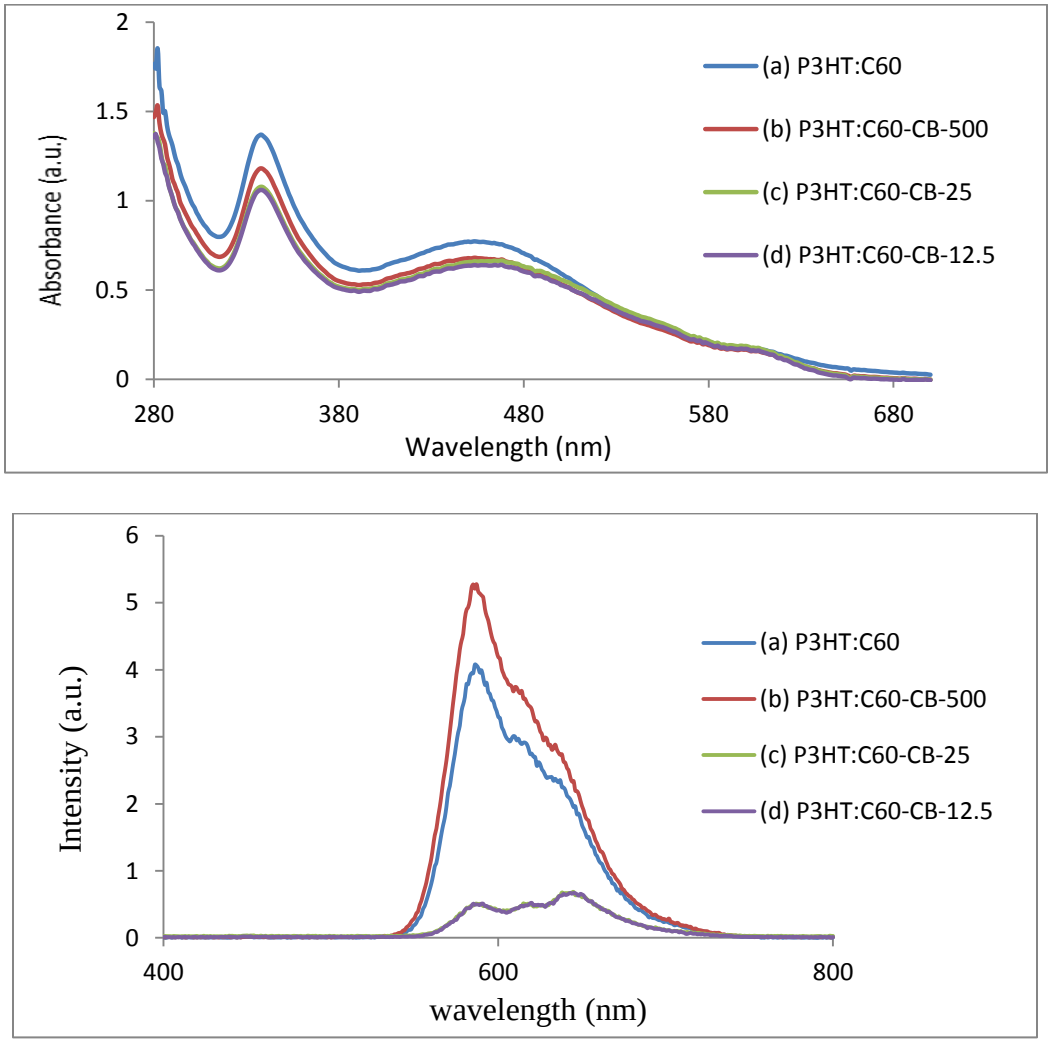

Figure 5.2 UV-visible absorption spectra and Fluorescence spectra of (a) P3HT:C60 (b) P3HT:C60-CB-500 (c) P3HT:C60-CB-25 (d) P3HT:C60-CB-12.5.

UV-Vis spectroscopy was used to characterize the effect of CB on absorption of sunlight in the P3HT:C60 film. Figure 5.2 shows the UV-Vis spectra of control cell (P3HT:C60) which had bands around 340 and 454 nm that were assigned to active layer of P3HT:C60. When CB was added to C60 and formed into active layer, the characteristic peaks of active layer showed minor shift to lower wavelengths and there was as much as

18% decrease in absorbance as CB concentration decreased to 12.5 ppm, suggesting strong interaction between the C60 and CB. Similar trend has also been reported before [65].

The fluorescence spectra of P3HT, P3HT:CB and P3HT:C60-CB composites are presented in Figure 5.2. P3HT had a strong PL in the visible region, which peaked at 587 nm. When CB was directly added to P3HT, the fluorescence intensity remained unchanged. The PL quenching by C60 provided direct evidence of the possibility of exciton dissociation and in this case was unaffected by the presence of CB. This implied that the latter did not participate in exciton dissociation [7]. The PL spectra of CB at low concentrations (12.5 ppm) showed further quenching which implied that low concentration complex may enhance exciton dissociation.

5.3.2 Morphology of Active Layers

The different photoactive films are listed in Table 5.1. SEM images in Figure 5.1 (b) and (c) showed that incorporating CB into C60 formed a homogeneous phase. Figures 5.3 (a), (b), (c) (d) at 2 μm scale showed the SEM images of the surface of active layers with four different CB concentrations (0, 12.5, 25, and 500 ppm). P3HT showed a flat surface morphology, which is a common feature of this type of polymer. With the decreasing concentration of CB, the domain size of C60-CB clusters appeared to increase, which could provide improved pathways for the percolations for the electrons and holes [87]. This indicated that CB helped in binding C60 and P3HT tightly, which led to the formation of close interface between the acceptor and the donor in order to facilitate more efficient charge transfer between the two phases [91].

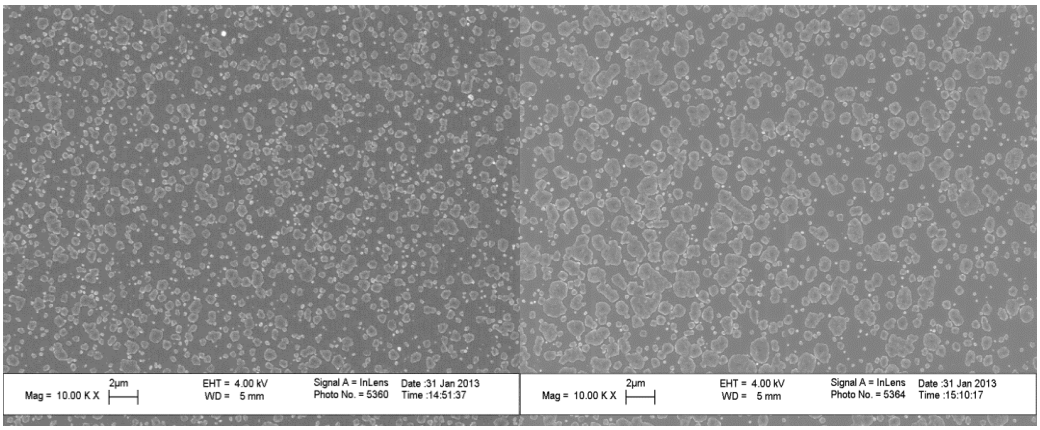

(a) (b)

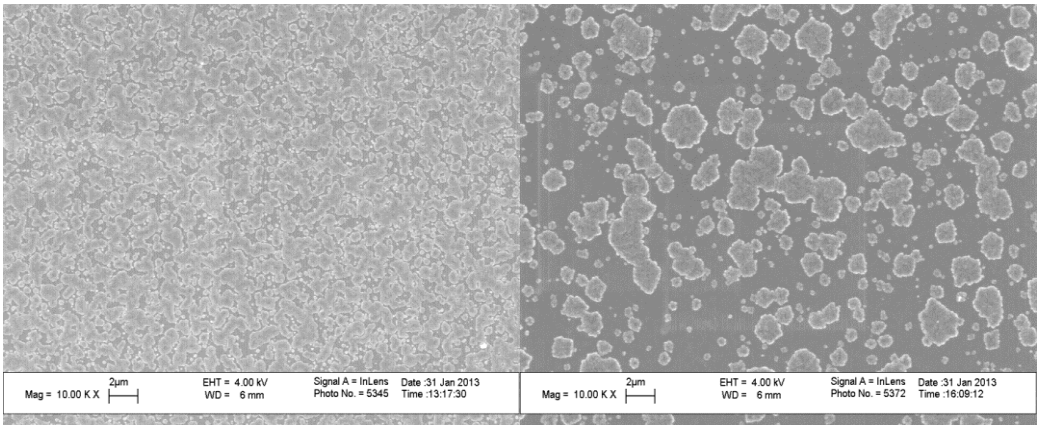

(c) (d)

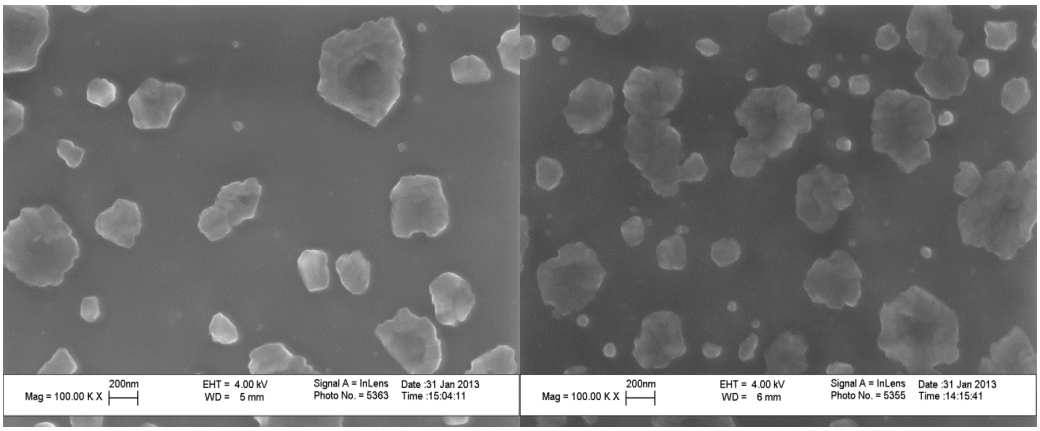

(e) (f)

Figure 5.3 SEM images of (a) P3HT:C60 at 2 µm (b) P3HT:C60-CB-500 at 2 µm (c) P3HT:C60-CB-25 at 2 µm (d) P3HT:C60-CB-12.5 at 2 µm (e) P3HT:C60 at 200 nm (f) P3HT:C60-CB-500 at 200 nm (g) P3HT:C60-CB-25 at 200 nm (h) P3HT:C60-CB-12.5 at 200 nm.

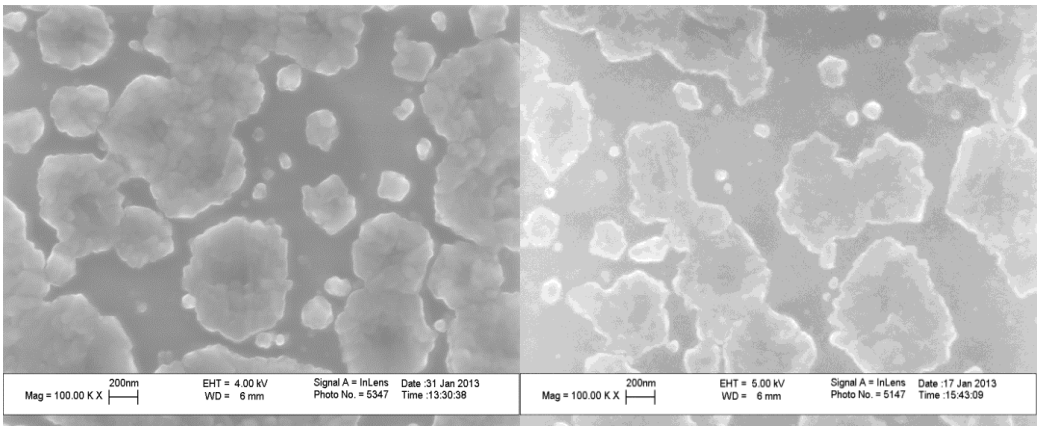

(g) (h)

Figure 5.3 SEM images of (a) P3HT:C60 at 2 µm (b) P3HT:C60-CB-500 at 2 µm (c) P3HT:C60-CB-25 at 2 µm (d) P3HT:C60-CB-12.5 at 2 µm (e) P3HT:C60 at 200 nm (f) P3HT:C60-CB-500 at 200 nm (g) P3HT:C60-CB-25 at 200 nm (h) P3HT:C60-CB-12.5 at 200 nm.

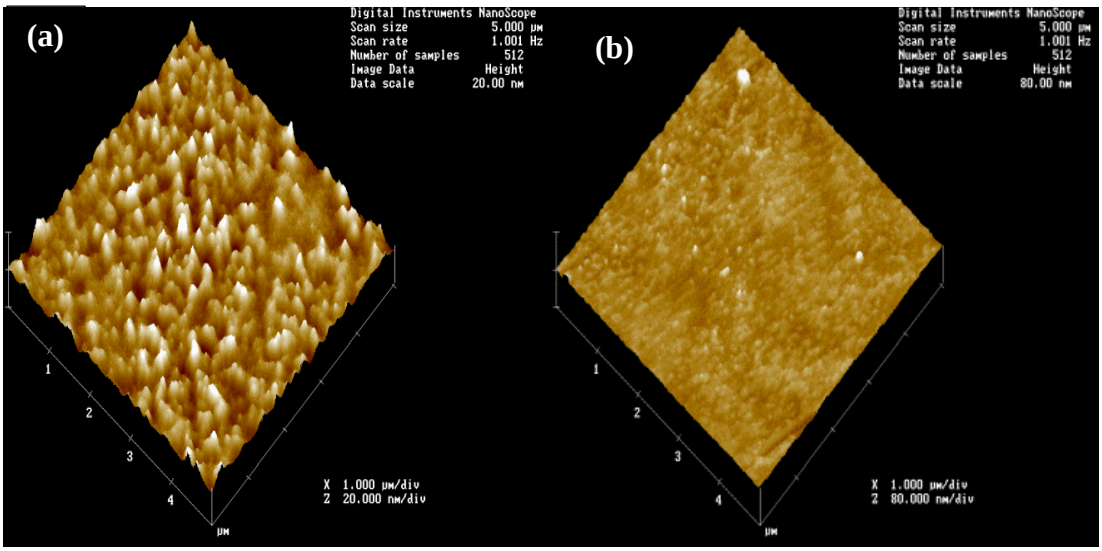

Figure 5.4 Tapping mode AFM of samples after annealing at 120°C for 10 min: (a) P3HT: C60 (b) P3HT:C60-CB-500 (c) P3HT:C60-CB-25 (d) P3HT:C60-CB-12.5.

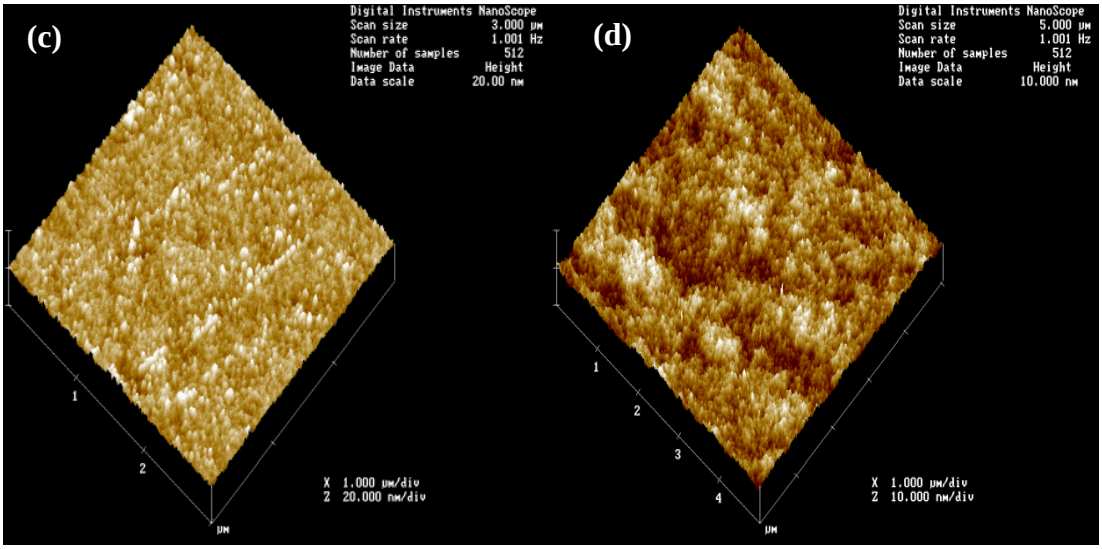

Figure 5.4 Tapping mode AFM of samples after annealing at 120°C for 10 min: (a) P3HT: C60 (b) P3HT:C60-CB-500 (c) P3HT:C60-CB-25 (d) P3HT:C60-CB-12.5.

AFM measurements of the photoactive composites showed that the presence of CB altered the film morphology, where the surface roughness was significantly different. Figure 5.4 shows that the RMS height of the P3HT:C60 film was 4.6 nm, P3HT:C60-CB-500 was 2.1 nm, while that P3HT:C60-CB-25 was 9.0 nm and P3HT:C60-CB-12.5 was 9.2 nm, where the surface roughness increased at low concentration of CB and decreased with high concentration of CB. This agrees with SEM images shown in Figure 5.3, where larger domain size of C60 was seen at low concentration of CB. The higher surface roughness may provide many advantages such as larger donor or acceptor domains, larger donor-acceptor interfaces and an increase in contact area which may affect the efficiency of charge collection at the electrode-polymer interface. It is also known to enhance internal reflection and light collection [11].

5.3.3 Photovoltaic Performance

The J-V curves for the different OPVs are presented in Figure 5.5 a and b, and their performance (mean and standard deviation) is presented in Table 5.1. From Table 5.1 and Figure 5.6, it is seen that all four solar cell performance parameters (Jsc, Voc, FF and PCE) showed similar trend. They decreased with increasing concentration of CB. At a concentration of 12.5 ppm, Jsc increased by 35%, while PCE increased by 79%. At high concentrations, the Jsc, PCE, V_{OC} as well as FF were below that of plain P3HT:C60 solar cell.

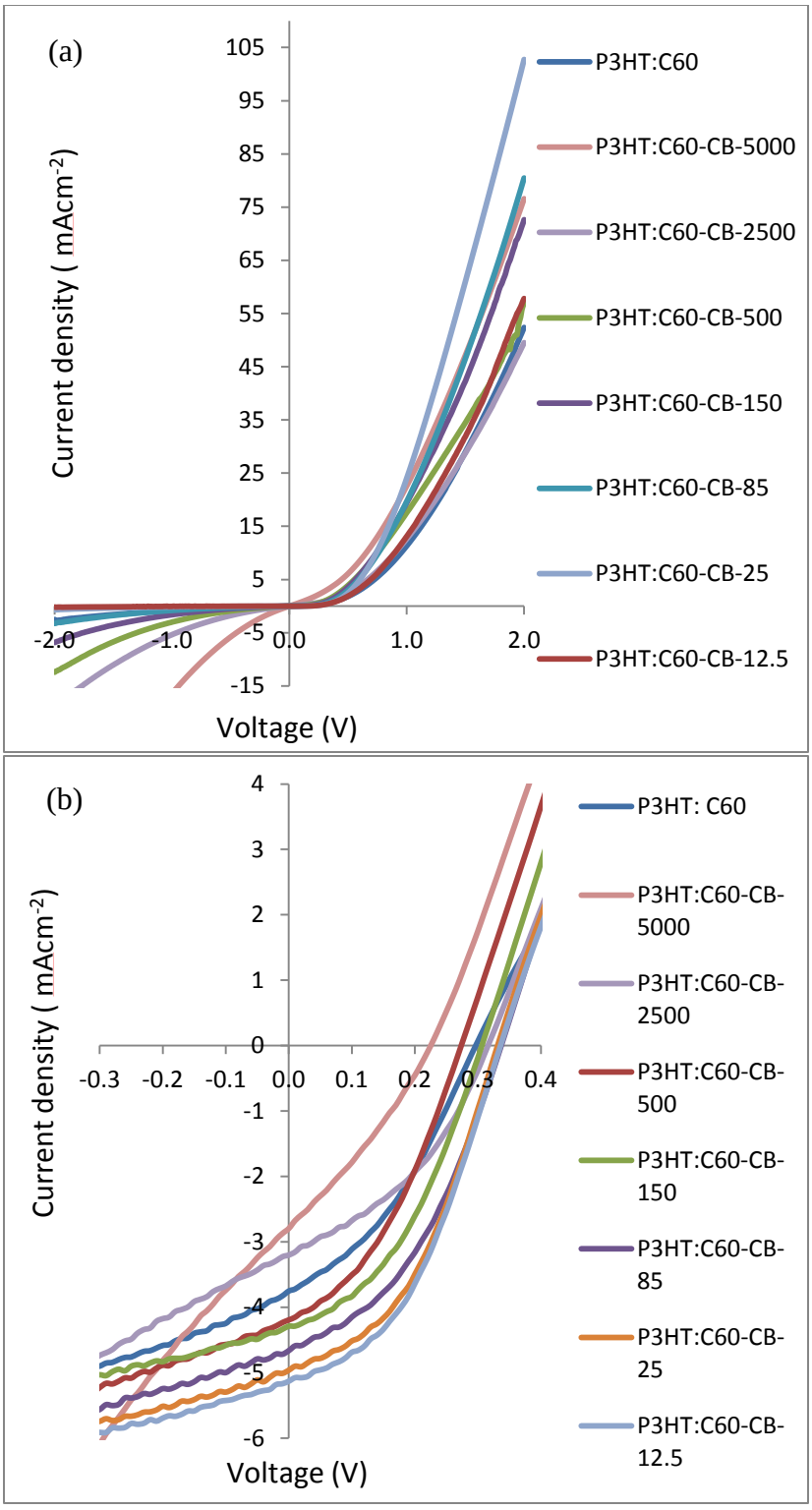

Figure 5.5 J-V characteristics in the dark (a) and under simulated solar irradiation at 95 mW cm^{-2} (b) of OPVs with P3HT:C60, P3HT:C60-CB-5000, P3HT-C60-CB-2500, P3HT:C60-CB-500, P3HT:C60-CB-150, P3HT:C60-CB-85, P3HT:C60-CB-25, P3HT:C60-CB-12.5, all of the cells were annealed at 120°C for 10 min.

Table 5.1 Photovoltaic Parameters under 95 mW/cm^2 Simulated Solar Irradiation were Measured after Thermal Annealing at 120^{o}C

Photovoltaic layer	**Concentration of Carbon Black (ppm)**	**Voc (V)**	**Jsc (mAcm^{-2})**	**FF (%)**	**PCE (%)**
P3HT: C60	0	0.31±0.02	3.74±0.42	0.35±0.02	0.43±0.04
P3HT: C60-CB-5000	5000	0.23±0.03	2.79±0.08	0.29±0.02	0.20±0.04
P3HT: C60-CB-2500	2500	0.31±0.01	2.97±0.33	0.38±0.01	0.37±0.06
P3HT: C60-CB-500	500	0.28±0.01	4.18±0.13	0.36±0.02	0.45±0.05
P3HT: C60-CB-150	150	0.30±0.01	4.35±0.14	0.41±0.01	0.57±0.03
P3HT: C60-CB-85	85	0.34±0.01	4.51±0.16	0.41±0.04	0.67±0.08
P3HT: C60-CB-25	25	0.35±0.02	4.77±0.29	0.44±0.02	0.76±0.09
P3HT: C60-CB-12.5	12.5	0.34±0.01	5.03±0.31	0.42±0.01	0.77±0.04

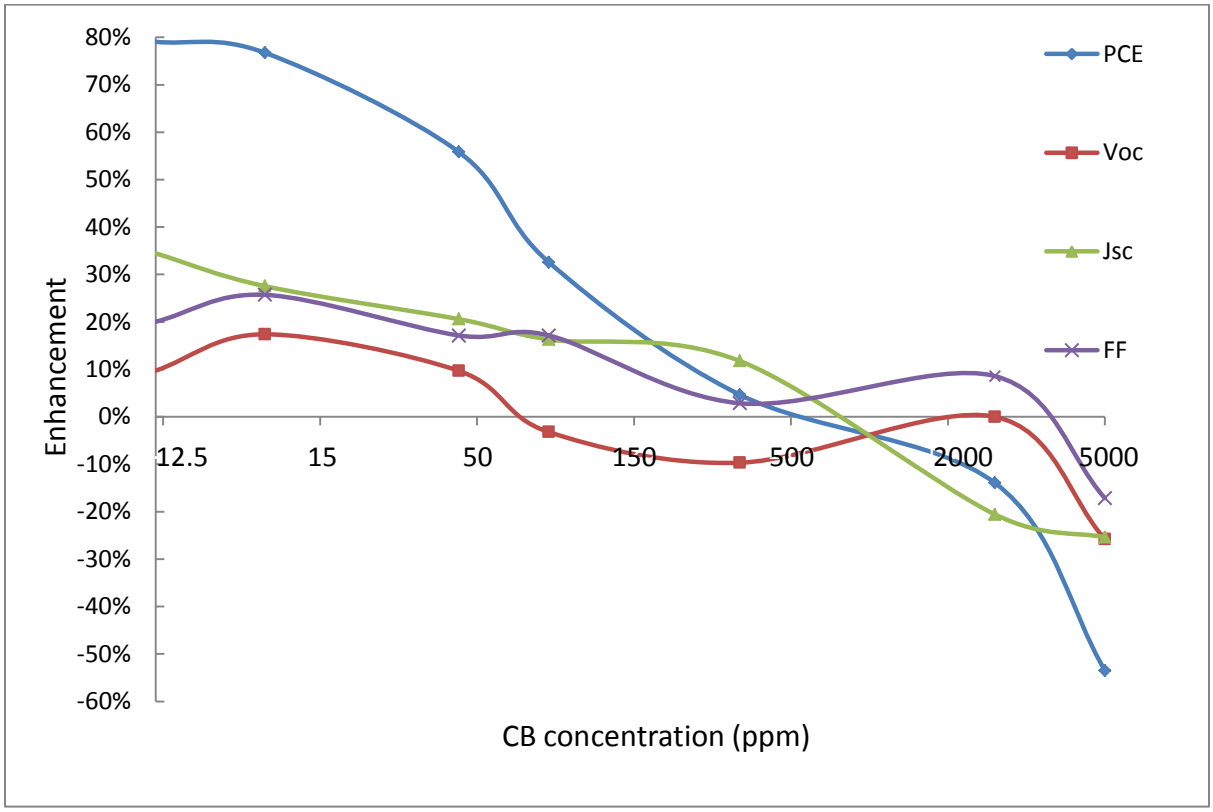

Figure 5.6 Concentration vs. PCE, Voc, FF, and Jsc.

An energy level diagram of P3HT with C60 is shown in Figure 5.7 [91]. V_{OC} depends upon the energy difference in the HOMO level of donor and LUMO level of the acceptor, and it was seen that the Voc of the P3HT:C60 and P3HT:C60-CB at low concentrations (150 to 12.5) was almost the same. Therefore, it is assumed that at low concentrations of CB, the HUMO-LUMO levels of the complex were the same as that of the C60 [92]. This implied that since the CB was encapsulated by C60, it did not participate in exciton dissociation but served to enhance charge transport. This was evidenced by the significant increase in Jsc while Voc remained the same. At high concentrations other factors came into play and Voc was no longer the same.

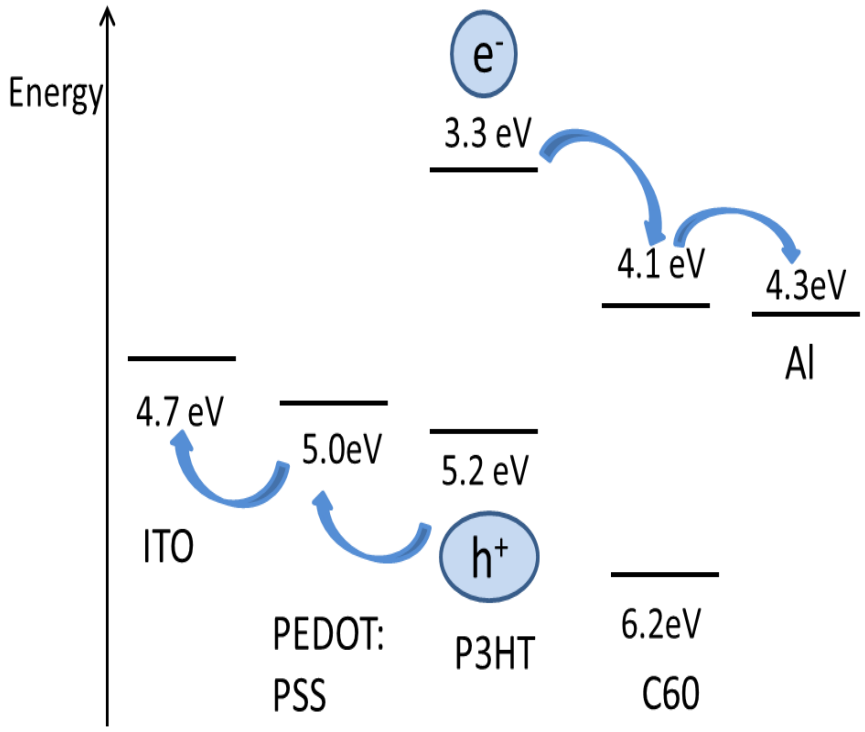

Figure 5.7 An energy level diagram of P3HT with C60 at low CB concentration.

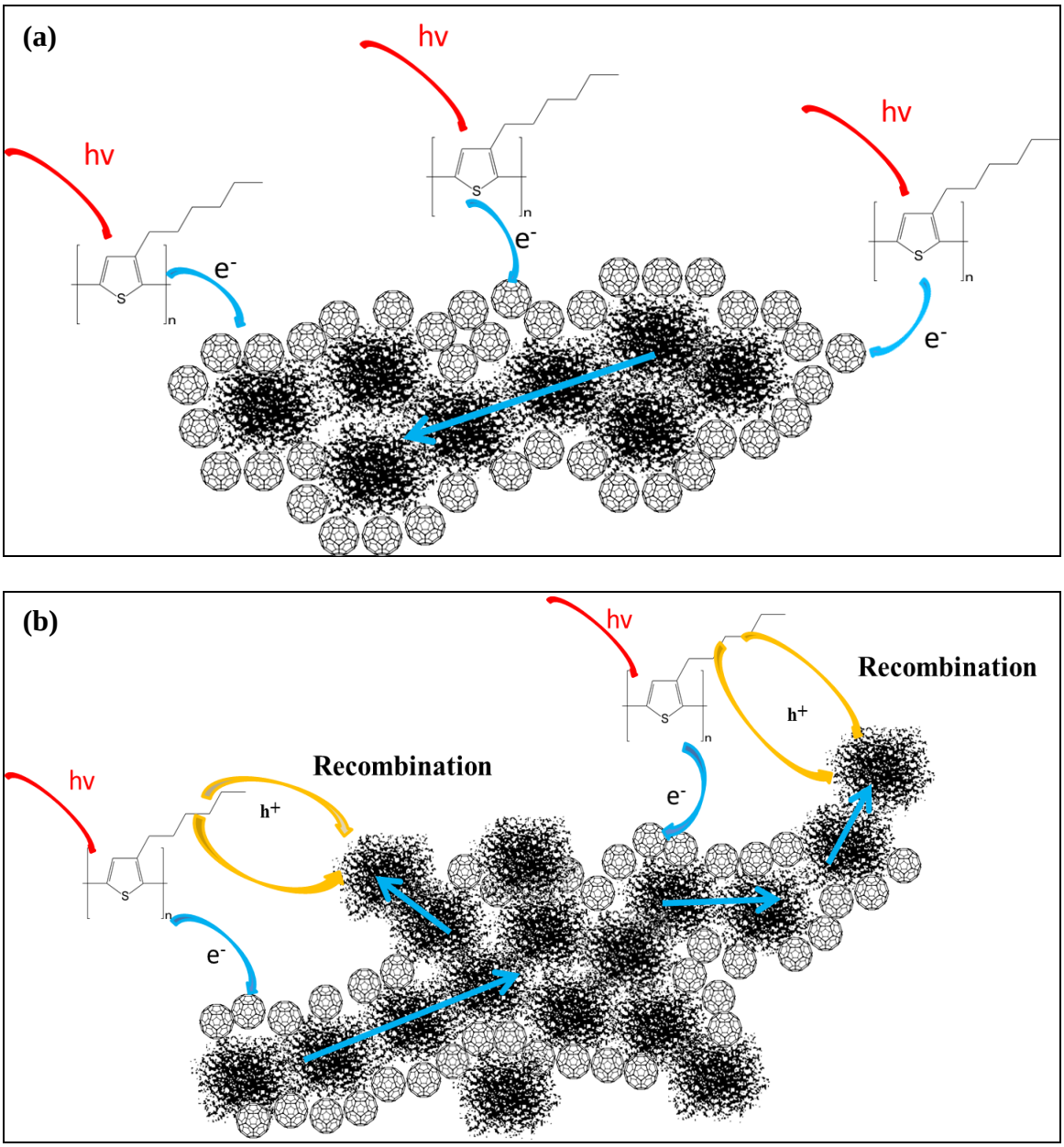

Figure 5.8 Mechanism of charge transport: (a) at low CB concentration, and (b) at high CB concentration.

The mechanism of charge transport at high and low concentration of CB is shown in Figure 5.8. In the desirable scenario, electrons are photogenerated in P3HT and transferred to C60, and then instead of hopping among the C60 molecules, they find a more efficient pathway through the C60-CB complex (Figure 5.8 a). The C60 molecules tend to

aggregate and encapsulate the CB as they polymerize under microwave irradiation [37, 47]. At high concentrations, some CB may not be covered with C60 molecules, and consequently the probability of short circuit as well as electron hole recombination increased (Figure 5.8 b). This explains why performance was so poor at 5000 and 2500 ppm. In short, it is postulated that the introduction of small concentration of CB into the P3HT-C60 system allowed better film formation and phase separation, which contributed to the enhancement of FF.

5.4 Summary

In conclusion, low concentration of CB serves as an effective additive to improve charge transport in OPVs. Low concentrations at parts per million were found to form optimum composites that showed higher short circuit current as well as PCE. The results here were obtained using P3HT:C60 system, but it is anticipated that this approach will be valid for other donor acceptor system as well.

REFERENCES

[1] Ohkita H, Cook S, Astuti Y, Duffy W, Tierney S, Zhang W, et al. Charge Carrier Formation in Polythiophene/Fullerene Blend Films Studied by Transient Absorption Spectroscopy. Journal of the American Chemical Society. 2008;130(10):3030-42.

[2] Huang DM, Moule AJ, Faller R. Characterization of Polymer–Fullerene Mixtures for Organic Photovoltaics by Systematically Coarse-Grained Molecular Simulations. Fluid Phase Equilibria. 2011;302(1–2):21-5.

[3] Thompson BC, Fréchet JMJ. Polymer–Fullerene Composite Solar Cells. Angewandte Chemie International Edition. 2008;47(1):58-77.

[4] Kippelen B, Bredas J-L. Organic Photovoltaics. Energy & Environmental Science. 2009;2(3):251-61.

[5] Huang LCL, Chang H-C. Adsorption and Immobilization of Cytochrome c on Nanodiamonds. Langmuir. 2004;20(14):5879-84.

[6] Deibel C, Dyakonov V. Polymer–Fullerene Bulk Heterojunction Solar Cells. Reports on Progress in Physics. 2010;73(9):096401-39.

[7] Cai W, Gong X, Cao Y. Polymer Solar Cells: Recent Development and Possible Routes for Improvement in the Performance. Solar Energy Materials and Solar Cells. 2010;94(2):114-27.

[8] Gunes S, Neugebauer H, Sariciftci NS. Conjugated Polymer-Based Organic Solar Cells. Chem Rev. 2007;107(4):1324-38.

[9] Nardes AM, Kemerink M, de Kok MM, Vinken E, Maturova K, Janssen RAJ. Conductivity, Work function, and Environmental Stability of PEDOT:PSS Thin Films Treated with Sorbitol. Organic Electronics. 2008;9(5):727-34.

[10] Bundgaard E, Krebs FC. Low Band Gap Polymers for Organic Photovoltaics. Solar Energy Materials and Solar Cells. 2007;91(11):954-85.

[11] Li G, Shrotriya V, Yao Y, Yang Y. Investigation of Annealing Effects and Film Thickness Dependence of Polymer Solar Cells Based on Poly(3-hexylthiophene). Journal of Applied Physics. 2005;98(4):043704-5.

[12] Nishikitani Y, Uchida S, Kubo T. Chapter 11 - Nanostructured Organic Bulk Heterojunction Solar Cells. In: Soga T, ed. Nanostructured Materials for Solar Energy Conversion. Amsterdam: Elsevier 2006, 319-33.

[13] Heeger AJ. Semiconducting Polymers: the Third Generation. Chemical Society Reviews. 2010;39(7):2354-71.

[14] Dolmatov VY. Detonation-Synthesis Nanodiamonds: Synthesis, Structure, Properties and Applications. Russian Chemical Reviews. 2007;76(4):339-23.

[15] Liu J, Tanaka T, Sivula K, Alivisatos AP, Fréchet JMJ. Employing End-Functional Polythiophene To Control the Morphology of Nanocrystal−Polymer Composites in Hybrid Solar Cells. Journal of the American Chemical Society. 2004;126(21):6550-1.

[16] Blom P, Mihailetchi, V., Koster, L. and Markov, D. Device Physics of Polymer:Fullerene Bulk Heterojunction Solar Cells. Advanced Materials. 2007;19(12):1551-66.

[17] Garcia-Belmonte G, Munar A, Barea EM, Bisquert J, Ugarte I, Pacios R. Charge Carrier Mobility and Lifetime of Organic Bulk Heterojunctions Analyzed by Impedance Spectroscopy. Organic Electronics. 2008;9(5):847-51.

[18] Li G, Shrotriya V, Huang J, Yao Y, Moriarty T, Emery K, et al. High-Efficiency Solution Processable Polymer Photovoltaic Cells by Self-Organization of Polymer Blends. Nat Mater. 2005;4(11):864-8.

[19] Illescas BM, Martín N. [60]Fullerene-Based Electron Acceptors. Comptes Rendus Chimie. 2006;9(7–8):1038-50.

[20] Ferguson AJ, Blackburn JL, Kopidakis N. Fullerenes and Carbon Nanotubes as Acceptor Materials in Organic Photovoltaics. Materials Letters. 2013;90(0):115-25.

[21] Guldi DM, Prato M. Excited-state Properties of C(60) Fullerene Derivatives. Accounts of chemical research. 2000;33(10):695-703.

[22] Liu T, Troisi A. What Makes Fullerene Acceptors Special as Electron Acceptors in Organic Solar Cells and How to Replace Them. Advanced Materials. 2013;25(7):1038-41.

[23] Hu Z, Zhang J, Xiong S, Zhao Y. Performance of Polymer Solar Cells Fabricated by Dip Coating Process. Solar Energy Materials and Solar Cells. 2012;99(0):221-5.

[24] Mastria R, Rizzo A, Nobile C, Kumar S, Maruccio G, Gigli G. Improved Photovoltaic Performances by Post-Deposition Acidic Treatments on Tetrapod Shaped Colloidal Nanocrystal Solids. Nanotechnology. 2012;23(30):305403-9.

[25] Denning MS, Watts ID, Moussa SM, Durand P, Rosseinsky MJ, Tanigaki K. Close-Packed C703- Phases − Synthesis, Structure, and Electronic Properties. Journal of the American Chemical Society. 2002;124(19):5570-80.

[26] Hummelen JC, Knight BW, LePeq F, Wudl F, Yao J, Wilkins CL. Preparation and Characterization of Fulleroid and Methanofullerene Derivatives. The Journal of Organic Chemistry. 1995;60(3):532-8.

[27] Koster LJA, Mihailetchi VD, Blom PWM. Ultimate Efficiency of Polymer/Fullerene Bulk Heterojunction Solar Cells. Applied Physics Letters. 2006;88(9):093511-3.

[28] Mihailetchi VD, van Duren JKJ, Blom PWM, Hummelen JC, Janssen RAJ, Kroon JM, et al. Electron Transport in a Methanofullerene. Advanced Functional Materials. 2003;13(1):43-6.

[29] Mikroyannidis JA, Kabanakis AN, Sharma SS, Sharma GD. A Simple and Effective Modification of PCBM for Use as an Electron Acceptor in Efficient Bulk Heterojunction Solar Cells. Advanced Functional Materials. 2011;21(4):746-55.

[30] Khatri I, Soga T. Carbon Nanotubes Towards Polymer Solar Cell. Carbon and Oxide Nanostructures: Springer Berlin Heidelberg 2011, 101-23.

[31] Tanaka H, Takeuchi K. Diameter Determination of C60 and C70 Monomers in the Gas Phase Using a Differential Mobility Analyzer. Appl Phys A. 2005;80(4):759-61.

[32] Shenderova O, Zhirnov V, Brenner D. Carbon Nanostructures. Critical Reviews in Solid State and Material Sciences. 2002;27(3-4):227-356.

[33] Zhu H, Wei J, Wang K, Wu D. Applications of Carbon Materials in Photovoltaic Solar Cells. Solar Energy Materials and Solar Cells. 2009;93(9):1461-70.

[34] Wu Z, Chen Z, Du X, Logan JM, Sippel J, Nikolou M, et al. Transparent, Conductive Carbon Nanotube Films. Science. 2004;305(5688):1273-6.

[35] Kymakis E, Amaratunga GAJ. Single-wall Carbon Nanotube/Conjugated Polymer Photovoltaic Devices. Applied Physics Letters. 2002;80(1):112-4.

[36] Li C, Chen Y, Wang Y, Iqbal Z, Chhowalla M, Mitra S. A Fullerene-Single Wall Carbon Nanotube Complex for Polymer Bulk Heterojunction Photovoltaic Cells. Journal of Materials Chemistry. 2007;17(23):2406-11.

[37] Li C, Chen Y, Ntim SA, Mitra S. Fullerene-Multiwalled Carbon Nanotube Complexes for Bulk Heterojunction Photovoltaic Cells. Applied Physics Letters. 2010;96(14):143303-3.

[38] Li C, Mitra S. Processing of Fullerene-Single Wall Carbon Nanotube Complex for Bulk Heterojunction Photovoltaic Cells: AIP; 2007;91(25):253112-3.

[39] Arranz-Andrés J, Blau WJ. Enhanced Device Performance Using Different Carbon Nanotube Types in Polymer Photovoltaic Devices. Carbon. 2008;46(15):2067-75.

[40] Lee WH, Chuang SY, Chen HL, Su WF, Lin CH. Exploiting Optical Properties of P3HT:PCBM Films for Organic Solar Cells with Semitransparent Anode. Thin Solid Films. 2010;518(24):7450-4.

[41] Chuang S-Y, Chen H-L, Lee W-H, Huang Y-C, Su W-F, Jen W-M, et al. Regioregularity Effects in the Chain Orientation and Optical Anisotropy of Composite Polymer/Fullerene Films for High-Efficiency, Large-Area Organic Solar Cells. Journal of Materials Chemistry. 2009;19(31):5554-60.

[42] Kovalenko I, Bucknall DG, Yushin G. Detonation Nanodiamond and Onion-Like-Carbon-Embedded Polyaniline for Supercapacitors. Advanced Functional Materials. 2010;20(22):3979-86.

[43] Basiuk EV, Basiuk VA, Meza-Laguna V, Contreras-Torres FF, Martínez M, Rojas-Aguilar A, et al. Solvent-free Covalent Functionalization of Multi-Walled Carbon Nanotubes and Nanodiamond with Diamines: Looking for Cross-Llinking Effects. Applied Surface Science. 2012;259(0):465-76.

[44] Pantea D, Darmstadt H, Kaliaguine S, Sümmchen L, Roy C. Electrical Conductivity of Thermal Carbon Blacks: Influence of Surface Chemistry. Carbon. 2001;39(8):1147-58.

[45] Han D, Meng Z, Wu D, Zhang C, Zhu H. Thermal Properties of Carbon Black Aqueous Nanofluids for Solar Absorption. Nanoscale Res Lett. 2011;6(1):1-7.

[46] Li G, Zhu R, Yang Y. Polymer Solar Cells. Nat Photon. 2012;6(3):153-61.

[47] Wang C, Guo Z-X, Fu S, Wu W, Zhu D. Polymers Containing Fullerene or Carbon Nanotube Structures. Progress in Polymer Science. 2004;29(11):1079-141.

[48] Dang MT, Wantz G, Bejbouji H, Urien M, Dautel OJ, Vignau L, et al. Polymeric Solar Cells Based on P3HT:PCBM: Role of the Casting Solvent. Solar Energy Materials and Solar Cells. 2011;95(12):3408-18.

[49] Probst N, Grivei E. Structure and Electrical Properties of Carbon Black. Carbon. 2002;40(2):201-5.

[50] Nagata A. Fabrication, Nanostructures and Electronic Properties of Nanodiamond-Based Solar Cells. Progress in Natural Science: Materials International. 2010; 20(0):38-42.

[51] Alvarez-Zauco E, Sobral H, Basiuk EV, Saniger-Blesa JM, Villagrán-Muniz M. Polymerization of C60 Fullerene Thin Films by UV Pulsed Llaser Irradiation. Applied Surface Science. 2005;248(1–4):243-7.

[52] P.G. Karagiannidis, D. Georgiou, C. Pitsalidis, A. Laskarakis, S. Logothetidis. Evolution of Vertical Phase Separation in P3HT:PCBM Thin Films Induced by Thermal Annealing. Materials Chemistry and Physics. 2011;129(0):1207-13.

[53] Dennler G, Scharber MC, Brabec CJ. Polymer-Fullerene Bulk-Heterojunction Solar Cells. Advanced Materials. 2009;21(13):1323-38.

[54] Hoppe H, Sariciftci NS. Morphology of Polymer/Fullerene Bulk Heterojunction Solar Cells. Journal of Materials Chemistry. 2006;16(1):45-61.

[55] Matthias A. Ruderer and Peter M€uller-Buschbaum. Morphology of Polymer-Based Bulk Heterojunction Films for Organic Photovoltaics. Soft Matter. 2011;7(12):5482-93.

[56] Yamanari T, Taima T, Sakai J, Saito K. Origin of the Open-Circuit Voltage of Organic Tthin-Film Solar Cells Based on Conjugated Polymers. Solar Energy Materials and Solar Cells. 2009;93(6-7):759-61.

[57] Wang Y, Wei W, Liu X, Gu Y. Research Progress on Polymer Heterojunction Solar Cells. Solar Energy Materials and Solar Cells. 2012;98(0):129-145.

[58] Li X, Liu L, Qin Y, Wu W, Guo Z-X, Dai L, et al. C60 Modified Single-Walled Carbon Nanotubes. Chemical Physics Letters. 2003;377(1–2):32-6.

[59] Shen Y-M, Chen C-S, Yang P-C, Ma S-Y, Lin C-F. Improvement of Surface Morphology of Thin Films and Performance by Applying Electric Field on P3HT:PCBM Based Solar Cells. Solar Energy Materials and Solar Cells. 2012;99(0):263-7.

[60] Raty J-Y, Galli G. First Principle Study of Nanodiamond Optical and Electronic Properties. Computer Physics Communications. 2005;169(1-3):14-9.

[61] Dupont SR, Oliver M, Krebs FC, Dauskardt RH. Interlayer Adhesion in Roll-to-Roll Processed Flexible Inverted Polymer Solar Cells. Solar Energy Materials and Solar Cells. 2012;97(0):171-5.

[62] Stoneham M. Electrons in Carbon Country. Nat Mater. 2004;3(1):3-5.

[63] Service RF. Outlook Brightens for Plastic Solar Cells. Science. 2011;332(6027):293-1.

[64] Segura JL, Martin N, Guldi DM. Materials for Organic Solar Cells: the C60/Pi-Conjugated Oligomer Approach. Chem Soc Rev. 2005;34(1):31-47.

[65] Radbeh R, Parbaile E, Chakaroun M, Ratier B, Aldissi M, Moliton A. Enhanced Efficiency of Polymeric Solar Cells via Alignment of Carbon Nanotubes. Polymer International. 2010;59(11):1514-9.

[66] Ratier B, Nunzi J-M, Aldissi M, Kraft TM, Buncel E. Organic Solar Cell Materials and Active Layer Designs—Improvements with Carbon Nanotubes: a Review. Polymer International. 2012;61(3):342-54.

[67] Arbogast JW, Foote CS. Photophysical Properties of C70. Journal of the American Chemical Society. 1991;113(23):8886-9.

[68] Pfuetzner S, Meiss J, Petrich A, Riede M, Leo K. Improved Bulk Heterojunction Organic Solar Cells Employing C70 Fullerenes. Applied Physics Letters. 2009;94(22):223307-3.

[69] Lau XC, Desai C, Mitra S. Functionalized Nanodiamond as a Charge Transporter in Organic Solar Cells. Solar Energy. 2013;91(0):204-11.

[70] Chen Y, Mitra S. Fast Microwave-Assisted Purification, Functionalization and Dispersion of Multi-Walled Carbon Nanotubes. Journal of Nanoscience and Nanotechnology. 2008;8(11):5770-5.

[71] Powell C, Bender T, Lawryshyn Y. A Model to Determine Financial Indicators for Organic Solar Cells. Solar Energy. 2009;83(11):1977-84.

[72] Kalowekamo J, Baker E. Estimating the Manufacturing Cost of Purely Organic Solar Cells. Solar Energy. 2009;83(8):1224-31.

[73] Yap CC, Yahaya M, Salleh MM. Effect of Organic Salt Doping on the Performance of Single Layer Bulk Heterojunction Organic Solar Cell. Solar Energy. 2011;85(1):95-9.

[74] Pivrikas A, Neugebauer H, Sariciftci NS. Influence of Processing Additives to Nano-Morphology and Efficiency of Bulk-Heterojunction Solar Cells: A Comparative Review. Solar Energy. 2011;85(6):1226-37.

[75] Kalita G, Masahiro M, Koichi W, Umeno M. Nanostructured Morphology of P3HT:PCBM Bulk Heterojunction Solar Cells. Solid-State Electronics. 2010;54(4):447-51.

[76] Derbal-Habak H, Bergeret C, Cousseau J, Nunzi JM. Improving the Current Density Jsc of Organic Solar Cells P3HT:PCBM by Structuring the Photoactive Layer with Functionalized SWCNTs. Solar Energy Materials and Solar Cells. 2011;95, Supplement 1(0):53-6.

[77] Guangyong L, Liming L. Carbon Nanotubes for Organic Solar Cells. Nanotechnology Magazine, IEEE. 2011;5(3):18-24.

[78] Ren S, Bernardi M, Lunt RR, Bulovic V, Grossman JC, Gradečak S. Toward Efficient Carbon Nanotube/P3HT Solar Cells: Active Layer Morphology, Electrical, and Optical Properties. Nano Letters. 2011;11(12):5316-21.

[79] Pradhan B, Batabyal SK, Pal AJ. Functionalized Carbon Nanotubes in Donor/Acceptor-type Photovoltaic Devices. Applied Physics Letters. 2006;88(9):093106-3.

[80] Liu L, Stanchina WE, Li G. Effects of Semiconducting and Metallic Single-Walled Carbon Nanotubes on Performance of Bulk Heterojunction Organic Solar Cells. Applied Physics Letters. 2009;94(23):233309-3.

[81] Cataldo S, Salice P, Menna E, Pignataro B. Carbon Nanotubes and Organic Solar Cells. Energy & Environmental Science. 2012;5(3):5919-40.

[82] Kalita G, Adhikari S, Aryal HR, Umeno M, Afre R, Soga T, et al. Cutting Carbon Nanotubes for Solar Cell Application. Applied Physics Letters. 2008;92(12):123508-3.

[83] Tezuka N, Umeyama T, Seki S, Matano Y, Nishi M, Hirao K, et al. Comparison of Cluster Formation, Film Structure, Microwave Conductivity, and Photoelectrochemical Properties of Composites Consisting of Single-Walled Carbon Nanotubes with C60, C70, and C84. The Journal of Physical Chemistry C. 2010;114(7):3235-47.

[84] Nismy NA, Jayawardena KDGI, Adikaari AADT, Silva SRP. Photoluminescence Quenching in Carbon Nanotube-Polymer/Fullerene Films: Carbon Nanotubes as Exciton Dissociation Centres in Organic Photovoltaics. Advanced Materials. 2011;23(33):3796-800.

[85] Dabera GDMR, Jayawardena KDGI, Prabhath MRR, Yahya I, Tan YY, Nismy NA, et al. Hybrid Carbon Nanotube Networks as Efficient Hole Extraction Layers for Organic Photovoltaics. ACS Nano. 2012;7(1):556-65.

[86] Wang XX, Wang JN, Su LF. Preparation and Electrochemical Performance of Ultra-Short Carbon Nanotubes. Journal of Power Sources. 2009;186(1):194-200.

[87] Deng X, Xiong D, Wang H, Chen D, Jiao Z, Zhang H, et al. Bulk Enrichment and Separation of Multi-Walled Carbon Nanotubes by Density Gradient Centrifugation. Carbon. 2009;47(6):1608-10.

[88] Cheng X, Zhong J, Meng J, et al.,Characterization of Multiwalled Carbon Nanotubes Dispersing in Water and Association with Biological Effects. Journal of Nanomaterials. 2011;2011(0):938491-11.

[89] Karagiannidis PG, Georgiou D, Pitsalidis C, Laskarakis A, Logothetidis S. Evolution of Vertical Phase Separation in P3HT:PCBM Thin Films Induced by Thermal Annealing. Materials Chemistry and Physics. 2011;129(3):1207-13.

[90] Yu G, Gao J, Hummelen JC, Wudl F, Heeger AJ. Polymer Photovoltaic Cells: Enhanced Efficiencies via a Network of Internal Donor-Acceptor Heterojunctions. Science. 1995;270(5243):1789-91.

[91] Zhou Y, Shim JW, Fuentes-Hernandez C, Sharma A, Knauer KA, Giordano AJ, et al. Direct Correlation Between Work Function of Indium-Tin-Oxide Electrodes and Solar Cell Performance Influenced by Ultraviolet Irradiation and Air Exposure. Physical Chemistry Chemical Physics. 2012;14(34):12014-21.

[92] Chen G, Yokoyama D, Sasabe H, Hong Z, Yang Y, Kido J. Optical and Electrical Properties of a Squaraine Dye in Photovoltaic Cells. Applied Physics Letters. 2012;101(8):083904-11.